Selective Area Growth of cubic Gallium Nitride by Molecular Beam Epitaxy

Dissertation

submitted to the Departement of Physics in fullfilment of the requirements for the degree of 'Doctor rerum naturalium' at Paderborn University by

M. Sc. Falco Meier

First reviewer: Prof. Dr. Donat J. As
Second reviewer: Prof. Dr. Jörg K. N. Lindner

January 23, 2023

Abstract

In this thesis, Selective Area Growth (SAG) of cubic Gallium Nitride (c-GaN) on 3C-SiC/Si (001) pseudo substrates is demonstrated. Silicon Dioxide was employed as a growth mask, preventing nucleation of c-GaN on covered surfaces. Plasma deposited and thermal silicon oxides were employed and patterned by means of Nanosphere Lithography (NSL), Block-Copolymer Lithography (BCP) and Electron Beam Lithography (EBL). NSL and BCP were utilized to achieve hole arrays with 130 nm and 17 nm in diameter. EBL was employed for patterning of U- and V-shaped grooves. Patterns were transferred into SiO_2 by Reactive Ion Etching. 3C-SiC and SiO_2 were etched by SF_6 and CHF_3/Ar plasmas, respectively. It was possible to demonstrate phase pure and selective nucleation down to nano scales of 17 nm and 100 nm on <001> and <111> facets of 3C-SiC, correspondingly. Hexagonal fraction of GaN was confirmed by means of Transmission Electron Microscopy (TEM) and High Resolution X-Ray Diffraction (HRXRD). On checker board patterns with openings of 3 mm, hexagonal phase contents below 1 % were achieved. On V-shaped grooves, approximately exposing <111> facets along [110] in 3C-SiC, a hexagonal phase content of 17.6 % was estimated. For all structures, phase pure nucleation was shown by TEM imaging. Furthermore, coalescence was shown to be possible after nano SAG of c-GaN with dominant cubic phase. On BCP patterned holes the lowest hexagonal fraction observed was 29% after coalescence of GaN.

Key words: Gallium Nitride, Silicon Carbide, Plasma Assisted Molecular Beam Epitaxy, Selective Area Growth, Lithography

Declaration

I hereby declare that this thesis is my own work and effort and that it has not been submitted anywhere for any award. Where other sources of information have been used, they have been acknowledged. Results already published elsewhere will be marked respectively.

23.01.2023 Falco Meier

Contents

CHAPTER 1

Introduction

Wide bandgap group III Nitrides could be utilized to replace common semiconductors. Due to their favorable mechanical [Hau18], thermal [Amb96; Hau18] and electrooptical [Hau18; Str92] properties, nitrides stay interesting for a lot of applications. Nowadays, one of the most prominent application is the blue LED invented by Nakamura. [Heb14] Besides blue LED's, Nitrides can also be used in Telecommunication as the Band gap of cubic Indium Nitride is about 0.6 eV. By mixing Indium, Gallium and Aluminum with Nitrogen a range from 0.6 eV to 4.4 eV can be covered within the cubic Nitride material system, granting usability for a lot of applications like LED's, LD's and more. Nitrides are also suitable for high frequency applications [For05]. In industry, hexagonal nitrides are commonly utilized, e.g. for LED's, as they are easy to grow with high quality on sapphire and other commercially available substrates.

Efficiency of such devices is strongly limited by internal polarization fields caused by hexagonal crystal symmetry. These polarization fields result in the so called Quantum Confined Stark Effect (QSCE), which limits the overlap of wave functions in active low dimensional structures, e.g. Quantum Wells. Therefore, the effect reduces the internal quantum efficiency of devices based on hexagonal Nitrides. These inefficiencies could be treated by employing the cubic phase of Gallium Nitride [Tsa22]. Figure 1.1 depicts the Internal Quantum Efficiency (IQE) versus current density. As can be seen, polar nitrides suffer 51% efficiency droop compared to their cubic counterparts at high current densities. Furthermore Tsai et al. revealed, that c-GaN based devices are more immune to Auger electron-hole interactions and other efficiency degrading effects.

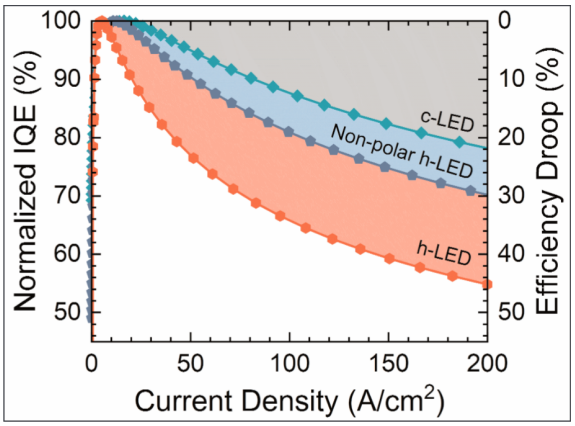

Figure 1.1: Normalized IQE (left y-axis) and efficiency droop (right y-axis) as a function of current density are plotted. Red hexagons and green rhombuses refer to the h- and c-LEDs, whereas blue pentagons refer to the nonpolar h-LED grown on m-plane GaN substrates. Taken from [Tsa22].

Despite its symmetric advantages, the cubic phase is metastable and therefore very hard to grow with high crystal quality. Additionally, no lattice matched substrates exist. This strongly limits structural and morphological quality of GaN epilayers, and therefore devices based on cubic Nitrides, dramatically. Successful SAG of c-GaN could overcome previous limits and therefore promote c-GaN to commercial qualities.

The presented work engages the challenging task of growing cubic Gallium Nitride (c-GaN) selectively. Selective Area Growth (SAG) is a commonly used technique to overcome mismatch induced crystal defects like Stacking Faults (SF). SAG is used in many material systems to grow materials with lattice mismatch on different substrates as HSU et al. successfully demonstrated for Gallium Arsenide on patterned Silicon (Si) substrates [Hsu12]. In this way it is possible to switch to cheaper substrates like Si. In the case of cubic Nitrides it could allow to achieve new grades of crystal quality as no lattice matched substrates exist. The closest substrate utilized is 3C Silicon Carbide (3C-SiC) with a mismatch of 3.2 %. State of the Art thin films with thicknesses of around 600 nm exhibit Full width at half maximum (FWHM) of Rocking curves of about 30 arcmin with hexagonal contents well below 1%. Surface roughness Root Mean Square (RMS) of such films is in the order of 4 nm on 10x10 μm^2. While this is a good start, such structural quality is not good enough to compete with hexagonal counterparts. In cubic Gallium Nitride 54.7° stacking faults are the dominating defects reducing crystal quality. Therefore it is crucial to find techniques to reduce SF density. On successful implementation comparable works show reduction of FWHM of a factor of 2 at least [She02]. For hexagonal Nitrides multiple techniques were already demonstrated useful[Fan08; Kap97; Sch11; Tan00]. Furthermore, proper SAG parameters could allow additional techniques like Pendeoepitaxy, Nano Hetero Epitaxy, Aspect Ratio Trapping and many more to become viable [Che08; Ju04; Lin99; Liu16; Man20].
Successfully implementing SAG is strongly dependent on different factors like the lattice mismatch, the sticking coefficient of ad atoms, III/V flux ratios, substrate temperature and more. The fact that GaN is metastable in its cubic phase adds more difficulty on top. When adapting growth parameters to ensure selectivity its unclear if the cubic phase can be kept dominant. Therefore this work is not only about achieving selective but also cubic growth within SAG conditions. Besides the work of Shen et al. [She02], up to now only Ricada Kemper attempted Nanoheteroepitaxie (NHE) to increase c-GaN quality by reducing the growth area [Kem14]. While being somewhat successful, the growth was not selective and therefore not usable in combination with masks. If growth is not selective there is little to no chance to achieve coalescent cubic films with higher quality compared to films grown with regular heteroepitaxy on unpatterned 3C-SiC substrates. A byproduct of Kempers work were V-shaped grooves approximately dissecting <111> facets of 3C-SiC. TEM measurements revealed that c-GaN and c-AlN deposited in such grooves were defect free. It is impossible to cover all conceivable techniques within one thesis to a satisfying extend. The main goal of this thesis is to find a mentioned set of SAG conditions while preserving the cubic phase and try to achieve coalescence. Selective nucleation will be tested down to nanoscopic scales. Additionally, SAG conditions for cubic nucleation in V-Grooves, with an angle of 54.7° exposing (111) facets, etched into 3C-SiC along [110] and [1-10] shall be found. In the work of R. Kemper such

V-shaped grooves were artifacts of the patterning. In this work such growth shall be reproduced selectively and without Aluminum Nitride interlayers.

CHAPTER 2

Theory

In the following chapter theoretical basics are presented. This includes the properties of cubic Nitrides and correlated Crystals like the substrate made of 3C-SiC (001). For growth Plasma Assisted Molecular Beam Epitaxy (PAMBE) is used. Usually c-GaN is grown with carefully optimized substrate temperature to ensure that a monolayer (ML) of Ga is present during growth the whole time. The description and theory of this method does not hold for selective growth as the substrate temperature has to be increased by over 100°C to achieve selectivity between 3C-SiC and SiO_2. Therefore, a brief explanation is given based on experimental findings. There is no citable explanation of the process of growing cubic Nitrides with PAMBE without a metal monolayer. This process is still subject of current research. Nevertheless, growth at elevated temperatures was already suspected to happen in a so called evaporation-condensation equilibrium [Sch02]. First results in such a growth regime are presented in section 4.2.
Additionally, characterization methods of Nitrides are explained. In situ monitoring is done via Reflective High Energy Electron Deflection (RHEED). Characterization methods involve High Resolution X-Ray Diffraction (HRXRD), Atomic Force Microscopy (AFM), Scanning Electron Microscopy (SEM), Transmission Electron Microscopy (TEM) and Photoluminescence measurements (PL).
Patterning of Masks was done with the help of optical and electron beam Lithography as well as self organization methods like Nanosphere Lithography (NSL) and Block-Copolymer Lithography (BCP). All lithographic techniques will be covered briefly.
The Chapter is concluded with theoretical background about Reactive Ion Etching (RIE) processes necessary to pattern SiO_2 and 3C-SiC.

2.1 Group III-V Nitrides and related Crystals

The following chapter describes the fundamental properties of the employed Crystals. Namely this will cover Nitrides, especially Gallium Nitride as well as substrate materials. To begin with, table 2.1 lists all physical parameters.
From the table 2.1 we can see that only 2 substrates offer a comparably small lattice mismatch of below 4%. On one hand we have 3C-SiC (001) with a mismatch of -3.9% and c-AlN (001) with a mismatch of -3.4%. Despite the smaller lattice mismatch of c-AlN in most cases 3C-SiC is utilized as this substrate is commercially available.
In this work heteroepitaxial growth is mainly conducted on 3C-SiC. Besides that homoepitaxial SAG of c-GaN on c-GaN is tested. Homoepitaxial SAG is concerned to increase selectivity.

crystal	Lattice constant[Å]		Bandgap[eV]	lattice mismatch to c-GaN[%]
	a	c		
c-GaN	4.53[Pow93]	-	3.21[Pow93]	
h-GaN	3.289[Pas04]	5.186[Pas04]	3.44[Gol01]	
c-InN	4.97[Tab99]	-	0.61[Sch06]	9.7
h-InN	3.5365[Dav]	5.7039[Dav]	0.9[Dav]	
c-AlN	4.38[She91]	-	4.5[Ber06]	-2.8
h-AlN	3.112[Pas04]	4.981[Pas04]	5.9[Oku98]	
Si	5.419[Str52]	-	1.179[Blu74]	16.4
3C-SiC	4.359[She91]	-	2.3[Har95]	-3.2
YSZ	5.125[CRY]	-	5.8[Nic92]	11.6

Table 2.1: Overview of physical parameters for employed Crystals in this work, including lattice constant and bandgap for Nitrides, their respective substrates as well as lattice mismatches to c-GaN (001).

2.1.1 Properties of Nitrides

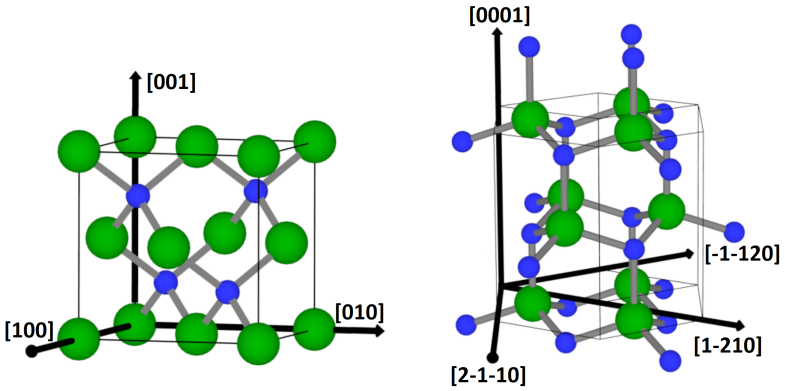

Figure 2.1: Ball and Stick scheme depicting the cubic zinc blende Gallium Nitride phase (left) and the wurtzite hexagonal Gallium Nitride phase (right). Green represents Gallium and blue Nitrogen.

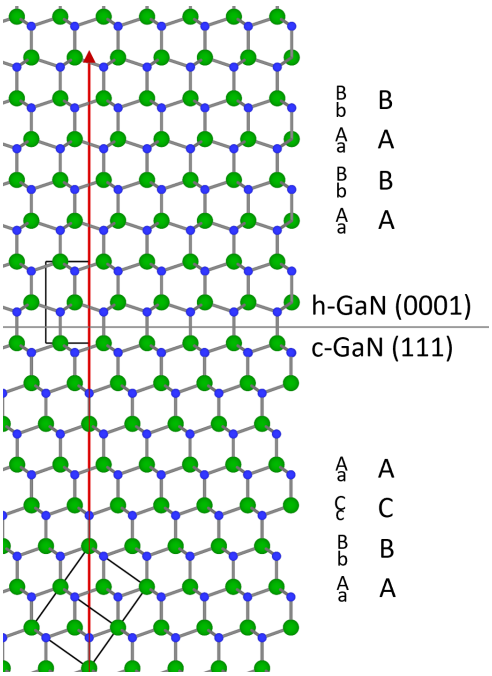

Figure 2.2: Schematic of zinc blende (111) to wurtzite (0001) transition in GaN projected towards [1-10]. Black boxes depict the unit cell with respect to the projection. Red Vector gives (111)/(0001) direction.

Group III-V Nitrides like Indium Nitride (InN), Gallium Nitride (GaN) and Aluminum Nitride (AlN) occur in two phases. Nitrides tend to nucleate and grow in the stable hexagonal wurtzite (WZ) phase. By employing epitaxy, Nitrides can also be grown in the metastable cubic zinc blende (ZB) phase. Fig. 2.1 depicts both phases with the help of a ball and stick theme. Green balls are representative for Gallium and blue balls for Nitrogen. For the ZB phase 1 unit cell is plotted. Hexagonal WZ is plotted with 3 unit cells to emphasize hexagonal symmetry, which is more intuitive compared to a single unit cell. Both phases are made of tetrahedra with Gallium in the center surrounded by 4 Nitrogen atoms. The stacking sequence is different for both phases (see Fig 2.2). Along (111) ZB is stacked ABCABC while WZ is stacked ABABAB along (0001). In the Nitride system both crystallographic directions are very similar and have a very small lattice mismatch of 0.4% for the c-GaN/h-GaN <111/0001> interfaces. The critical thickness of c-GaN on 3C-SiC is in the range of a

few monolayers. Therefore, Misfit Dislocations (MD), causing Stacking Faults (SF) and hexagonal inclusions on <111> facets of the ZB phase are the most prominent defects, limiting the crystal quality. Forming such SF and hexagonal inclusions is the main mechanism of strain relaxation. By choosing proper cubic substrates, like 3C-SiC, and careful stoichiometric control of the III/V ratio, cubic phase can be epitaxially maintained.
The Nitride material system already offers some advantages in the hexagonal phase, e.g. thermal[Amb96; Hau18] and mechanical[Hau18] stability as well as electrooptical[Hau18; Str92] properties. Besides that there is the theoretical possibility of mixing ternary and quarternary compounds made of AlN, GaN and InN. Their bandgap energies E_g cover a wide range from 0.61 eV (infrared) to 5.9 eV (ultraviolet). Thus, Nitrides could be useful for a wide range of applications.
The wurtzite phase exhibits polarization fields along its c axis. Polarization is subjected to cause the so called Quantum Confined Stark Effect (QSCE). QSCE is a delicate derogation of efficiency in wurtzite GaN devices. While blue LED's made of h-GaN are efficient enough to be competitive, QSCE is rendering green h-GaN LED's bootless. This effect is also called "Green Gap". By employing zinc blende structure those fields can be avoided. Due to the discussed properties of cubic Nitrides, crystal quality is insufficient to compete with hexagonal nitrides up to now [Nip16; Tsa22].

2.1.2 Properties of Substrates

In this work Silicon (Si) , Silicon Dioxide (SiO_2) and 3C Silicon Carbide (3C-SiC) are employed as substrates and masks. Si exhibits a diamond structure, which is very similar to the zinc blende structure. The main difference is the atomic base. Where zinc blende is made up of different atoms, e.g. Ga and N, diamond structure is only made up of one atom like Si (see Fig. 2.1). Si is very cheap, commercially available and among the purest crystalline materials one can get hands on. This makes it perfect for testing purposes, where the crystal phase is not that important, e.g. for selectivity testing.
The mainly used substrate for this thesis is 3C-SiC (001). SiC is a semiconducting ceramic compound made of Silicon and Carbon. In industry SiC is utilized because of its chemical and mechanical robustness making it useful for e.g. car brakes, bullet proof vests and many more. Since the 1970's it is also used in electronics for manufacturing of LED's and Detectors. SiC is especially suited for devices operated in extreme environments, operated with high power and high frequencies. Over 200 different polytypes have been identified for SiC. The most prominent phases are 3C-SiC, 4H-SiC and 6H-SiC. The latter ones are made of wurtzite with different stacking sequences or unit cell length (2H,4H, 6H), while 3C-SiC exhibits the zinc blende structure. The wurtzite polytypes stack like ABAB (2H), ABCB (4H), ABCACB (6H) respectively.

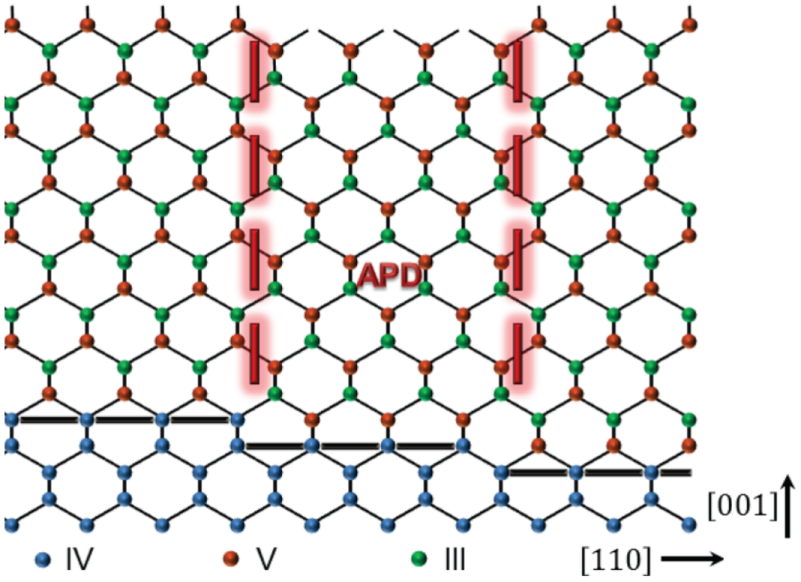

Figure 2.3: Schematic of the Silicon/3C-Silicon Carbide Interface with monoatomic steps. These steps on the substrates surface lead to Anti Phase Domains (APD) in the epilayer. Taken and adopted from [Fau16].

Commercially available 3C-SiC (001) substrates are usually not free standing but thin films deposited on Si (001). This is done by a complicated Metall Organic Chemical Vapor Deposition (MOCVD) process in industry. After deposition of 20 μm the film is grounded to about 10 μm to achieve a surface roughness of below 1 nm.
Since the lattice mismatch between Si (001) and 3C-SiC (001) is close to 20%, this process comes along with a lot of SF in 3C-SiC grown on Si. These SF are accompanied by Anti Phase Domains (APD), where the lateral atomic sequence reverses (see Fig. 2.3). APD's are introduced by atomic surface steps and can be suppressed by introducing miscut Si or 3C-SiC surfaces [Fau16; Lee19b]. However, SF can not be suppressed this way.
All of the aforementioned defects can propagate into GaN epiplayers during growth. Even if there would be no lattice mismatch between 3C-SiC and c-GaN, introducing more defects, those defects from the substrate would remain and propagate into the epilayer. Additionally, defects lines like SF have a predominant orientation depending on the respective APD [Lee19a]. This is very important for the prospect of tailoring nanoscopic structures in order to exploit SAG techniques like Aspect Ratio Trapping (ART).

2.2 Epitaxy

The term epitaxy (greek "order, alignment") is describing the adoption of crystallographic properties (orientation, lattice constant, phase, etc.) of condensing matter on a crystalline substrate. If at least one property is adopted growth is concerned to be epitaxial. If the materials grown on top of each other are identical (e.g. GaN on GaN) it is called homoepitaxy. If the materials differ (e.g. GaN on 3C-SiC) it

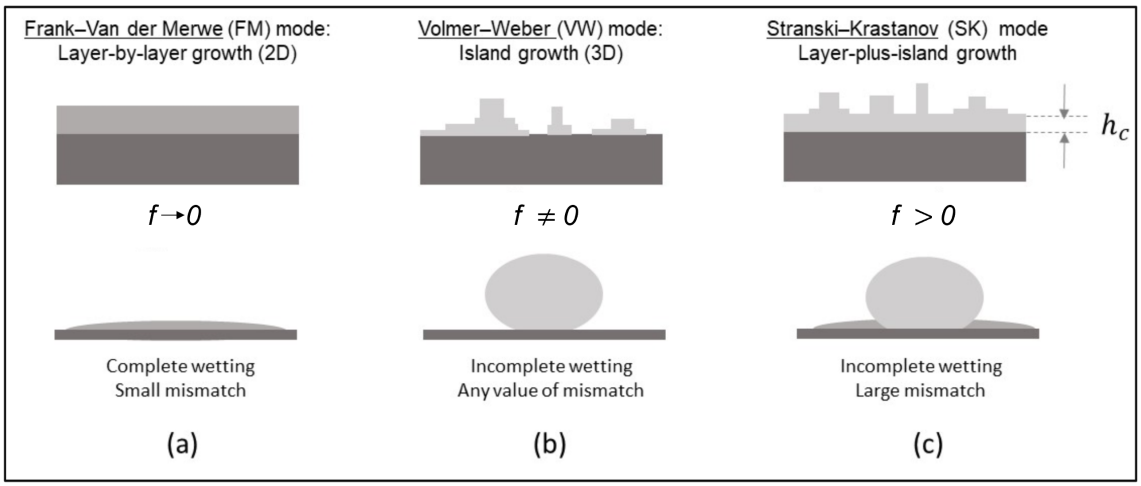

Figure 2.4: Scheme depicts growth modes with respect to the lattice missmatch f and the wetting of the substrate. a) 2D Layer-by-layer growth, b) 3D Island growth c), Layer-plus-island growth. Adopted and taken from [Tas19].

is called heteroepitaxy. One of the crucial parameters during epitaxial growth is the lattice mismatch. It is a measure for the deviation between lattice constants of epilayer and substrate and is given by the following formula:

$$f = \frac{a_l - a_s}{a_s} \tag{2.1}$$

With a_l the lattice constant of the layer and a_s the lattice constant of the substrate. When growing a mismatch layer the unit cell of the epilayer has to be distorted in order to fit onto the substrate. This is called a pseudomorphically strained layer. One also differentiates between tensile (f<0) and compressive (f>0) strain. Furthermore, the crystal can only grow pseudomorphic until the critical layer thickness h_c is reached. Above this thickness the layer will relax the accumulated deformation potential by introducing defects which can be accompanied by island formation.
Fig. 2.4 depicts the possible growth modes. If f is close to 0 the critical layer thickness is very large. Hence, pseudomorphic or even unstrained growth can be maintained for thick layers or structures. By carefully setting material fluxes, two dimensional (2D) layer-by-layer growth can be achieved. This is also called Frank-Van-der Merve

growth. 2D growth is very useful for 2D structures, as atomically sharp interfaces can be achieved. On miscut substrates growing layers can propagate as steps, leading to so called step flow growth. If the lattice mismatch is greater than 0 the epilayer is compressively strained. After growing past the critical layer thickness the layer relaxes by the formation of islands, switching to 3 dimensional (3D) growth. This, so called Stranski-Krastanov growth mode can be used to grow quantum dots. If the mismatch is large enough relaxation can happen right after nucleation, resulting in 3D growth without any strained layer below. Nucleation happens in independent islands that can coalesce to form a closed layer. This is accompanied by a lot of defects.
Epitaxial growth is conducted with different established techniques nowadays. The most prominent techniques are Liquid Phase Epitaxy (LPE), Metall Organic Chemical Vapor Deposition (MOCVD), Plasma Enhanced Chemical Vapor Deposition (PECVD) and (Plasma Assisted) Molecular Beam Epitaxy (PAMBE, MBE).
For LPE a crystal seed is placed in a carefully prepared over saturated solution. The material solved can then deposit on the seedling and grow. This technique is very good to achieve good structural qualities and stoichiometric control of the solvents. Drawbacks are its susceptibility against parameter deviations and the challenge to achieve atomically sharp interfaces.
Another important technique is MOCVD. Metall organic precursors are introduced into a chamber, where they react at the substrates surface to form the layer. This allows for sharp interfaces. With MOCVD techniques a big area can be laminated and therefore it is very commonly used in industrial applications. Nevertheless, MOCVD employs very toxic precursors and it is very hard to monitor all the reactions going on in such a chamber.
In PECVD Systems deposition occurs after reaction of precursor gases in a plasma chamber. After ignition Elements of the plasma react and nucleate to form an epilayer. One of the main advantages compared to other CVD techniques is that the energy for the reaction of precursors is introduced by a plasma and not by heat. Therefore, it is also possible to achieve useful epilayers at much lower temperatures. This opens CVD for different applications like lamination of plastics. Plasma deposition can also be used to induce chemical reactions with the substrate. This can be helpful to increase sticking of the epilayer. MBE utilizes molecular beams. The used materials are evaporated inside a ultra high vacuum chamber from Knudsen cells and are directed towards the substrate. This allows for very precise stoichiometric control. Because of the very low pressures inside the chamber very low background doping levels are incorporated into the layers. Furthermore, very sharp atomically flat interfaces can be achieved. The disadvantage of MBE is the limited substrate size and comparably small growth rates. This makes MBE an excellent choice in research but their use is limited in industry. In this work MBE will be used to grow Nitrides and PECVD to deposit oxides.

2.2.1 Epitaxy of cubic Gallium Nitride

In order to find a theoretical approach of the discovered process of growing cubic Nitrides selectively (see chapter 4), a brief explanation of Gallium's behavior as an ad atom is given. Afterwards experimental findings of previous works are discussed and put into perspective of the experimental findings of this work.
Description of Gallium's kinetic surface diffusion during MBE growth follows [BRY; Bry16; Shi89] inspired by Burton, Carbera and Frank (BCF) theory [Bur51]. Film growth is initiated with the so called nucleation phase. Ga atoms from the impinging molecular beam condensate above the substrates surface. After condensation they can either diffuse, re-evaporate or nucleate with a group V element like Nitrogen or Arsenic. In our case the impinging III/V flux ratio is always above unity. Therefore, understanding of the kinetic behavior of the group III element is crucial.
There are thermodynamic approaches for GaN growth inside MOCVD setups. In our case these descriptions don't fit very well as growth is very far from thermodynamic equilibrium and at very low pressures compared to MOCVD. For that reason growth of GaN is explained mostly by surface kinetics.

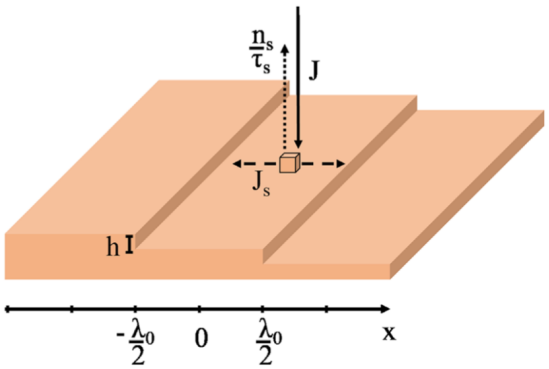

Figure 2.5: Scheme of a stepped but atomically flat surface. Depicts the possible interactions of Ga atoms impinging onto the surface. Taken from [Bry16].

The simplified situation of Gallium ad atoms on a stepped surface is depicted in Fig. 2.5. Without any nucleation occuring, the net flux adsorbed $J_v(x)$ is equal to the diffusion flux on the surface within a terrace. Steps circumfencing terraces can occur due to different effects like step flow growth from a miscut substrate, defects reaching up to the surface or grain boundaries. If steps are assumed to be sinks with an adsorption probability of 1 the system depicted in Fig. 2.5 can be described with the following continuity equation:

$$\frac{\partial J_s(x)}{\partial x} = J - \frac{n_s(x)}{\tau_s} = J_v(x) \tag{2.2}$$

With $J_v(x)$ the net absorbed flux, $J_s(x)$ the surface diffusion flux, J the ad atom flux from the vapor phase to the surface, n_s the ad atom density on the surface, τ_s the mean ad atom residence time and λ_0 the terrace width or distance between steps in the surface. In order to discuss diffusion it is also important to acknowledge Einstein's formula for the mean displacement of an ad atom [Bur51; Poh20]:

$$x_s = \sqrt{D_s \cdot \tau_s} \tag{2.3}$$

Where D_s is the diffusion coefficient. Diffusion is described as a thermodynamic process with an exponential behavior. For simple molecules and atoms the following equation can be used[Bur51]:

$$D_s = a^2 \cdot \nu' \cdot e^{\frac{-E_d}{k_b T}} \tag{2.4}$$

with a the distance between 2 neighboring lattice sites, ν' the atomic frequency (~10^{13}Hz), E_d the diffusion barrier, k_b the Boltzmann constant and T the temperature. Inserting (2.2) and (2.4) into (2.3) yields a more sophisticating expression for the mean diffusion length of a Gallium ad atom:

$$x_s = a \cdot \sqrt{\nu' \cdot e^{\frac{-E_d}{k_b T}} \cdot \frac{n_s(x)}{J - J_v(x)}} \tag{2.5}$$

From (2.5) it is possible to deduce 2 important influences for the mean free path of Ga on the surface. The mean free path is reducing with increasing temperature. This is intuitive as a hotter surface has more energy to evaporate atoms. On the other hand the mean free path can be increased by just offering more Gallium (increase adsorbed flux $J_v(x)$).
This leads to the conclusion, that the same diffusion length of Ga ad atoms can be achieved for different sets of Gallium flux and surface temperature. The ad atom density n_s not necessarily changes as a higher adsorbed flux can be compensated by shorter residence times (increase in surface temperature). Therefore, this behavior is arbitrary from the absolute amount of ad atoms on the substrate.
The previous discussion cuts short influences like the Ehrlich-Schwöbel barrier by just assuming steps to be sinks of ad atoms. Here we neglect the possible influence by assuming a very low density of steps as our substrates are without any nominal miscut in most cases. Also the total amount of Ga atoms on the surface, as well as the ratio of available and occupied surface sites for residual Ga atoms is not discussed.
As Nitrogen is introduced into the chamber nucleation starts to take place. Since the growth rate is limited by the Nitrogen flux, under the assumption of a III/V flux ratio above unity, the kinetic behavior of Nitrogen adsorbed onto the surface is

probably neglectable.
Because of the lattice mismatch growth always starts 3D. Small and very flat 3D islands form and coalesce after a certain growth time to form a 2D film. Previous works also reveal, that the growth rate is not linear. It drops to a steady state growth rate after coalescence. This is important because usually growth rate is averaged over the whole growth time. A longer nucleation time could be mistaken for a lower growth rate after reaching a steady state 2D growth. It was also shown that nuclei capture impinging atoms is the dominating process for growth. Diffusion towards nuclei was shown to be neglectable [Hea96].
By careful control of Ga flux and substrate temperature it should be possible to achieve comparable 2D growth over a large range of substrate temperatures in direct contrast to previously published works regarding growth of cubic Nitrides. Because of the meta stability of the cubic phase it was concerned to be highly challenging to keep the phase while achieving noteworthy crystal qualities. Usually a narrow substrate temperature window of around 720°C (thermocouple shows ~750°C in our case) is recommended for c-GaN on 3C-SiC and found to be working very well. Additionally, due to the lower total energy of the hexagonal phase, stabilization of the cubic phase during nucleation is sometimes achieved by comparably low temperature nucleation (600°C) and by keeping the III/V flux ratio above unity [As03; Sch02]. To keep the flux ratio above unity and prohibit Ga droplet formation, surface coverage of Ga is monitored carefully via RHEED (see section 3.7). Flux and substrate temperature are optimized in a way, that exactly a monolayer of Ga ad atoms is present. This counteracts the comparably short diffusion length at the regular growth temperatures of 720°C. While the diffusion length is short due to the noteworthy re-evaporation of Ga atoms, the Ga flux is increased to maintain the coverage and metal rich growth. This leads to the conclusion that good 2D growth in the cubic Nitride system is not necessarily depended on long diffusion length which is very counter intuitive but was also shown by Haedrick et al. and Gotschke et al. [Got11; Hea96].
Quite recently, it was experimentally found that it is also possible to keep the cubic phase while dramatically increasing the nucleation and growth temperature to over 800°C (see section 4.2) without increasing the impinging Gallium flux.
Nevertheless, previous works [Sch02] also state that elevated growth temperatures of around 800°C should increase crystalline quality because they suspected GaN begins to dissociate. That would cause irregularly nucleated atoms to be insufficiently bonded to contribute to 3 dimensional or irregular growth. Those Ga atoms are available for nucleation on energetically more favorable sites after dissociation and probably contributing to the total flux of Gallium available for growth. This approach is backed by experimental findings (see chapter 4). Noteworthy GaN dissociation occurs above 900°C as the growth rate decreases (see section 4.1.2).
Growing GaN with dominant cubic phase under metal rich conditions at elevated substrate temperatures (T_s»720°C) is still subject of current research. Growth at

such temperatures is also known to be favorable for hexagonal Nitrides and for the formation of hexagonal inclusions [Sch02]. Nitrides grown by MOCVD are usually described by process supersaturation condensing a lot of parameters into one quantity. However, this description does not hold in MBE grown as the vapor pressures are not comparable. Also selective growth in MOCVD can be described by supersaturation. In case of PAMBE, there is no sophisticated thermodynamic description of the process, yet.
An explanation concluding the counter intuitive observations could be that moving further away from the thermodynamic equilibrium could maintain the metastable cubic phase as each nucleation has to take place faster then re-evaporation. Therefore the adsorbed material has little to no time for diffusion and formation energetically favorable hexagonal nuclei or 3D irregularities.

2.2.2 Selective Area Growth

Selective Area Growth (SAG) and Selective Area Epitaxy (SAE) are established growth techniques for a wide variety of crystalline materials. The aim of these techniques is to achieve selective growth by offering different surfaces or facets of the substrate.
There is a difference between both terms because selective deposition does not necessarily includes epitaxial growth. Especially parasitic growth on unwanted surfaces tends to produce very polycristalline and unorientated material. But even if nucleation is reduced to the aimed surfaces proper parameters for epitaxial growth have to be found and maintained.
SAG and SAE are subject to a lot of research regarding Nitrides at the moment. Within MOCVD setups selectivity can be achieved by just offering different facets of the substrate, e.g. Stark et al. demonstrated that GaN doesn't nucleate on Si (001) but on the Si (111) facets [Sta13]. However, such conditions could not be found within our PAMBE setup.

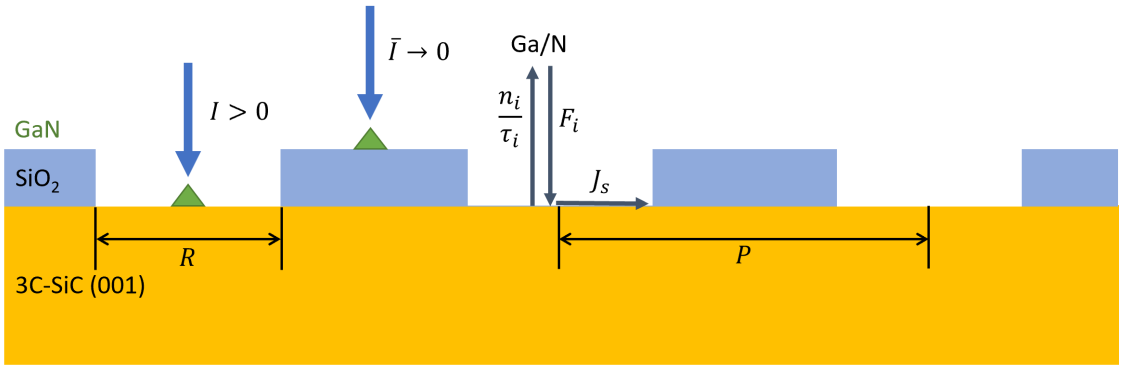

Figure 2.6: Scheme of a masked and atomically flat surface. Depicts the possible sites of GaN nucleation at the surface (blue arrows) and material adsorption and desorption (black arrows, comp. Fig. 2.5).

There are plenty of reports documenting SAG and SAE with different mask materials preventing nucleation of GaN on Si [Got11], on SiO_2 [Fan08; Kap97; Sch11; Tan00], on SiN_x [Ber10] and on Ti [Hir08]. Unfortunately, most of the mentioned works cover selective growth of hexagonal Nitrides or growth within MOCVD setups. Nevertheless, it was shown that SAG/SAE of c-GaN on 3C-SiC is possible by Suda et al. and Meier et al. [Mei21; Sud00]. The basic explanation is that the temperature dependent sticking coefficient of Ga is smaller for all of the aforementioned mask materials compared to the bare 3C-SiC or Si substrate [Mei21]. Also Dubrovskii et al. [Dub21] stated that Ga droplet formation on masks is strongly inhibited. Therefore the substrate temperature was mainly subjected to be the crucial parameter for

SAG/SAE of c-GaN. Besides that most of the publications suspect that also the III/V flux ratio is crucial, not only for keeping the cubic phase but for selectivity itself.
Gridchin et al. recently presented a theoretical model for SAG of GaN [Gri22] deduced by selective growth of h-GaN nanowires. To my current knowledge there are no other useful approaches for the theoretical description of SAG of c-GaN within MBE setups. Within MOCVD selectivity is usually described by Ga supersaturation. This reduction is already a harsh approximation as epitaxy usually is far away from thermodynamic equilibrium. Furthermore, growth inside MBE setups is conducted at much lower pressures compared to MOCVD processes, resulting in an even more kinetic process.
Gridchin et al. found a mathematical description of growth regimes with the help of nucleation rates. The idea is astonishing and simple. The result also qualitatively holds for the observations of this work. Description follows the work of Gridchin et al. [Gri22].
Figure 2.6 depicts a 3C-SiC surface with SiO_2 masked regions. Selectivity itself can be described by different nucleation rates of GaN on the substrate and the mask.

$$I > \frac{1}{\pi R^2 \tau_{Ga}} > 0 \; ; \; \bar{I} < \frac{1}{(S - \pi R)^2 \tau_{\bar{Ga}}} \to 0 \tag{2.6}$$

Nucleation rates I,$\bar{I}$ are given by eq. (2.6), with R^2 the radius of approximately circular mask openings and the respective residence times τ_{Ga},$\tau_{\bar{Ga}}$.

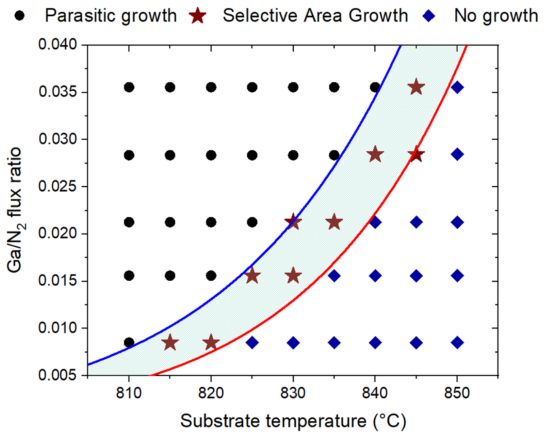

Figure 2.7: III-V flux ratio over temperature diagram showing data points experimentally generated by Gridchin et al. of SAE of h-GaN NW on Si (111). Three growth regimes, given by eq. (2.11), are plotted to show the process window of SAG.Taken from [Gri22].

SAG can be classified to occur in-between the regimes of non-growth and parasitic-growth. The first inequality describes the nucleation rate of GaN within mask opening. To have growth inside the nucleation rate I has to be greater then zero. If Ga flux is insufficient or growth temperature is to high there is no GaN nucleation on the bare 3C-SiC substrate. The second inequality demands the absence of parasitic growth on the SiO_2 mask. Therefore, nucleation rate $\bar{I}$ around the mask openings $(S - \pi R)^2$ has to be as close to zero as possible. If Gallium flux is to high or growth temperature is to low GaN can nucleate on the mask. Both are strongly dependend on the Ga residence time as activated

Nitrogen is much more volatile.
All Ga and N atoms arriving within mask openings either have the chance to nucleate or desorb. Nucleation can be described by the total amount of Ga and N presend on the surface. As Ga adatoms have a much higher mobility, GaN nucleation is strongly dependend on Ga diffusion.

$$I = D_{Ga} n_{Ga} n_N \tag{2.7}$$

Where D_{Ga} is the Gallium diffusion constant, n_{Ga} Gallium adatom density and n_N Nitrogen adatom density. The total fluxes can be described as following.

$$F_{Ga} = \frac{n_{Ga}}{\tau_{Ga}} + D_{Ga} n_{Ga} n_N \; ; F_N \approx 2 D_N n_{Ga} n_N^2 \tag{2.8}$$

Eq. (2.8) takes into account that N probably desorbs as N_2. It also neglects the possibility of Ga diffusion from or towards the mask openings which is, in first approximation, also supported by our own observations (see section 4.1). Combining eq. (2.6), (2.7) and (2.8) yields a describtion by fluxes and diffusion coefficients. At least for hexagonal GaN these are estimated in literature.

$$\frac{1}{\pi R^2 \tau_{Ga}} \frac{1 + D_{Ga}\tau_{Ga}\sqrt{\frac{F_N}{2D_N}}}{D_{Ga}\tau_{Ga}\sqrt{\frac{F_N}{2D_N}}} < F_{Ga} < \frac{1}{\pi R^2 \bar{\tau_{Ga}}} \frac{1 + \bar{D_{Ga}}\bar{\tau_{Ga}}\sqrt{\frac{F_N}{2\bar{D_N}}}}{\bar{D_{Ga}}\bar{\tau_{Ga}}\sqrt{\frac{F_N}{2\bar{D_N}}}} \tag{2.9}$$

This inequalities can be rewritten with eq. (2.4) and the general expression for residence time [Bur51] to get a general expression for the III/V flux ratio in dependence of the substrate temperature necessary to achieve SAG.

$$\tau_i = \nu_{des} e^{-\frac{E_{des}}{k_b T}} \tag{2.10}$$

SAG growth regime can be generally described by the following inequalities.

$$\frac{R_0^2}{R^2} e^{-\frac{\Delta E}{k_B T}} \left(1 + \varepsilon e^{\frac{\Delta E - E_{des}^{Ga}}{k_B T}}\right) < \frac{F_{Ga}}{F_N} < \frac{\bar{R_0}^2}{P^2 - R^2} e^{-\frac{\Delta \bar{E}}{k_B T}} \left(1 + \bar{\varepsilon} e^{\frac{\Delta \bar{E} - E_{\bar{des}}^{\bar{Ga}}}{k_B T}}\right) \tag{2.11}$$

Rewritten by employing the following definitions:

$$R_0^2 = \frac{1}{\pi a F_{N2}^{3/2}} \frac{\left(\nu_{des}^{Ga}\right)^2 \sqrt{\nu_{diff}^{N}}}{\nu_{diff}^{Ga}} \; ; \; \bar{R_0}^2 = \frac{1}{\pi a F_{N2}^{3/2}} \frac{\left(\nu_{des}^{\bar{Ga}}\right)^2 \sqrt{\nu_{diff}^{\bar{N}}}}{\nu_{diff}^{\bar{Ga}}} \tag{2.12}$$

$$\Delta E = 2E_{des}^{Ga} + \frac{E_{diff}^{N}}{2} - E_{diff}^{Ga} \; ; \; \Delta \bar{E} = 2E_{des}^{\bar{Ga}} + \frac{E_{diff}^{\bar{N}}}{2} - E_{diff}^{\bar{Ga}} \tag{2.13}$$

$$\varepsilon = \left(2\sqrt{2}\pi R_0^2 \frac{F_N}{\nu_{des}^{Ga}}\right)^{-1} \; ; \; \bar{\varepsilon} = \left(2\sqrt{2}\pi \bar{R_0}^2 \frac{F_N}{\nu_{des}^{\bar{Ga}}}\right)^{-1} \; ; \; P = \sqrt{S/\pi} \tag{2.14}$$

Taking both inequalities into account SAG growth regime is limited by two curves. One curve separates the SAG regime from the non-growth regime. It describes the limit where Ga adsorption is not sufficient for nucleation. The other curve describes adsorption limit for Ga on top of the mask. If too much Ga adsorbs on the mask parasitic nucleation occurs. Fig 2.7 depicts the solution of eq. (2.11) for the case of SAE of h-GaN nanowires (NW). For this simulation the parameters can be found in the work of Gridchin et al. [Gri22]. The blue and red curves separate process windows with parasitic/selective growth (blue) and selective/no growth. The data points correspond to measurements taken from different samples. The samples exhibit a quantitatively well known temperature gradient. Therefore, it was possible to test different substrate temperatures for a fixed flux. Fortunately, the simulated curves fit measurement data very well. While our results quantitatively differ the qualitative description holds very well for our experiments.
Besides being able to correlate III/V flux ratio and substrate temperature necessary for SAG, eq. (2.11) also describes the influence of the masks geometry by the parameter P which describes the pitch, the distance between mask openings. If the pitch is large there is a lot of masked area for nucleation. If the pitch is too large the SAG process window vanishes completely [Gri22].
In total the description yields 3 important parameters. Over a large variety of substrate temperatures matching III/V flux ratios ensuring SAG exist. Therefore, it is crucial to carefully estimate the proper III/V flux ratio for a given substrate temperature or vice versa. Besides that, the masks dimensions themself can determine if there is a SAG growth regime at all.

2.3 Characterization

2.3.1 Reflective High Energy Electron Deflection

Reflective High Energy Electron Deflection (RHEED) utilizes a fine electron beam with energys in the range of 5-50 keV. It hits the samples surface under grazing incidence interfering with topological features on atomic scales. The resulting interference pattern allows in-situ monitoring of the growing Crystal. Analyzing the RHEED pattern yields useful information, e.g. epitaxial relation between substrate and epilayer, surface domains and reconstructions, surface roughness, periodicity of the unit cell, growth rates and more [Has12; Poh20]. Due to the small incidence angle RHEED is very surface sensitive.

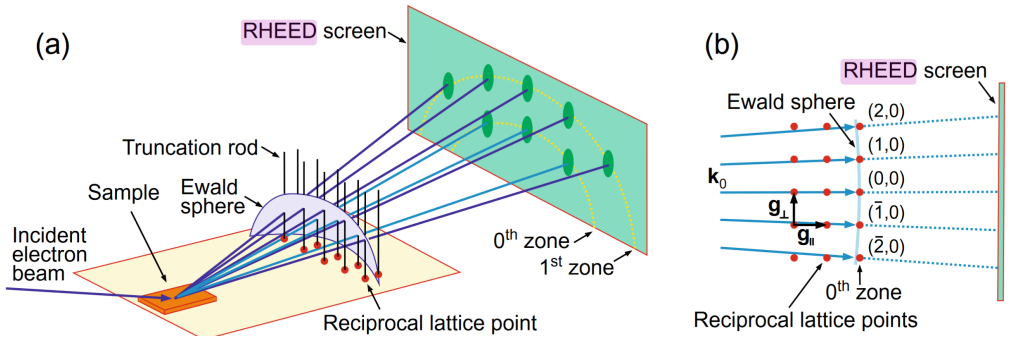

Figure 2.8: Schematic of RHEED system with diffraction spots of a cubic lattice. a) Red dots indicate the two-dimensional reciprocal lattice of the sample surface-lattice, the intersection points of the vertical black truncation rods with the Ewald sphere define the directions of diffracted beams. Yellow dotted semicircles on the screen indicate Laue circles. b) Top-view, not to scale. Taken from [Poh20].

Figure 2.8 depicts how the Crystals surface interacts with the electron beam to generate a pattern by Ewalds sphere construction. k_0 is the wave vector of the impinging electrons. As these electrons are suspected to scatter elastically the resulting wave vectors have the same magnitude. All of these vectors end on a sphere, called Ewalds sphere, with radius $|k_0|$.

$$|k_0| = \frac{1}{\hbar}\sqrt{2m_0E + E^2/c^2} \tag{2.15}$$

For the used energies the resulting radius is about 400 times larger compared to unit cells of regular cubic semiconductors [Poh20], cutting the zones almost perpendicular. Assuming äquidistant atoms, the Fourier transform yields planes. Intersection with these planes in k-space are so called Laue circles or zones (see Fig. 2.8). As the surface is 2D these planes reduce to truncation rods resulting in spotty or streaky intersections and patterns on the screen.

Different surface morphologies yield different RHEED patterns. Fig 2.9 depicts some of the possible combinations. A perfect flat surface yields sharp spots on Laue circles. For this work we expect growth with domains due to the APD's in 3C-SiC. Therefore, a perfectly flat surface would correspond to streaks.
A 3D surface also produces spots but they don't follow Laue circles anymore but depict the reciprocal lattice. Therefore, also growth mode can be approximated with the help of RHEED observations.
As already discussed in section 2.1.1, Nitrides have a high chance to generate hexagonal inclusions on <111> facets. This can also be monitored by RHEED as the hexagonal phase produces different reflexes (see Fig. 2.10).

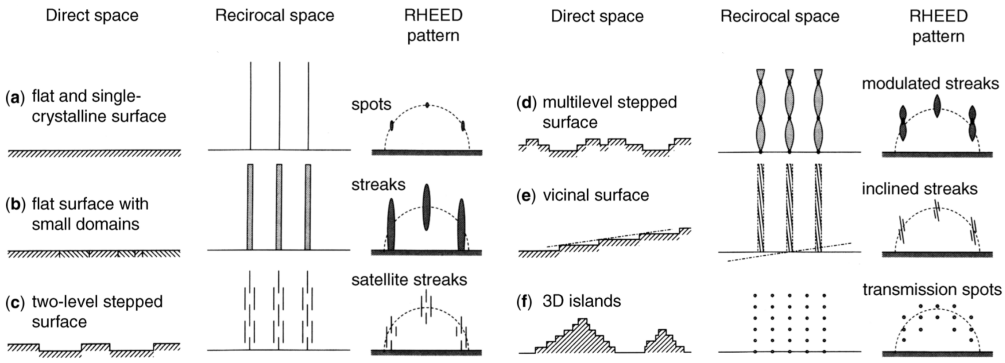

Figure 2.9: Schematics of various kinds of surfaces, in real-space (direct space) morphology, in reciprocal space, and their RHEED patterns, respectively. Taken from [Has12].

RHEED offers the possibility of monitoring the surface wing Nitrides. Figure 2.10 depicts RHEED patterns for different surfaces of grown Nitrides on 3C-SiC. If the sample generates a pattern comparable to Fig. 2.10 a) the surface is very two dimensional (2D) with a low roughness but with APD. Figure 2.10 a) depicts a c-GaN surface grown at very hot conditions (T_s 870°C). The growth mode can considered to be FM (see section 2.2) for pure streaky patterns.

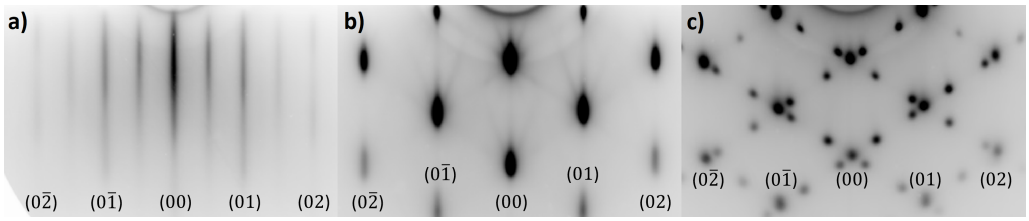

Figure 2.10: RHEED images of different surface morphologies during growth interruptions of Nitrides. a) RHEED image of a perfectly 2D c-GaN surface with APD and 2x2 reconstruction. b) RHEED image of a facetted 3D c-InN surface with streaks indicating APD and facetation. c) RHEED image of a 3D c-InN/h-InN surface with reflexes correspoding to a lot of hexagonal growth on <111> facets.

If growth is not optimal it turns to SK or even VW mode with growth of individual islands. Within some limits, growth can still be reverted to FW growth mode. Nucleation results in a three dimensional (3D) surface that turns 2D after coalescence. The as nucleated islands are often confined by <111> facets resulting in streaky connection lines between the reflexes. While the perpendicular streaks correspond to APD's the streaks connecting the cubic reflexes are caused by the aforementioned <111> facets. Figure 2.10 b) depicts a c-InN surface with a rough 3D surface and a high Stacking Fault (SF) density.
If growth is not reverted to 2D it can get out of control resulting in formation of hexagonal nuclei on <111> facets as can be seen in Fig. 2.10 c). It depicts a surface with a phase mixture of c-InN and h-InN. Streaky connection lines between cubic reflexes are replaced by spotty reflexes of much shorter distance. These additional reflexes can be denoted to the hexagonal GaN phase. It is (0001) h-GaN grown on <111> facets of c-GaN.

2.3.2 High Resolution X-Ray Diffraction

In order to analyze the structure of a Crystal, X-Ray Diffraction (XRD) is utilized. The basic principle of XRD is Braggs equation.

$$n\lambda = 2 \cdot d_{hkl} sin\theta \tag{2.16}$$

With λ the wavelength of the primary beam, d_{hkl} the diffracting lattice plane spacing and θ the samples tilt off the primary optical axis or diffracting angle.
Braggs equation describes the possibility of constructive interference for an optical path difference of $n\lambda$ in thin films. Every lattice plane can be approximated as a thin film for X-Rays with sufficient energy (short wavelength). If one varies θ constructive interference is a result of the structural properties of the crystal itself, resulting in individual and discrete reflexes for every crystalline material.
The structure of a crystal is taken into account by d_{hkl}. The effective spacing of lattice planes depends on the structure of the crystal (cubic, hexagonal, ...), on the Miller index of the planes normal vector and on the lattice constant of the Crystal.

$$\frac{1}{d_{hkl}^2} = \frac{h^2+k^2+l^2}{a^2} \quad ; \quad \frac{1}{d_{hkl}^2} = \frac{4}{3}\frac{h^2+hk+k^2}{a^2} + \frac{l^2}{c^2} \tag{2.17}$$

Eq. (2.17) shows the relation for d_{hkl} for cubic (left) and hexagonal (right) primitive unit cells giving the lattice spacing with respect to lattice constants and the Miller indices. Combining (2.16) and (2.17) allows for identification of a Crystals structure, phase and orientation if the wavelength λ is known.

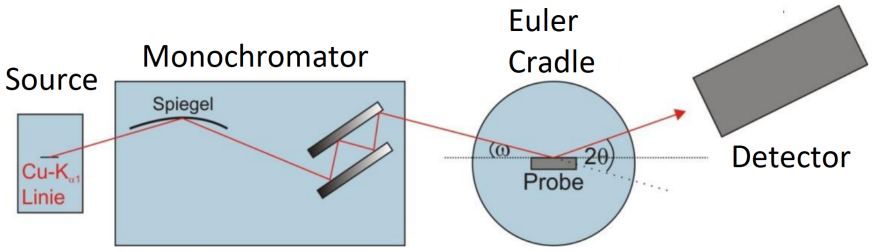

Figure 2.11: Schematic of the HRXRD apparatus. The X-Rays are generated by a sealed copper tube. Copper k_α line is filtered by a hybrid Ge (220) monochromator. The Euler cradle allows precise movement of the sample in all directions. Radiation is detected by an Malvern Xcelerator, made of a X-Ray sensitive CCD array[Wec13].

Figure 2.11 depicts a scheme of the Panalytical X'Pert HRXRD apparatus. Xrays are generated by a sealed copper tube. Afterwards copper k_α is filtered out by a hybrid Ge (220) monochromator combining monochromation and collimation of the

line focused beam. The beam-divergence is about 47 arcsec and λ=1.54Å.
A Euler cradle with a high resolution goniometer is working as a manipulator for the samples and can be moved along 7 degrees of freedom.
That would be the sample tilt and detection angle ω and 2θ, the rotation around the optical axis χ, the rotation around the samples surface normal φ as well as the 3 spacial dimensions x,y and z.

Before each measurement all degrees of freedom have to be carefully adjusted to achieve maximum intensity and high signal to noise ratio. Especially when it comes to measurements on thin films good adjustment is crucial. Detection is done by a X-Ray sensitive diode array called X'Celerator. Among the basic measurement modes are the ω scan (Rocking curve) and the coupled $\omega - 2\theta$ scans, where $\omega = 2\theta + offset$. Such scans are used to measure defect densities and identify crystal phases of poly crystalline samples with the help of Braggs equation. Regular c-GaN Films of 1 μm thickness exhibit defect densities of $10^9/\text{cm}^2$ and hexagonal phase contents well below 1%. For crystalline samples one has to measure so called Reciprocal Space Maps (RSM). Figure 2.12 depicts the FWHM of rocking curves from different c-GaN epilayers grown on 3C-SiC. The inset shows a typical rocking curve. The Full Width at Half Maximum (FWHM) is a direct measure of the dislocation density. The dislocation density and FWHM of the rocking curve develop inversely proportional with the layer thickness d. The solid line gives the theoretical minimum of dislocation density under the assumption of a dislocation glide model from Ayers et al. [Aye95].

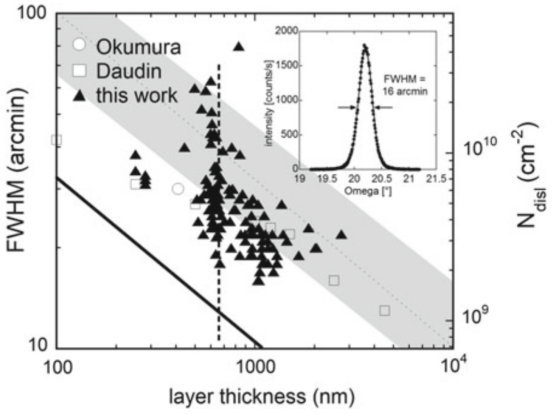

Figure 2.12: Rocking Curve linewidth of c-GaN layers on 3C-SiC (001) versus epilayer thickness[Kem14].

Dislocation density is also reduced during growth by SF annihilation. If opposing defect planes meet they can annihilate [Lee19a]. The figure shows that there is still room for improvement but state of the art c-GaN films cluster around the squares approaching the theoretical minimum.
This means that even perfect growth conditions would still result in dislocation densities around $10^9/\text{cm}^2$, rendering cubic Nitrides noncompetitive for device applications.
Besides rocking curves, HRXRD also allows to collect RSM's due to the very precise goniometer. Imaging XRD reflexes in 2 dimensions depicts the reciprocal lattice of the Crystal. The recorded RSM's allow to estimate additional information like strain, tilt, composition of ternary compounds and more.

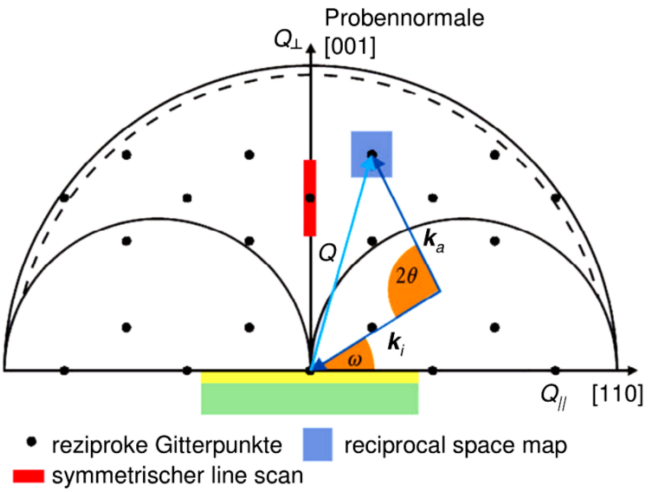

Figure 2.13: Schematic of reciprocal space accessible by HRXRD[Wec13].

In general the reciprocal space is defined by vertical and parallel lattice vectors $Q_\perp$ and $Q_\parallel$. Symmetric and asymmetric scans are seperated. Symmetric scans only scan along (0,0,l) reflexes while asymmetric scans include all possible (h,k,l) planes. While symmetric maps are sophisticated to estimate structure, phase and tilt of the layer asymmetric scans allow to determine composition, strain, mosaicity and more.
Figure 2.13 depicts all allowed and accessible reflexes of reciprocal space. To map the reciprocal space a bunch of $\omega - 2\theta$ scans are collected with different offsets. With the help of the following formula a RSM can be generated from those line scans.

$$Q_\perp = \frac{2\pi}{\lambda}\left(sin(2\theta-\omega)+sin\omega\right) \;;\; Q_\parallel = \frac{2\pi}{\lambda}\left(cos(2\theta-\omega)-cos\omega\right) \tag{2.18}$$

In this work RSM's will be mainly used to estimate hexagonal phase content of inclusions in the cubic GaN layers. Figure 2.14 depicts RSM's measured on cubic GaN samples grown on 3C-SiC under different conditions. The left RSM, grown under unoptimized conditions, shows hexagonal inclusions on the SF of the c-GaN layer. SF appear as streaks intersecting the (002) reflection. Intensity maxima on those streaks correspond to inclusions. Those hexagonal inclusions are missing in the right RSM from a sample grown under optimized conditions. As the hexagonal inclusions are oriented they would not appear in symmetrical line scans (see Fig. 2.13). Cubic phase content is approximated by calculating integral peak intensities of the cubic GaN phase and of all observable GaN reflexes along both azimuths ($\varphi = 0$,$\varphi = 90°$).

$$\frac{c-GaN}{GaN} = \frac{\sum I(c-GaN)}{\sum I(GaN)} \tag{2.19}$$

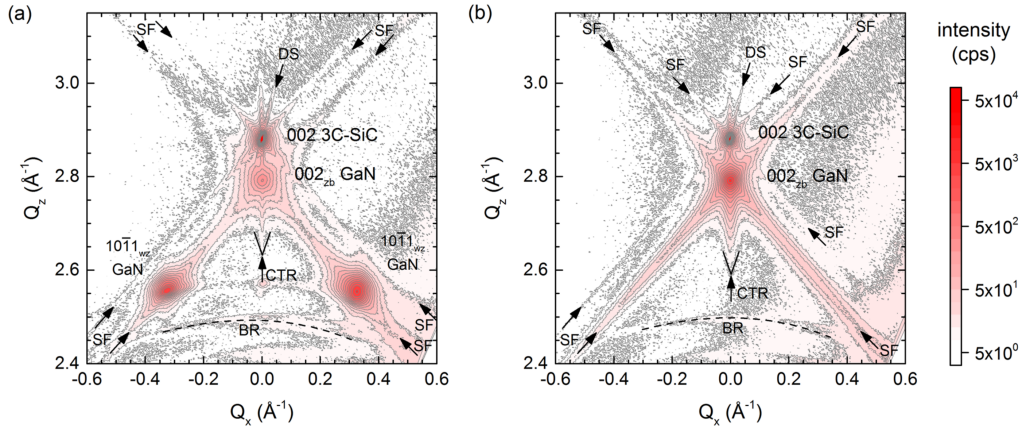

Figure 2.14: Measured symmetric (002) RSMs of cubic GaN samples grown under (a) non-optimized conditions which promote hexagonal inclusion formation, and (b) optimized conditions, which gives close to 100 % pure cubic GaN, with Stacking Fault (SF) streaks, Detector Streak (DS), Crystal Truncation Rod (CTR), and Bragg-ring (BR)[Fre17].

2.3.3 Atomic Force Microscopy

Atomic Force Microscopy (AFM) is a widely used technique to image surfaces down to atomic scales. It exploits interatomic Van-der-Waals forces between sensor and sample to create a topographic image of the surface. Resulting Lennard-Jones potential helps to understand operating modes of AFM's. In general it describes chemical potential of weakly bound particles. The tip is attached to a cantilever whose bending can be attributed to the Lennard-Jones force and its amplitude can be measured by laser interferometry.

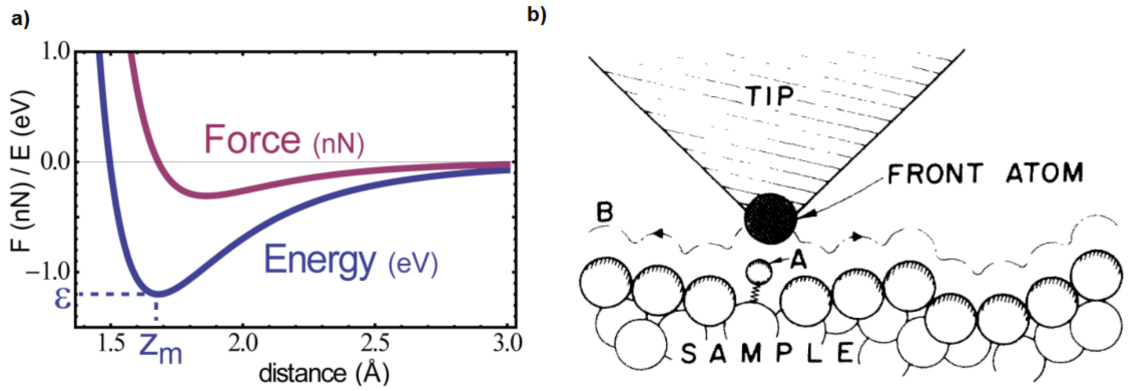

Figure 2.15: a) Model of Lennard-Jones potential (blue) and derivated Lennard-Jones Force as a function of interatomic distance. z_m and ε are binding distance and energy respectively. b) scheme of the AFM needle over the samples surface [Bin86; Lot13].

Operating modes are contact and non-contact mode. In contact mode the AFM needle is in physical contact with the surface with a distance smaller then z_m. This close contact exerts a repelling force onto the needle bending the cantilever. Amplitude is kept constant and piezoelectric motors scan the whole surface. Piezovoltages can be used to calculate an image afterwards. In non-contact mode the distance between tip and surface is larger then z_m. At this distance Lennard-Jones force is attractive and the cantilever can start to oscillate. Surface topology influences resonance frequency which can be measured to calculate an image.
Within this work we use AFM in contact mode to measure the mean surface roughness of our as grown GaN samples. State of the art c-GaN films have roughnesses in the order of nanometers. The measure for surface roughness is the root mean square height (Sq, RMS) which is representative for the standard deviation of heights.

$$S_q = \sqrt{\frac{1}{n}\sum_{i=1}^{n} y_i^2} \tag{2.20}$$

With y_i deviation from surface mean height. Sq is also dependend on the absolute

area as larger areas tend to include more artefacts the RMS is usually bigger compared to measurements on smaller areas.

2.3.4 Electron Microscopy

Electron microscopy is a modern imaging technique that was developed and improved for decades. The idea is to use some sort of probe, able to interact with smaller structures then light. Electrons can be utilized to analyze matter down to atomic scales nowadays. The electrons act as a very fine probe for either the surface or the internal atomic structure of the specimen.

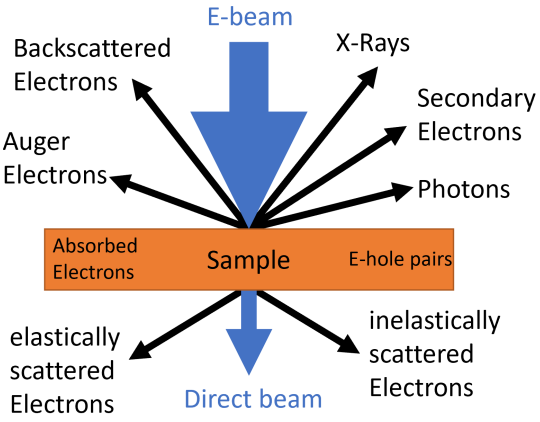

Figure 2.16: Fundamental interactions of electrons with a solid surface. Adopted from [Sci].

Fig 2.16 depicts the possible reactions happening if an electron beam hits a solid sample. In backscattering geometry auger electrons, backscattered electrons, X-Rays, secondary electrons and photons are observable. From Auger electrons, X-Rays, Photons and secondary electrons one can achieve information about the chemical properties of the sample like composition and surface states or reveal the presence of adsorbates e.g. carbon. Backscattered electrons can be employed to generate a topological picture of the surface [Ard38].
For the transmitted electrons it is possible to measure the elastically and inelastically scattered electrons. For thin samples, allowing transmission of electrons, one can reveal structural properties like phase, lattice constant and more.
Backscattering obervations usually refer to Scanning Electron Microscopy (SEM) while transmission measurements correspond to Transmission Electron Microscopy (TEM).
Figure 2.17 depicts the two most prominent electron microscopy setups, namely SEM (left) and TEM (right). In both setups there is an electron source, usually realized by a hot filament. The generated free electrons are accelerated by an anode to form a beam, followed by one or multiple condensor lenses. In the SEM setup condensor lenses as well as objective lenses and x,y displacement coils focuss the beam down to a few nanometers. This fine electron probe can then be used to scan the sample. Backscattering and secondary electron detectors allow to plot the backscattered intensity over x,y creating a morphological picture of the surface down to atomic scales. Besides that some SEM setups have the possibility to detect X-Rays emitted from the sample. This X-Rays have characteristic energies depending on the irradiated material (EDX) and can be analyzed to identify the elements the specimen is made of. In the TEM the electron beam is collimated and then sent through a

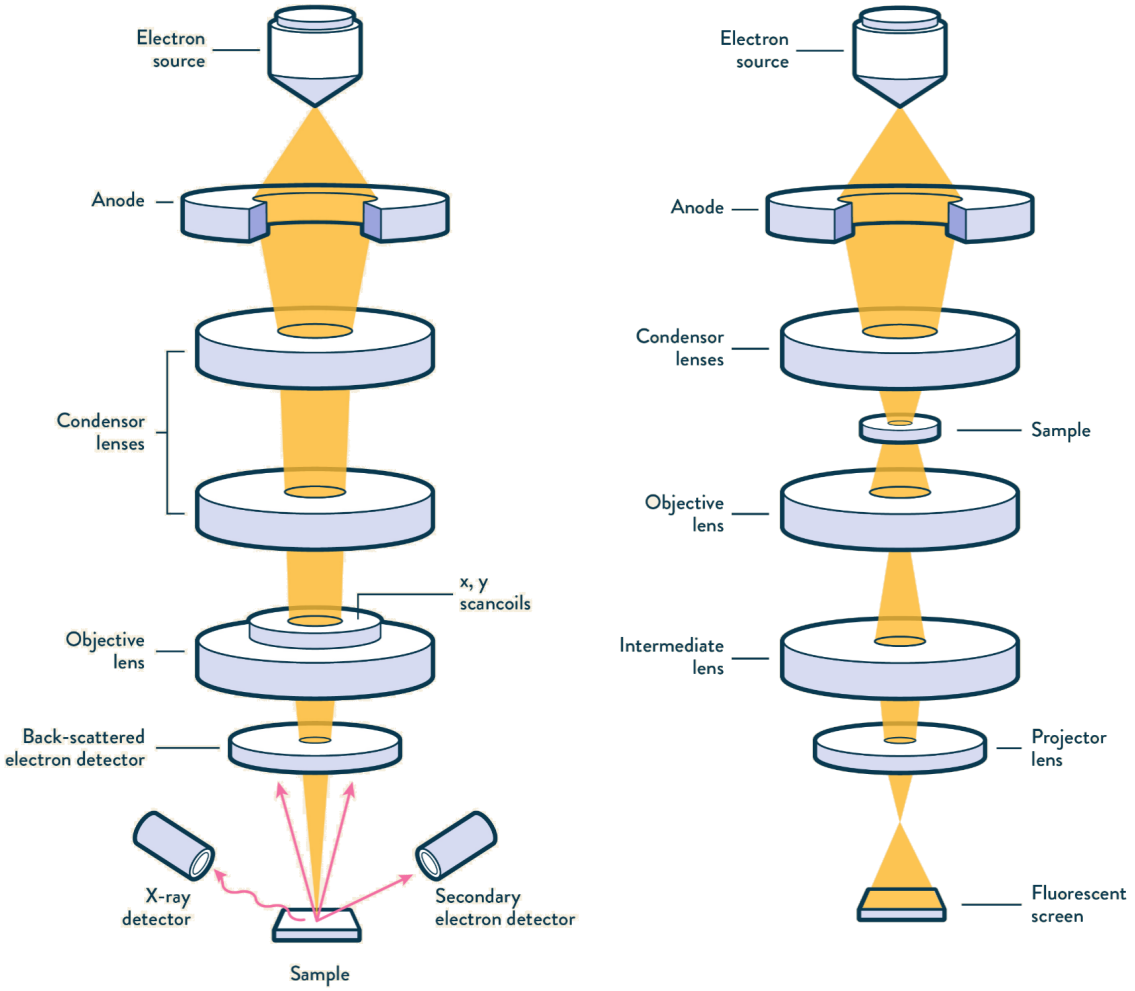

Figure 2.17: Schematic depicting the SEM (left) and REM (right) apparatus setups. The main difference between both devices is scattering geometry. While SEM measures backscattered electorn to depict the morphology of a sample, TEM measures transmitted electons to resolve a samples internal structure[Gle20].

thin sample. Afterwards the beam is projected on a fluorescent screen to see how the electrons interact with the sample. In transmission one can achieve higher resolutions and also measure structural properties like interatomic electrical fields, defects, phase relations, EDX with atomic resolution and more. Nevertheless, TEM requires samples to be extremely thin and therefore, sample preparation is time consuming and expensive. Also the operation of a TEM is way more complicated then operation of a SEM.

2.3.5 Photoluminescence Spectroscopy

Luminescence describes the possibility of matter to emit light due to chemical or physical interactions. Luminescence is categorized by the origin of excitation. E.g. bioluminescence of algae as a form of chemiluminescence, where the reaction of Luciferin and Luciferase with certain photo proteins creates light visible to the human eye [Had10]. Description of physical (photo)luminescence follows [As03; Poh18; Sch02].

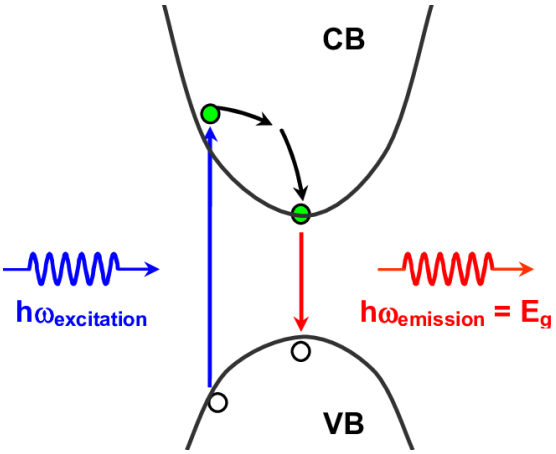

Figure 2.18: Shows absorption of electrons and emission of photons [Jac22].

In a physical perspective luminescence is referred to any radiative recombination from excited electronic states. Excluded are reflections, blackbody radiation and lasing. If a material is irradiated by sufficiently energetic photons for excitation, it's called photoluminescence. If electrons are exciting the process is called cathodoluminescence. Excitation by carrier injection is called electroluminescence. High fields can also cause luminescence by impact ionization resulting in arc discharges. It is also possible to excite gas discharges within bubbles squeezed by pressure changes, called sonoluminescence [Cru15]. Photoluminescence spectroscopy measures the emitted light intensity as a function of the wavelength after excitation. Photons with energy above the irradiated materials bandgap E_g can excite an eletron hole pair, elevating an electron from the valence band to a state within the conduction band (see Fig. 2.19). The final state is depending on the energy of the absorbed photon. In most cases heavy holes are excited as they have the highest density of states (DOS).
As the exciting photons have a larger energy then E_g, the excited electrons have excess energy. This energy is distributed by generating heat (phonons) in the crystal lattice. This process is called thermalization [As03]. These photon-electron interactions cause the electrons to relax towards the band edges. After thermalization recombination of electron and holes emits a photon with the bandgap energy of the material E_g.
Electron hole pairs can also recombine through nonradiative processes e.g. impurity scattering. Within this thesis only radiative recombination is examined. Those transitions are listed in the following tabular.

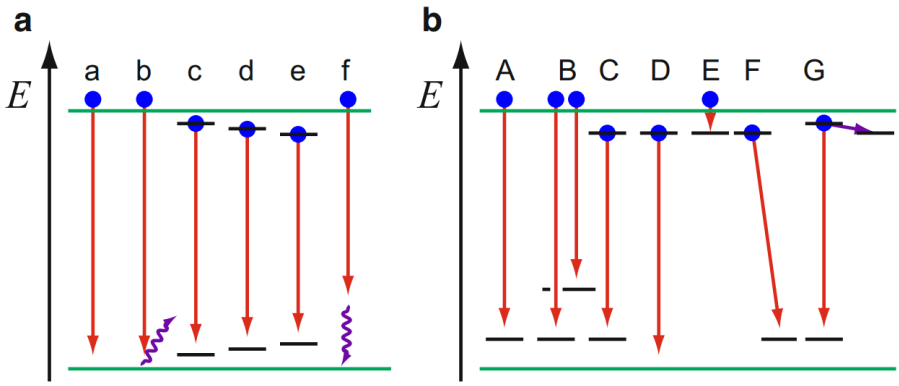

Figure 2.19: Possible radiative intrinsic (a) and extrinsic (b) interactions of electrons and holes emitting photons[Poh18].

intrinsic	extrinsic
(a) Direct band to band	(A) Band to impurity
(b) Indirect band to band	(B) Band-to-multilevel impurity
(c) Free exciton	(C) Excited state to ground state of a localized defect
(d) Free-exciton molecule	(D) Donor-to-valence band, similar to conduction-band-to-acceptor
(e) Electron-hole liquid	(E) Conduction-band-to-donor, similar to acceptor-to-valence band
(f) Phonon-assisted band edge	(F) Donor-acceptor pair
	(G) Bound exciton

Table 2.2: Possible intrinsic and extrinsic transitions (see fig. 2.18).

2.4 Lithography

Within this chapter the very basics of e-Beam and UV (Photo)lithography will be explained as both techniques will be utilized to pattern the SiO_2 masks. All of the following descriptions follow Levinson [Lev11]. The term Lithography is old and historically refers to engraving patterns into stone to create certain images. In a more modern sense Lithography describes patterning of integrated circuits on wafers. This process is crucial for manufacturing of modern semiconductor devices and circuits. Figure 2.20 depicts the steps necessary for lithographic processes. Some of them are optional (italics). First adhesion of the so called resist has to be promoted. Not all resists stick to all surfaces very well. In our case surfaces are sufficiently prepared by wet chemical cleaning steps. Once the surface is cleaned the sample is coated with the resist. A small droplet of the liquid resist is deposited onto the surface. The sample is then spun around its normal axis with very high frequency to spread the droplet and remove excess resist. Once the solvent evaporated it leaves a thin film of resist, typically in the range of 0.1-2 μm thickness. After coating, the sample has to be aligned to a reference point as multiple lithographic steps can be necessary to form a device. In our case alignment is very important to align the structures to crystallographic directions, e.g. grooves parallel or perpendicular to [-110] crystal direction.

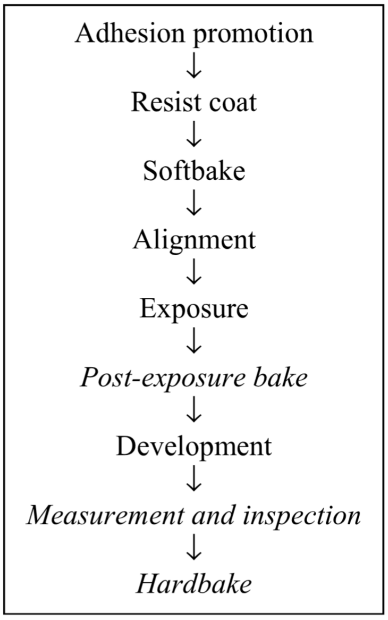

Figure 2.20: Steps within lithography process. Italic steps are optional. [Lev11]

Once the sample is aligned it is exposed. There are different techniques for different resists which will be explained later. Resists are either soluable with or without exposure. Positive resists are normally insoluble in developing chemicals. They become soluble once exposed. After development exposed parts of the resist is removed by developing. Negative resists get insoluble by exposure. After development everything unexposed will be removed. By exposing different regions of the resist film selectively, patterns like circuits are imprinted onto the surface. In some cases a post exposure bake can be helpful to drive additional chemical reactions or change the composition of the resist. The development step removes exposed or unexposed parts of the resist film, depending on the used resist (positive, negative). In most cases this is done by just dipping the sample into a certain solvent. After developing the sample is measured and inspected to control patterning quality. It is then ready for further processing like hardbaking, etching or deposition steps. Different methods of optical and electronic exposure will be explained in the following sections.

2.4.1 UV Lithography

In order to pattern a resist coated surface it is selectively exposed with photons of sufficient energy. The most common technique is utilizing photomasks for patterning. In this work we utilized an optical mask writer, both techniques will be roughly sketched within this section. To achieve small structures, down to micrometer scales, UV light sources are employed.

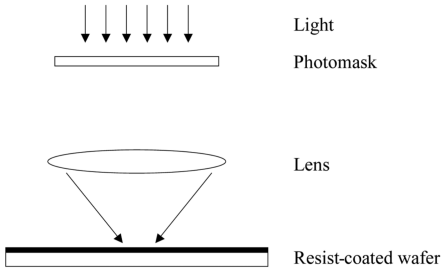

Figure 2.21: Schematic of Lithography utilizing Photomasks. [Lev11]

Figure 2.21 depicts a scheme of an optical lithography setup. Light is irradiating a photomask. Unblocked light is then projected onto the resist-coated wafer by a lens. This technique was developed to pattern wafers fast. Once a field is exposed the wafer can be moved and the next field is exposed. Nevertheless, this demands a proper photomask and most applications require individual masks first.
Optical mask writers are another way of patterning resist-coated wafers. Figure 2.22 depicts such a system. A UV Laser is focussed by different optics and then aligned towards a stage. The stage is precisely controlled and can move the substrate under the beam. By scanning the substrate arbitrarily chosen patterns are imprinted into the photo resist allowing for testing of geometrical parameters of structures before converting to photomasks for mass production. This is also very beneficial for research. In this work such a mask writer was used to pattern Si masked with SiO_2.

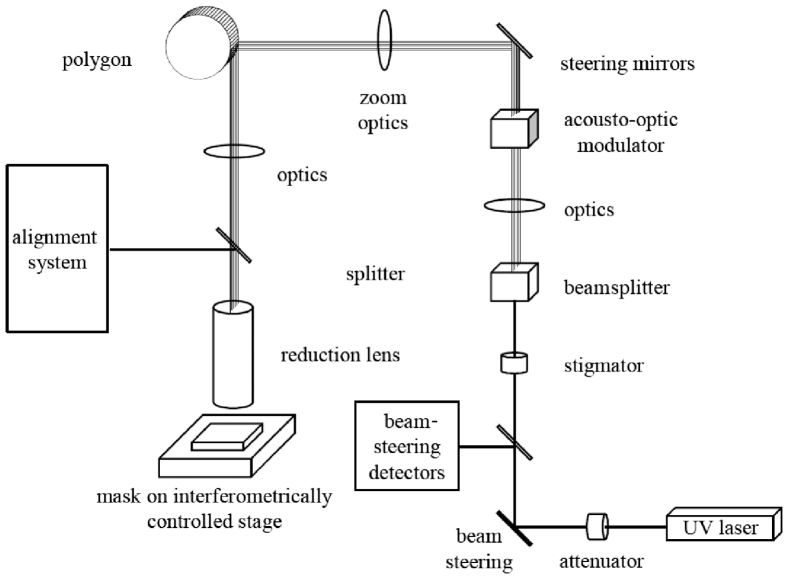

Figure 2.22: Schematic of optical mask writer architecture of ATLA. [Lev11]

2.4.2 Electron Beam Lithography

The principle of Electron Beam Lithography (EBL) is to use electrons instead of light as they can be focused to much smaller beam diameters compared to light. The setup is very comparable to a regular SEM but the stage is much more precise. Figure 2.23 depicts an EBL setup. For high resolution applications electrons are emitted by a thermal field emission source and accelerated with energies up to 200 keV. Afterwards the electrons are focussed by several deflectors and apertures. Typical Beam diameters of 10-20 nm can be achieved. The electron beam scans the sample irradiating the electron resist. For highest resolution Gauß shaped beams are utilized.
One problem with e-beam lithography is electron scattering. Electrons not only interact with the photoresist but also with the substrate below. Backscattering from substrate and the beam objective can irradiate the resist at unwanted locations. Also structures written very close to each other interfere due to the so called proximity effect (see Fig 2.24). Electrons backscattering out of the substrate interact with photoresist that still has to be exposed. Due to this the resist can be overexposed and therefore weakened. To guarantee structural sizes this effects are taken into account by state of the art devices and are compensated.
The e-beam focus is also very sensitive to the working distance, making it necessary to precisely align the sample before patterning. This method of patterning is comparably slow. The maximum beam speed for the utilized e-beam lithography system is 4 mm/s. Patterning of a 1x1 mm^2 field with grooves takes about 10h.

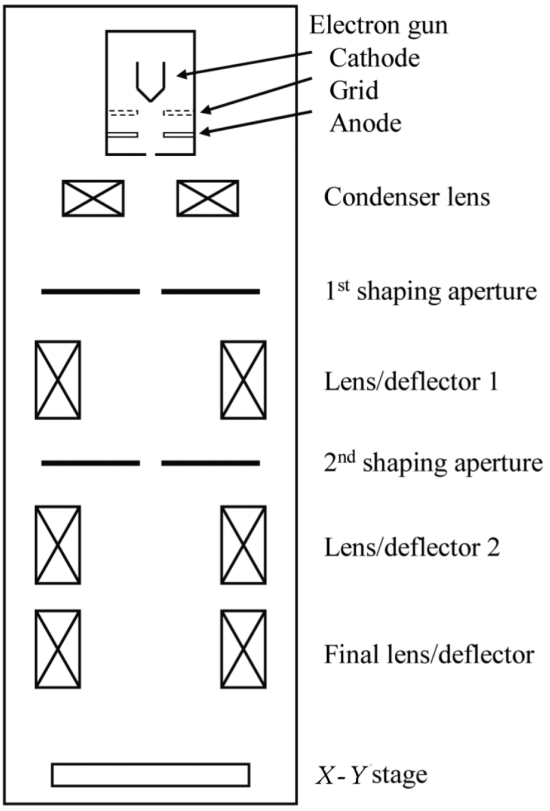

Figure 2.23: Schematic of an electron optical system for mask writing. For electron writers where throughput is a priority, the electron source is a thermionic emitter (such as lanthanum hexaboride), while systems designed for extremely high resolution employ thermal-field emission sources.[Lev11]

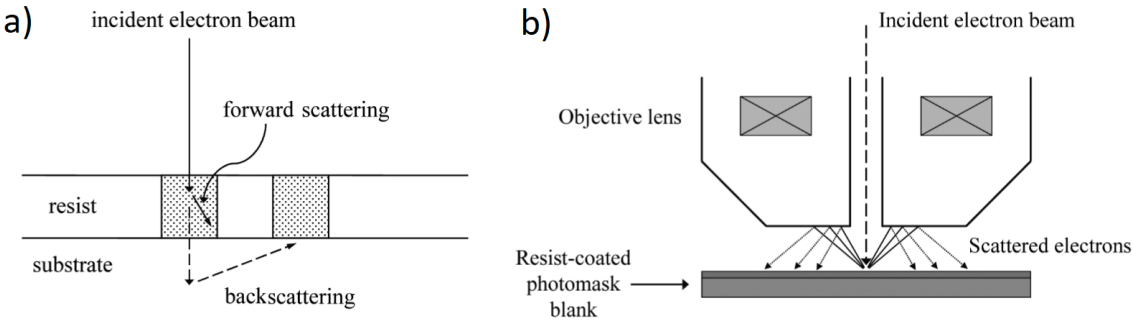

Figure 2.24: a) Backscattered electrons irradiate target areas (grey) and adding unwanted dose, causing the proximity effect. b) Double backscattering of electrons from the objective also exposes the resist. [Lev11]

2.5 Reactive Ion Etching

Reactive Ion Etching (RIE) or dry etching describes a technique for removing material from a substrate utilizing the plasma reaction of certain ions. The plasma presents a condition where one or more gases are ignited due to an external electrical potential applied, causing partial ionization of the gas atoms. Within the plasma, positive ions, radicals and electrons co-exist [Kar14]. This process utilizes physical and chemical effects like ion bombardement, ion-induce damage, spontaneous chemical etching, radical generation, film deposition and more. All of the mentioned effects contribute to the etching performance [Lae20]. The etching consists of two dominant processes. On one hand accelerated ions sputter the sample removing atoms physically. On the other hand activated radicals from the plasma can chemically react with the surface atoms and create volatile radicals that evaporate off or form passivization layers. Passivization layers can also be deposited and selectively sputtered by adding gases like Argon or Oxygen to the plasma. Fine tuning of RIE parameters allows to carefully weight chemical and physical etching to determine the etched profile.
In contrast to wet etching, dry etching is beneficial in terms of reproducibility, uniformity, throughput and anisotropy [Kar14; Lae20]. Investements and progress were high for RIE, especially because of the possibility of anisotropic etching without being dependent on crystallographic orientations. This also allows for lithographic transfer of well defined patterns with very small structure sizes. As the process happens in vacuum chambers it is also clean and beneficial for device processing [Jan12].
The parameters available for RIE are the chosen gases and their flow rates, RF and ICP powers, bias voltage, process pressure and substrate temperature. The outcome of the etch is categorized by the achieved etching rate, the anisotropy or sidewall angle, the masks selectivity, the substrates selectivity, the etched surface quality and the throughput [Lae20]. Most of them are interdependent. E.g. increasing RF Power increases DC bias which leads to the generation of more and faster ions bombarding the surface.Therefore, etching time has to be lowered as etching rate will be higher, but the resulting structure will be etched more anisotropic.

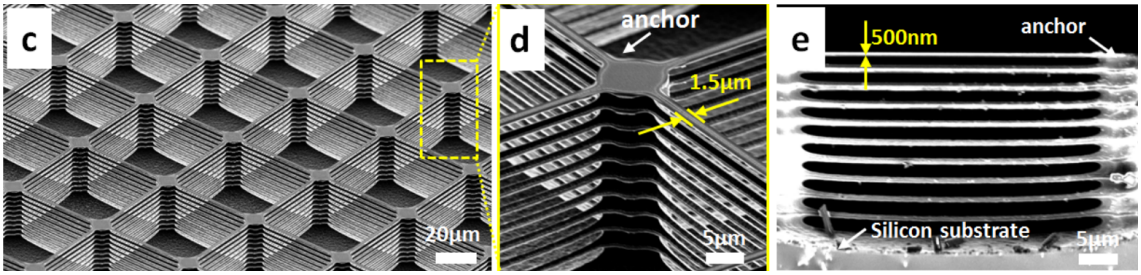

Figure 2.25: (c) Shows the anchor part that holds 10 stacked silicon beams. (d) Zoom in of region in (c). (e) Cross section view of the 3D silicon structures. [Cha18]

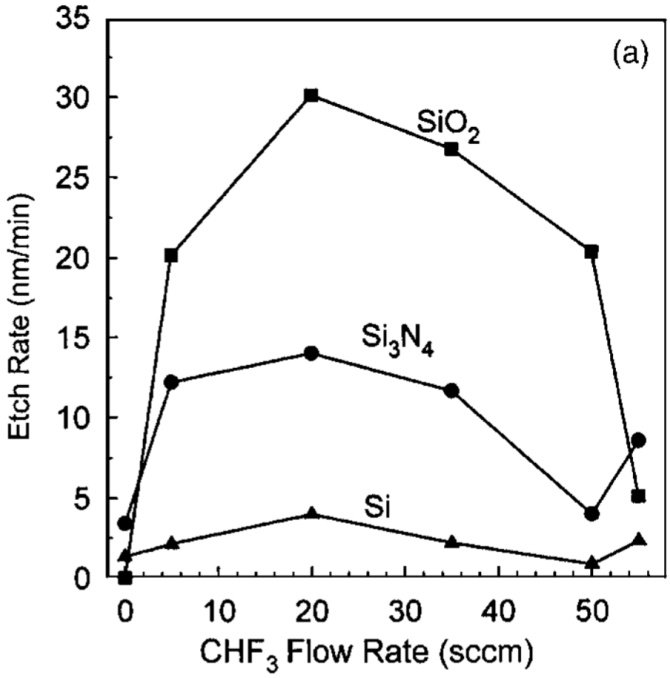

Figure 2.26: Etching rates of SiO_2, Si_3N_4 and Si in dependence of CHF_3 flow rate in a CHF_3/Ar plasma [Gat06]

Most RIE processes on Si and comparable semiconductors utilize chlorides like CHF_3, flourides like SF_6 and more. It is also possible to achieve 3 dimensional structures by RIE procedures. Those are useful for applications like field effect transistors, memory chips, biosensors, photonic Crystals and more [Cha18]. Chang et al. demonstrated this by a so called DREM (deposit, remove, etch, multistep) process on Silicon. They achieved stacks of 10 silicon beams with length of 50 μm, widths of 1.5 μm and thicknesses of only 500 nm. By carefully optimizing each step this complex structure was achieved within a single RIE operation (see Fig. 2.25). In this thesis the goal were rectangular patterns like grooves and holes in SiO_2 and v-shaped grooves in 3C-SiC. Oxides are etched with fluoride based plasmas. Vertical patterns can be achieved by utilizing a mixture of CHF_3 and Ar. Figure 2.26 shows the etchrates of different dielectrics and Si in a CHF_3/Ar plasma with constant gas flow rate of 55 SCCM (cubic centimetre per minute STP), 200 W of RF power and 52 mTorr. From this the high selectivity between SiO_2 and Si is visible. Furthermore it helps to understand the reactions on the surface. The reaction between Si and CHF_3 results in the formation of SiF_i radicals and CF_i polymers (i=1,2,3,...). Volatile compounds like SiF_4 can evaporate and remove substrate material. CF_i polymer layers deposit and act as a protective layer. While this ensures anisotropic etching by polymer deposition on the sidewalls, it also reduces the vertical etchrate. Polymer films introduce a diffusion barrier for F radicals and SiF_4 compounds and by this dampen

the chemical reaction. Depending on the chemistry added ions like Ar or O can either cause ion-inhibitor or ion-induced RIE. If added ions act like an inhibitor they deposit on unexposed areas, like sidewalls, preventing chemical etching. If they act like inducers they help to sputter protective polymer films. Sputtering can promote the chemical reaction [Jan12]. By adding Ar to the plasma the protective polymer layer is thinned by sputtering. This results in the highest etching rates for equal amounts of CHF_3 and Ar being fed to the plasma [Gat06; Tac91]. Addition of noble gas to a plasma can also enhance dissociation of reactive species [Jan12].
The 3C-SiC substrates are etched with SF6 and Oxygen plasma, where oxygen is an additive. This method of etching was analyzed by Hiller et al. [Hil13]. One of the main results was the dependency of the side wall slope on the DC bias and chamber pressure. The lower the DC bias and the higher the pressure the smaller the slope of the side walls. Mario Littmann [Lit] developed a recipe for v-shaped grooves with maximized enclosed angle, approximately dissecting <111> sidewall facets, of 70°. This was achived by reducing DC Bias and increasing chamber pressure which also fits the observations made by Hiller et al.

CHAPTER 3

Experimental

Within this chapter experimental details of patterning and the regular growth of cubic Gallium Nitride (c-GaN) are explained. One of the main goals of this thesis was to achieve V-shaped grooves, exposing <111> facets of the 3C-SiC substrate and to overgrow them selectively with c-GaN. Besides that, the subject was also to reach SAG on <001> facets of 3C-SiC. To fabricate various patterns in SiO_2, acting as a growth mask, different Lithography and RIE steps have to be employed. Therefore, SiO_2 deposition will be covered first, followed by structuring masks on top of SiO_2. The checker board pattern is used to measure the critical substrate temperature for GaN deposition on SiO_2 for fixed Ga and N fluxes. Nanosphere Lithography (NSL) and Block-Co-Polymer Lithography (BCP) are used for patterning of large areas with hexagonal hole arrays of different feature sizes. NSL holes have diameters of 130 nm and BCP holes of 17 nm. Electron Beam Lithography (EBL) is utilized to write grooves with lateral dimensions of 90 nm and barriers of 150 nm. The patterned area is 1x1 mm^2 so the grooves will be 1 mm in length if properly stitched. To conclude the chapter, PAMBE growth of c-GaN is explained. The focus of that chapter is on controlling Ga surface coverage during growth to maintain a Ga monolayer. Despite not being selective it is the most prominent method of c-GaN growth and serves as a state of the art reference for surface morphology and crystal quality [As03; As10; Sch02].
In all our experiments we will utilize different oxides (thermal, plasma deposited) as a growth mask to achieve selectivity. In order to structure the SiO_2, etch masks have to be employed. In our experiments etching will be masked by nickel when applying NSL, by ZEP520A when employing EBL and by Block-Co-Polymers when using BCP Lithography.

3.1 SiO_2 Deposition

Thermal and plasma deposited silicon oxides are employed as growth masks for GaN. Thermal deposition of SiO_2 on Silicon and 3C-SiC is already researched [Dea65; Fun84; Son04]. By heating Si and 3C-SiC substrates to well above 1000°C and supplying an oxygen rich atmosphere, deposition of smooth ($S_q < 1$ nm) and clean SiO_2 is possible. For thermal oxidation a tube stove of AG Meier was used. It can be supplied with either oxygen or nitrogen rich atmosphere. As the stove is mainly used for oxidizing Silicon the parameters for precise films of 200 nm were already known. Si (001) was thermally oxidized dry and at 1100°C for 2h and 53min, resulting in 200 nm of T-SiO_2 (Thermal-SiO_2). Thicknesses were estimated by ellipsometry done

at AG Goldhahn in Magdeburg.
For 3C-SiC (001) the parameters from Fung et al. couldn't be matched as they describe oxidation of hexagonal SiC [Fun84]. Therefore, an oxidation series was carried out to estimate the growth rate of SiO_2 on 3C-SiC (001) at 1200°C which was the highest temperature setting available for the used stove.

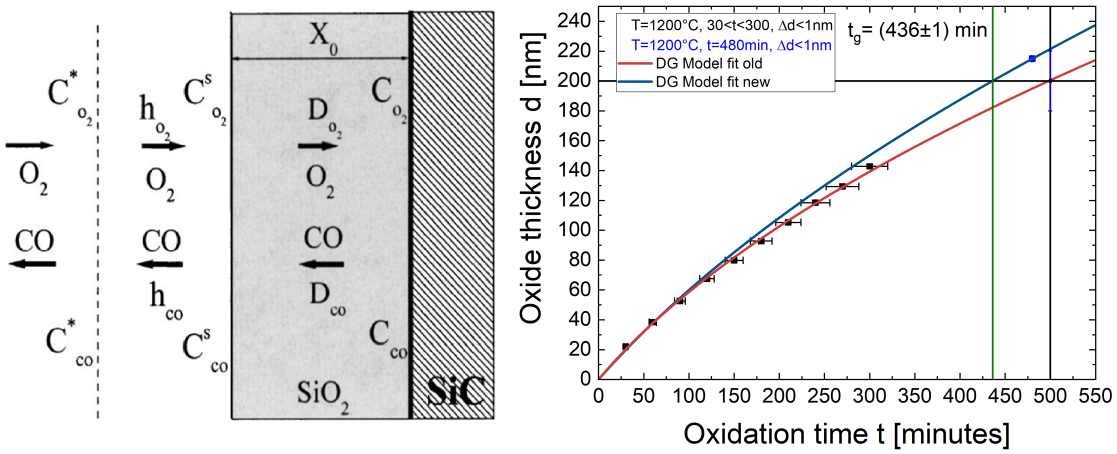

Figure 3.1: (left) Diffusion processes on heated 3C-SiC in an oxygen rich atmosphere [Son04]. (right) SiO_2 film thickness as a function of oxidization time at 1200°C. Red curve fits thicknesses for a consecutive oxidation series. The blue curve fits all samples. The blue sample was oxidized seperately to validate red fit. Oxidation time t_g was found to result in 200nm of SiO_2 on 3C-SiC.

This process was first described by the Deal-Grove Model [Dea65] for Silicon. Figure 3.1 (left) shows a scheme of this process for SiC which is very similar to the thermal oxidation of Silicon. Arrows indicate material fluxed and * indexes represent concentrations at the respective interface. By excessive heating Si-Si and Si-C bonds break without melting. If oxygen is supplied, the free sites can be occupied to form Si-O bonds. The initial oxide growth rate is only limited by the speed of the chemical reactions happening to dissociate substrate bonds and form SiO_2. Once this process is completed in the vicinity of the surface, the reaction front moves into the substrate while the SiO_2 film thickness X_0 increases. At some point the growth becomes diffusion limited as reaction educts (O_2) and products (CO) have to diffuse through the already grown SiO_2 film. For that reason Deal and Grove described the film thickness as a function of time to have a linear and parabolic component. The thicker the already grown film the longer the diffusion times from the surface towards the interface, thus growth is slowing down. Linear and parabolic regime are separated by a characteristic time, adverting diffusion limiting the speed of chemical reactions forming SiO_2.

The oxides growth rate on SiC is about one order of magnitude slower compared to the growth rate on Si because of several factors. Once the Si-C bond is broken the Carbon has to be removed. This happens by formation of CO molecules and consumes some of the available oxygen for growth of SiO_2. Furthermore, the CO has to diffuse out and CO saturation at the growth interface slows the reaction even further. Together, this results in a much slower growth rate compared to oxidation of Si. Nevertheless, it still can be described with a modified Deal-Grove-Model as the process does not fundamentally change, but involves an additional diffusion. Deal-Grove-Model describes the relation between film thickness X and oxidation time t as following [Son04].

$$X^2 + AX = B(t + \tau) \tag{3.1}$$

$$d = -\frac{A}{2} \pm \sqrt{A^2 + 4Bt}; \tau = 0 \tag{3.2}$$

With τ being related to the initial thickness. B is the parabolic and B/A the linear rate constant. For fitting, formula (3.2) was used. Figure 3.1 (right) shows the experimental results for 2 3C-SiC oxidation tests. First, a series with 10 samples was oxidized in one batch at 1200°C. Every 30 minutes one sample was taken out resulting in oxidation times ranging from 30 to 300 minutes. When removing a sample the whole batch had to be taken out of the stove. Therefore, removing each sample accumulates a 2 minutes error in oxidation time. This series was then analyzed with ellipsometry by AG Goldhahn in Magdeburg. Accuracy of this method is below 1 nm. From this the red curve was extrapolated and yielded an oxidation time of 500 minutes for 200 nm of SiO_2 on 3C-SiC (001). To validate this a single sample (blue) was oxidized without any interruption for 480 minutes. The resulting SiO_2 film was found to be (215±1) nm thick. Taking all 11 samples into account (blue curve) an oxidation time of 436 minutes is sufficient to grow (200±1) nm of T-SiO_2 on 3C-SiC (001) in the available stove.
Plasma deposition of (P-)SiO_2 was done in a plasmalab 80 PECVD apparatus. P-SiO_2 was grown at a rate of (73±3) nm/min. The sample inside the chamber is heated to 300°C. The plasma is operated at 20 W and 1000 mTorr and supplied with 400 SCCM of SiH4 and N_2O. In the case of plasma deposition none of the SiC is consumed. All samples were treated with aceton and isopropanol before and after deposition of SiO_2.

3.2 Checkerboard Pattern

In order to test selectivity, a critical substrate temperature was tested. For a given Ga and N flux the critical substrate temperature denotes a substrate temperature preventing nucleation and growth of GaN on the respective surface. In our case this is the SiO_2 mask.

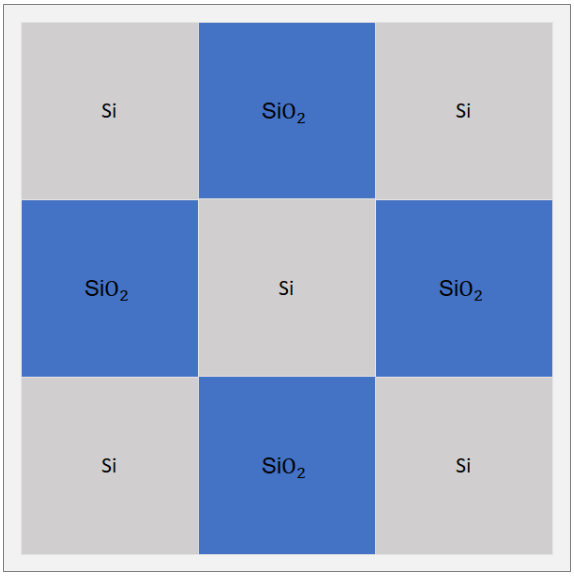

Figure 3.2: Schematic of the checkerboard pattern utilized to test critical substrate temperature for nucleation of GaN for given Ga and N fluxes. Grey areas depict Si and blue areas SiO_2 respectively. While the sample is 1x1 cm^2 every field is 3x3 mm^2.

Figure 3.2 depicts the structure used to test selectivity. 20 pieces of Si (001) were coated with SiO_2. Half of them were oxidized thermally and the other half were covered with plasma assisted deposition. The SiO_2 film thickness was (200±10) nm. The structure was written with maskless UV Lithography by employing a Heidelberg DW66 apparatus, operated by AG Bartley. The used laser has a wavelength of 375 nm. This method allows fast patterning of macroscopic masks. After developing the structure was transfered from the photoresist to the underlying SiO_2 by means of RIE, precisely described in section 3.6. The presented structure not only allows estimation of critical deposition temperature but also to measure diffusion. If there is noteworthy diffusion, from the SiO_2 mask to the substrate, growth rate will increase compared to unstructured reference samples. At least there should be observable thickness differences in the vicinity of the mask. Each sample was overgrown with a Ga flux of about $2{\cdot}10^{14}$ Atoms/cm^2s^{-1} and a Nitrogen flux of half of that. Growth was conducted for 41 minutes. Afterwards, the surfaces of SiO_2 and Si were observed by SEM to estimate the GaN coverage. These series were conducted on Si. After both series, containing 10 samples each, tests on 3C-SiC were done to see if parameters are adoptable. The large feature sizes also allow structural examination of the deposited GaN films.

3.3 Nanosphere Lithography

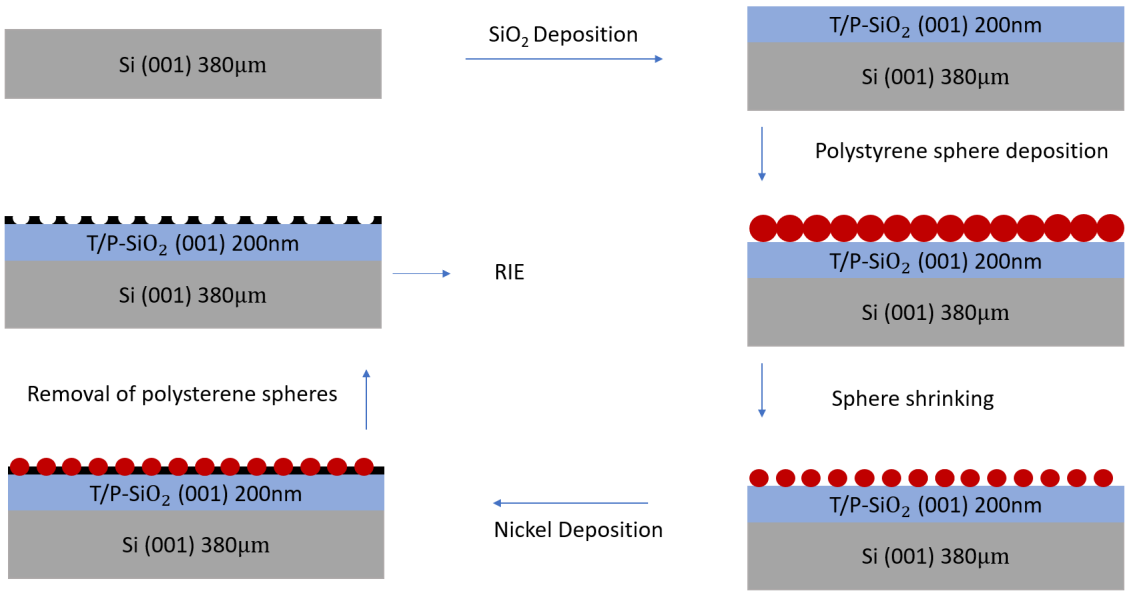

Figure 3.3: Flowchart for structurization of the Nickel hardmask by NSL Lithography.

Nanosphere Lithography was used to structure a hardmask made of Nickel on SiO_2 with small holes on a large area. Samples of 2x5 cm^2 were processed in one step. Nickel serves as a hardmask vor the consecutive RIE etch. Description follows [Bra18].
Figure 3.3 shows a flowchart for NSL Lithography to structure the Nickel hard mask. First SiO_2 is deposited as discussed in Chapter 3.1. Before and after deposition the samples were cleaned in acetone, isopropyl alcohol and deionized water to remove residues. The resulting 200 nm SiO_2 film was then covered by convective self-assembly. This process is done in a home-made apparatus. A droplet of solution with the spheres inside is deposited on the surface and moved with a doctor blade at a constant velocity. If the process parameters adjusted well the resulting polystyrene sphere layer is hexagonally closed packed and 2 dimensional. About 60% of the treated surface is covered with a monolayer of polystyrene spheres. The other 40% have multiple layers of spheres or no coverage at all. After deposition of spheres, their dimensions are further modified with an additional RIE step utilizing an Oxygen and Argon plasma for shrinking them to the nominal diameter of 130 nm. The shrunk spheres then act as a shadow mask during Nickel deposition. In our case we nominally deposit 12.5 nm of Nickel in a self-made Physical Vapor Deposition (PVD) device. Growth rate is monitored with the help of a Quartz Crystal. Metals are evaporated from small boats with a heating current applied. Once the Nickel is deposited, the polystyrene spheres are removed with toluene in an ultrasonic bath. Once the Nickel

hardmask is structurized the sample is etched to transfer the structure from Nickel to SiO_2. Once the SiO_2 etch is done, the remaining Nickel is removed with a wet chemical etch using diluted H_2SO_4 (7:1 ratio Water:H_2SO_4) in an ultrasonic bath at 135 kHz. High ultrasonic frequencies are necessary! Low frequencies can remove SiO_2 from the substrate!

3.4 Block Co-polymer Lithography

Block Co-polymer Lithography (BCP) utilizes mixtures of poly(styrene-b-methylmeth- acrylate) (PS-b-PMMA) with precisely estimated fractions of polystyrene to achieve strucure sizes of about 17 nm. Description follows Brassat et al.[Bra18]. The procedure is depicted in figure 3.4. First a 30 nm layer of

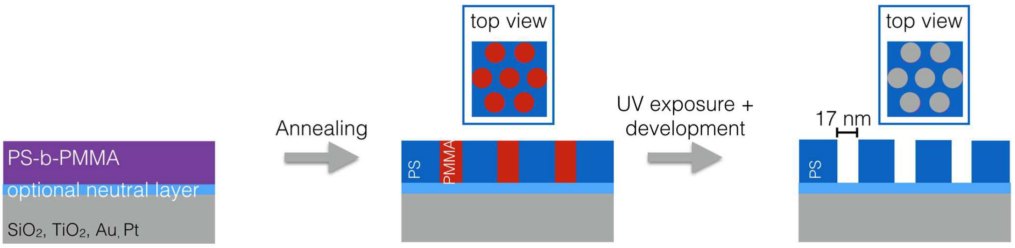

Figure 3.4: Flowchart for structurization with BCP Lithography [Bra18].

PS-b-PMMA is deposited, on the SiO_2 growth mask, with spin coating. Afterwards they are thermally annealed for 24h at 180°C for microphase separation. This leads to PMMA cylinders in a PS matrix. The final step is exposure with UV light for about 20 minutes followed by a 30 minutes etch in acetic acid to remove the PMMA cylinders. The remaining PS mask contains hexagonally close packed holes with nominal diameters of about 17 nm. The remaining PS is then used as a hardmask for RIE of SiO_2. After the RIE step the PS Mask was removed with piranha (H_2SO_5) etch.

Piranha etch is **dangerous** and working with it demands awareness of possible risks. H_2SO_5 is not only corrosive but also an oxidizer. This makes it extremely aggressive for organic compounds (like skin and tissue) and can even lead to fire or explosions if mixed with solvents or water. Also the fume is very corrosive so all experiments were conducted within a fume hood and with protective gear containing very thick gloves, a face shield, an acid resistant skirt and googles.

The Piranha etch is mixed from 3 parts of sulfuric acid (H_2SO_4, 96%) and 1 part hydrogen peroxide (H_2O_2, 35%) by **slowly** adding hydrogen peroxide to sulfuric acid while gently stirring the mixture. This process generates a lot of heat and can even lead to boiling of the acid. To prevent accidents the least possible amount was mixed every time. In our case that was 20 ml, so just enough to submerge a sample. After etching the acid was neutralized by solving 35 g of sodium carbonate (Na_2CO_3) in 100 ml of DI water. The sodium carbonate solution was then added **slowly** to the acid. Neutralizing piranha acid with sodium carbonate leads to generation of excessive heat and foam, caused by CO gas that is a byproduct of the reaction. After neutralizing, pH is about 9 and the mixture can be disposed. Samples were further cleaned by Acetone, Isopropanol and deionized water, each in an ultrasonic bath for

10 minutes. Excess water is blown off the samples with N_2 before loading them into our UHV Chamber.

3.5 Electron Beam Lithography

Electron Beam Lithography (EBL) is carried out in a Raith Pioneer Field Emission Scanning Electron Microscope. Zeon ZEP520A [Zeo] was employed as a positive resist. To coat the sample it is introduced into the spinner and cleaned with acetone, isopropyl alcohol and DI water subsequently while spinning at 800 rpm. Once the sample is cleaned, it is aligned so that the normal axis of the sample is parallel to the rotating axis of the spinner. Otherwise spin coating will result in a defective layer. 50 μm^3 of ZEP520A are deposited on the surface and spin coated for a minute at 5500 rpm. The resulting layer exhibits a thickness of about 380 nm. After spinning the resist is baked for 2 min and 30 s at 180°C in ambient.

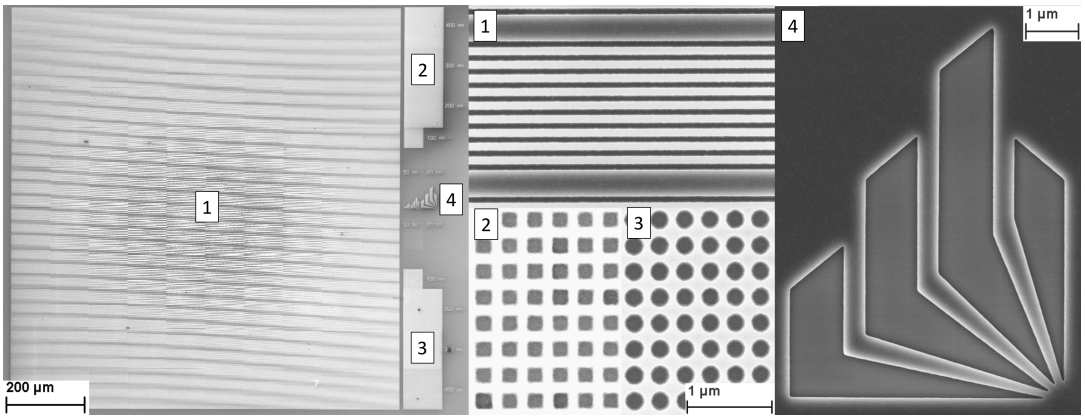

Figure 3.5: SEM images of the final employed patterns transferred into SiO_2 by RIE. (left) Overview with little magnification showing 1x1 mm^2 of grooves accompanied by smaller different hole patterns and a university logo. (middle) Magnified images from the patterned grooves and holes. (right) Magnified image of the university of paderborn logo.

In principle, the sample is ready to be introduced into the UHV chamber of the FESEM at this point, but the sample is scratched aggressively on one edge with a diamond scriber beforehand. The scratch serves as a surface perturbation, allowing focusing of the electron beam. Without the scratch there are no features on the surface to allow proper focusing. Beside that, the scratch acts as a macroscopic orientation and the grooves will always be patterned to point towards the scratch.
Patterning is done with 75 $\mu C/cm^2$ and a beam speed of about 1 mm/s. This results in a total patterning time of 10-12h, depending on the current of the beam.
Once the patterns are written, the resist is developed by a 1 min submerge in n-amylacetat, followed by isopropanol and DI Water rinse. After development of the resist the sample is ready for further processing, e.g. RIE of SiO_2.
Figure 3.5 shows SEM images of the employed patterns. The EBL pattern is discussed with a real SEM image. 90%+ of the patterning time is dedicated to

the 1x1 mm^2 patch containing grooves. Besides the large field of grooves, smaller patches were added to the right side. Besides the grooves, patches contain circular and rectangular holes with arbitrarily chosen diameters ranging from 100 to 400 nm. Furthermore, a university logo was added, with 4 different sizes, just to have large unpatterned areas for comparison.

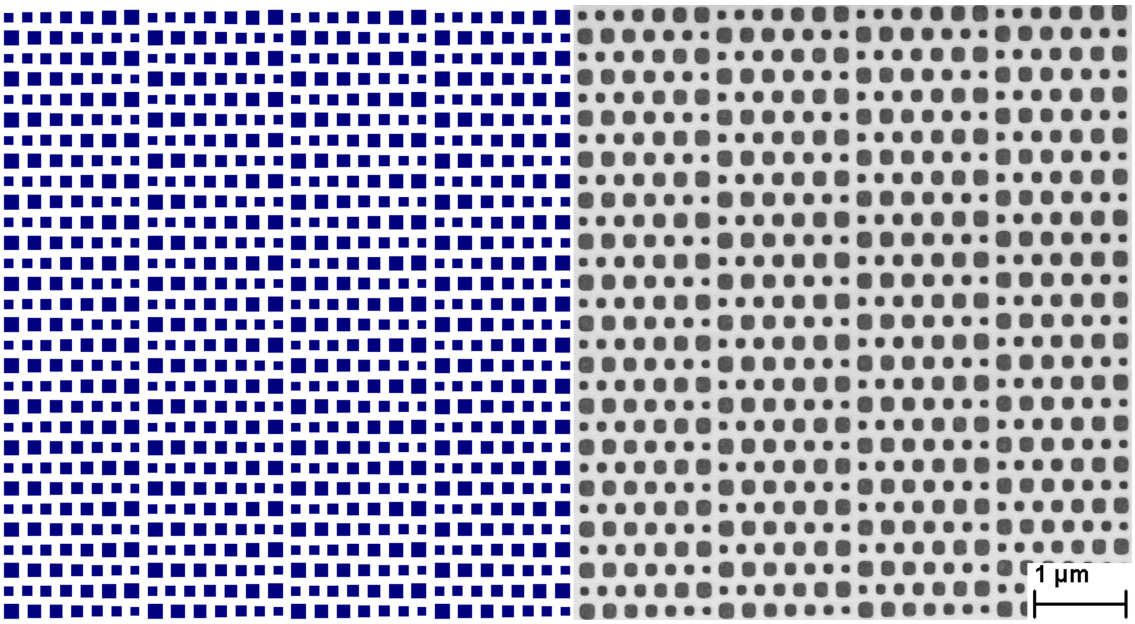

Figure 3.6: (left) Area filling pattern with different opening diameters and constant barriers of 100 nm. (right) SEM image of the pattern transferred into the photo resist.

Additionally, a pattern was designed to test the limits of our PAMBE chamber geometry. Figure 3.6 shows the proposed pattern to precisely estimate the geometrical limits of the chamber. If the aspect ratio is too big, gallium beam cannot reach the bottom of holes, thus nucleation on 3C-SiC gets unlikely. The pattern was easily transferred into the resist (see fig. 3.6 right). From previous observations it was known, that a critical aspect ratio has to be somewhere aroung 1.5 to 2. Aspect ratio is calculated by opening diameter divided by mask thickness. Nominally the holes were designed to exhibit aspect ratios from 1.5 to 2 but such small structures suffer from proximity effects. Therefore, the holes exhibit real aspect ratios ranging from 1.2 to 1.8.

3.6 RIE Patterning of SiO_2/3C-SiC (001)

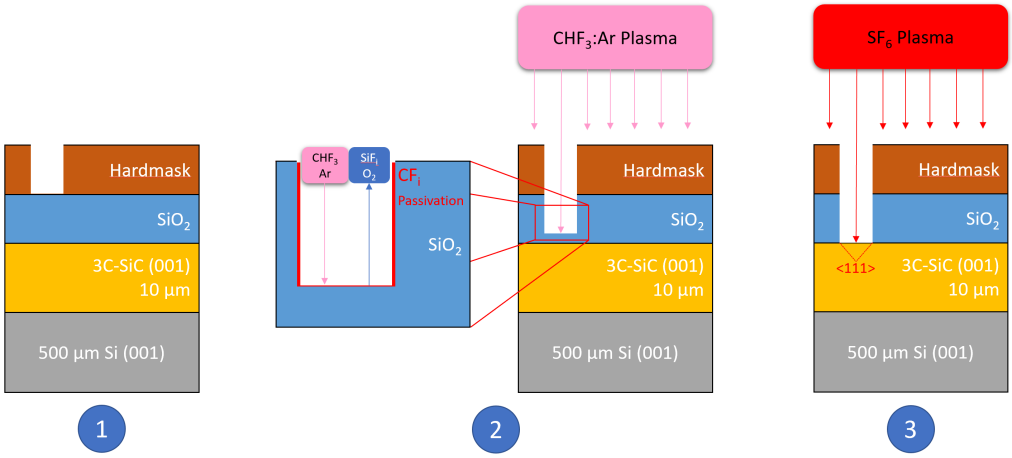

Figure 3.7: Schematic depicting the RIE procedure in 3 steps. 1) Patterning of a hardmask (EBL resist, PS, Ni). 2) RIE of SiO_2 with CHF_3:Ar chemistry. 3) RIE of 3C-SiC with SF_6 chemistry.

The patterning of SiO_2 and 3C-SiC is done by CHF_3/Ar and SF_6 chemistry, respectively. Figure 3.7 depicts the employed steps in the process. Once the hard mask is patterned (figure 3.7 (1)), the samples are introduced into an Oxford plasmalab 100. Figure 3.7 (2) depicts the RIE of SiO_2. The plasma was operated 25 W and 30 mTorr and fed with 20 SCCM of CHF_3 and Ar respectively. The etching rate was about 7 nm/h. Total etching time was experimentally estimated for each batch and structure. For example, etching BCP structured samples usually exhibited much lower etching rates of the SiO_2 mask. This is probably caused by diffusion limitation of products and educts due to the small lateral feature sizes. Tests with various mixtures of CHF_3 and Ar showed that the equal mix results in a very anisotropic etch profile with very steep sidewalls. When etching is conducted CF_i polymers deposit on all SiO_2 surfaces. Ar removes such polymers selectively from the bottom of the etched hole and therefore preserves vertical etching rate while lateral etching is suppressed. (see section 2.5). If no etching of 3C-SiC is required, the resist can be removed and after another cleaning step, with isopropyl alcohol, acetone and DI Water, the samples can be introduced into the UHV chamber of our PAMBE.
Once transferred into SiO_2, the patterns can be etched into 3C-SiC with an additional SF_6 step. This was also done in an Oxford plasmalab 100. The plasma was operated at 100 W, 95 mTorr and supplied with 100 SCCM of SF_6. Without any supplement like Ar or O, the etching results in V-shaped grooves approximately dissecting <111> facets along [110]. However, this also attacks the SiO_2 mask, as the resist is not strong enough to withstand SF_6 RIE.

3.7 PAMBE of cubic Gallium Nitride

To grow cubic Gallium Nitride (c-GaN), Plasma Assisted Molecular Beam Epitaxy (PAMBE) was employed. Growth was carried out in a Riber32 MBE chamber with Knudsen effusion cells. A schematic of the UHV chamber is depicted in fig. 3.8. Gallium, Aluminium, Indium, Silicon, Germanium, CBr_4 and Nitrogen can be utilized. Metals were evaporated from Boron Nitride crucibles designed for a maximum temperature of 1200°C. Nitrogen was activated by an Oxford HD25 plasma source, operated at 260 W and fed with 0,5 SCCM of N_2. Substrate holder can pick up sampleholders with up to 3" diameters and rotate during growth. Employed sampleholders were made of Molybdenum and manufactured to hold 1x1 cm^2 and 2x2 cm^2 samples. For cooling liquid N_2 was injected into a cryoshroud. Base pressure of the cooled UHV chamber was $4{\cdot}10^{-9}$ mbar.

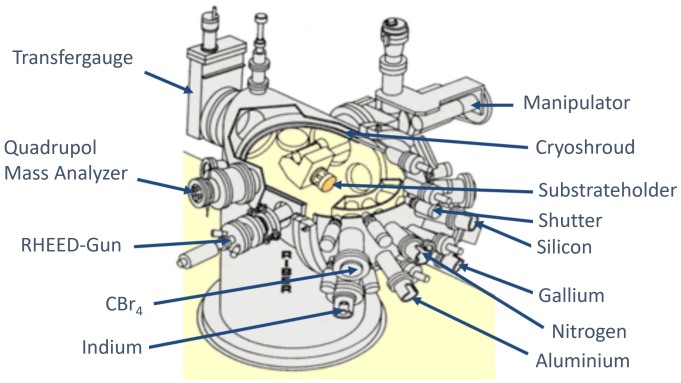

Figure 3.8: Schematic of the Riber32 MBE. Adopted from [Kem14].

Besides pressure gauges the chamber is also equipped with a quadrupol mass spectrometer (QMS) to measure background gas composition. In our case thats mostly Nitrogen and some traces of water with relative pressures well below 10^{-12} mbar. Before transfer, the pressure in the transferchamber is reduced to about 10^{-8} mbar before transfervalve is opened.

Growth of c-GaN is conducted in metal rich conditions as described by As and Schikora et al. [As03; As10; Sch02]. In this thesis, c-GaN is grown on 3C-SiC/Si (001) pseudo-substrates. Growth is controlled by means of RHEED (see section 2.3.1). At regular growth conditions, a monolayer of Ga is maintained on the surface during growth. The control of Ga coverage during growth is crucial to obtain state of the art c-GaN thin films. Surface morphology, structural quality, growth rate and more features are strongly coupled to Ga coverage.

The amount of Ga on the surface, for fixed Ga and N fluxes, is controlled by substrate temperature. If too much Ga is present, the substrate is heated to increase evaporation and vice versa. Before growth the substrate temperature is set with so called "Ga flashes" on the clean 3C-SiC (001) surface. RHEED allows to measure ad- and desorption times of Ga and the ratio is calculated as a first approximation of the sticking coefficient. The substrate is cleaned and brought to a reproducible state by flashing with Ga and Al. The Ga cell is operated at 923°C resulting in a flux of $2{\cdot}10^{14}\,\frac{\text{atoms}}{\text{cm}^2\text{s}}$ used for flashing and growing.

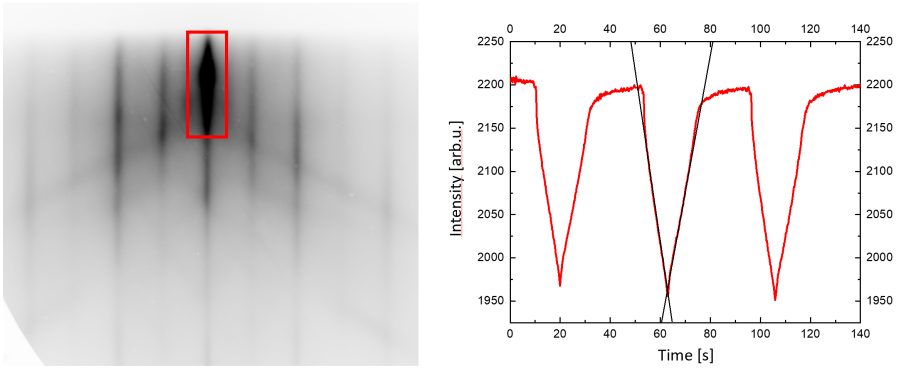

Figure 3.9: (left) RHEED image of the cleaned and flashed 3C-SiC surface along [110]. (right) integral intensity of the specular spot (red box) plotted vs time showing 3 Ga flashes at 753°C. Sticking coefficient was estimated to be 0.56.

The Al cell was operated at 1005°C for flashing. To flash the substrate, it is heated to 750°C. Afterwards Ga shutter is opened for 10s and closed for 30s. This is done 10 times to ad- and desorb Ga from the substrate. Subsequently, the substrate is heated to 900°C. The procedure is then repeated with Al. Flashing with metals removes contaminants like oxygen compounds. If prepared in this way, 3C-SiC exhibits a very streaky RHEED pattern with 2x2 reconstruction (see fig. 3.9). Before growth the sample is then cooled back down to about 750°C. 3 Ga flashes are done again and the integral intensity of the specular spot is measured with respect to the time. While adsorbing Ga, the reflected intensity decreases as the surface gets rougher due to the adsorbed Ga atoms. After the shutter is closed, Ga is evaporating and the surface gets smoother again, thus integral intensity increases. Calculating the ratio

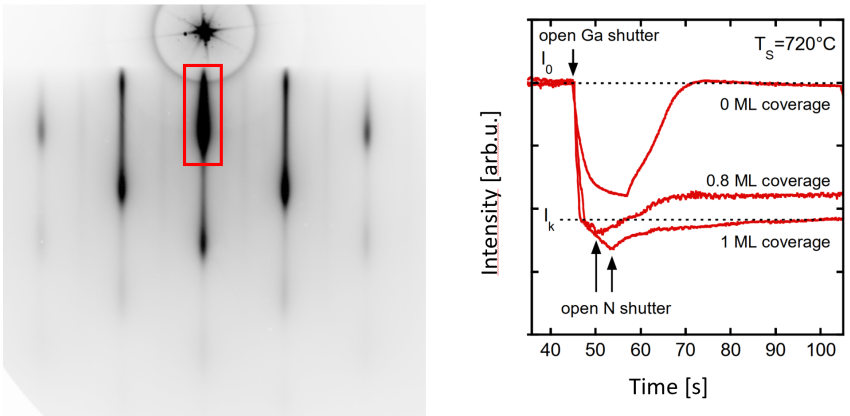

Figure 3.10: (left) RHEED image of thin and dominantly 2D c-GaN along [110]. (right) integral intensity of the specular spot (red box) plotted vs time. Adopted from [As10].

of intensity changes for both processes, given by the slope of linear fits, yields the sticking coefficient in a first approximation. Before growth we aim for a sticking coefficient of 0.55 for Ga/3C-SiC (001) to ensure metal rich growth conditions. This situation is depicted in figure 3.9. The substrate temperature is then varieed within 10-15°C to achieve the nominal sticking coefficient. This can vary from sample to sample as the total volume differs and thermal contact is not exactly the same each time growth is conducted. Between real substrate temperature and thermo couple we observe an offset in the order of 10K as also reported by Deppe [Dep20]. In this thesis, all reported temperatures are thermocouple readings. The flashes in figure 3.9 exhibit a sticking coefficient of 0,56 for a set substrate temperature of 753°C.
With this procedure regular growth conditions are set. The next step is to nucleate GaN. This is done in cycles to achieve good relaxation without facetation. Each cycle is started with about 7 s of Ga deposition which is roughly one monolayer of Ga. After 7 s the Nitrogen shutter is also opened. Both shutters remain open for 30 s. Afterwards both shutters are closed for 30 s to give GaN time to nucleate properly. 10 Cycles are conducted for nucleation. This results in 5 minutes of total growth time and in a streaky 2D surface.
Figure 3.10 shows such a RHEED pattern after nucleation process with a total growth time of 5 minutes. Once the surface is smooth and the RHEED pattern shows pure streaks, the substrate temperature is precisely set again. The Gallium shutter is opened for about 7s. After a short adsorption time a characteristic kink I_k appears, marking the point of a monolayer coverage with gallium. When the N shutter is opened intensity has to climb back to the intensity I_k. If the substrate is too hot, too much Ga evaporates and less then a monolayer is present. If substrate is too cold, not enough Ga is evaporating and droplets can form because the coverage exceeds a monolayer.
Once a steady state is reached, rotation is turned on and growth time is measured with a stopwatch. Growth is interrupted about every 30 minutes to check Ga coverage again. Growth rate is around 150 nm/h. After the nominal thickness is reached, growth is interrupted by closing all shutters and shutting down the plasma source as fast as possible to suppress residual reactions on the surface with activated nitrogen.
As grown state of the art c-GaN thin films with 600 nm thickness show surface roughnesses in the order of 4 nm and (002) rocking curve FWHM of about 20 arcmin. Hexagonal phase content is well below 1%. The remaining signal from hexagonal phase can be assigned to originate from SF's.

CHAPTER 4

Results

Selective Area growth is necessary as a basis for different sophisticated growth techniques and will be explained with respect to possible applications. The physical principles were explained in chapter 2.2.2. Possible applications are motivated, followed by estimation of a critical parameter for nucleation of GaN on SiO_2. After probing critical substrate temperature, the parameters were adopted to nanoscopic masks on 3C-SiC. Once that process worked repeatable, it was tested on various nanoscopic patterns, written with different lithography methods explained earlier. Each chapter will contain the morphological and structural properties of the mask and the deposited GaN, dominantly measured by Atomic Force Microscopy (AFM), Scanning Electron Microscopy (SEM), Transmission Electron Microscopy (TEM) and High Resolution X-Ray Diffraction (HRXRD). The chapter is concluded with growth of c-GaN on unstructured substrate at elevated substrate temperatures, employed for Nano Selective Area Growth (NSAG) of GaN.

4.1 Selective Area Growth

Selective Area Growth (SAG), as explained in chapter 2.2.2, describes surface sensitive nucleation and growth. Within this thesis all experiments were carried out employing SiO_2 as a growth mask. SAG was as already reported in literature for hexagonal nitrides [Fan08; Kap97; Sch11; Tan00]. Also different masks were reported to be useful, like Si [Got11], SiN_i [Ber10] and Ti [Hir08]. Furthermore, more techniques like Epitaxial Lateral Overgrowth (ELO) [Ju04], Pendeoepitaxie (PE) [Lin99], Nano Hetero Epitaxy (NHE) [Che08], Aspect Ratio Trapping (ART) [Man20], Phase Transitions [Liu16] and more get viable with proper SAG.
To estimate the parameters leading to proper SAG, a series on patterned silicon was conducted first. Silicon is very cheap compared to 3C-SiC, also very clean and easy to coat with oxides. From this series we get a rough idea of the substrate temperatures necessary to suppress GaN nucleation on SiO_2. This critical substrate temperature was estimated for the Ga flux nominally used for regular growth of c-GaN thin films. After estimation of the critical substrate temperature for a fixed Ga flux the parameters for SAG were adopted to a macroscopic pattern first. Subsequently, NSAG is demonstrated on NSL Masks with opening diameters of 130 nm, BCP masks with opening diameters of 20 nm and V-shaped Grooves with 100 nm width. NSL was used to test parameters for NSAG on 3C-SiC/SiO_2 (001). V-shaped grooves were employed to show NSAG on <111> facets of 3C-SiC. BCP masks were used to see if coalescence after NSAG is possible.

4.1.1 Critical substrate temperature

Starting from regular growth conditions, with a substrate temperature of about 750°C and Ga cell operated at 923°C (BEP $2{\cdot}10^{-7}$mbar), a substrate temperature is to be found where no GaN nucleates on SiO_2 covered surfaces. This temperature will be called critical substrate temperature T_c. By increasing substrate temperature the mean residence time of adatoms can be decreased below a certain threshold, where nucleation is unlikely (see section 2.2.2). Therefore, the Ga flux was fixed to test if there is such a temperature. Below critical substrate temperature GaN nucleates on all surfaces. Above critical substrate temperature GaN does not nucleate on SiO_2 if fluxes, substrate temperature and total growth time is fixed.

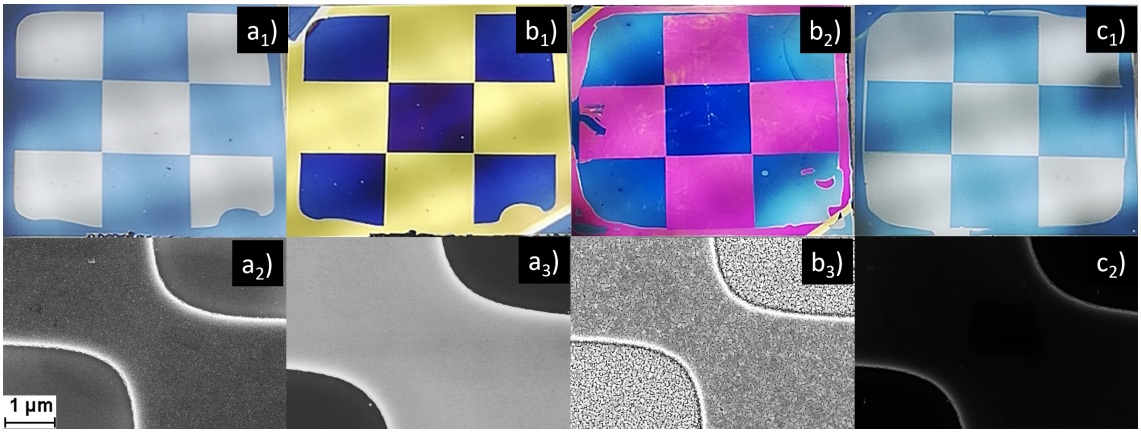

Figure 4.1: Optical photographs (top row) and SEM images (bottom row) of prepared and overgrown checkerboard patterns. SEM images were taken from the corners of the inner checker board field. $a_{1,2,3}$) Samples before growth. $b_{1,2,3}$) Samples overgrown at 810°C. $c_{1,2}$) Samples overgrown at 870°C. Samples shown in $a_{1,2}$), b_1) employed P-SiO_2 masks. Samples shown in a_3), $b_{2,3}$) and $c_{1,2}$) used T-SiO_2 masks.

Figure 4.1 depicts a selection of optical photographs and SEM images of Si/SiO_2 samples, patterned with checker board like structure as described in section 3.2. SEM images were taken from the corners of the inner checker board field. The pictures denoted with $a_{1,2,3}$) show as prepared samples before overgrowth. In a_2) and a_3) the different oxides masks can be seen with P-SiO_2 in the right and T-SiO_2 in the left image. The plasma deposited mask looks grainy and was also found to be rougher compared to the thermal mask by means of AFM. On a 1x1 µm^2 scale, P-SiO_2 exhibited a roughness of 4 nm while the roughness of T-SiO_2 was well below 1 nm. The difference was even bigger for the prepared Si surfaces as the plasma processes also roughen the Si by some extend. Pictures $b_{1,2}$) in figure 4.1 depict samples after overgrowth at 810°C employing different oxides. The nice golden, purple and blue colors originate from thin film interference. Due to the difference in mask roughness, GaN has a different probability to nucleate where a

rougher surface propably favors nucleation by increasing Ga residence time. Delayed nucleation results in a thinner film and therefore different colors. The color change was observed because GaN nucleates on all surfaces. Thus growth happened below T_c. The picture b_3) shows a SEM image of the sample overgrown at 810°C masked with T-SiO_2. GaN grains with about 100 nm in size grew on all surfaces but they appear to be a little smaller on the Si surfaces.
Pictures $c_{1,2}$) show a sample masked with T-SiO_2 overgrown at 870°C. From the photo one can barely see any change compared to the as prepared sampled depicted in a_1) Just a little edge caused by shadowing of the sample holder is depicted in the top left corner. The SEM image appears darker compared to the others, because SiO_2 and GaN appear in different brightness. If brightness and contrast are optimized for GaN as in b_3) Si and SiO_2 appear pitch black. As no bright spots can be seen, there is no nucleation of GaN at 870°C on SiO_2. Over both oxide series different color trends emerged but coverage vanished for 870°C. As the samples overgrown at 855°C still show coverage, the transition is very sharp and temperature sensitive. From optical examination a T_c of about 870°C was estimated.

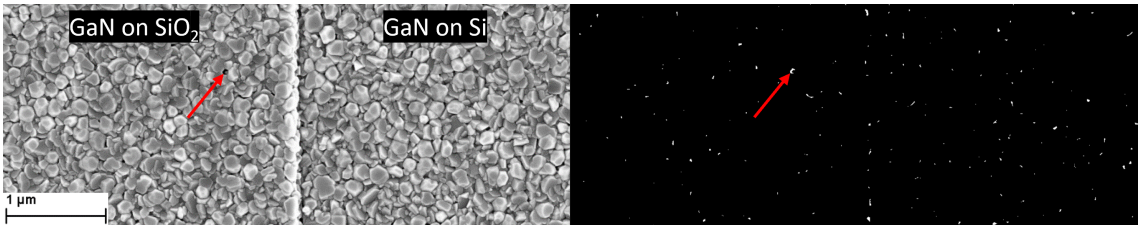

Figure 4.2: SEM image of the edge from the center checker board field of a sample overgrown at 750°C. GaN nucleated on all surfaces with some little gaps (red arrow). By reducing the image to a binary color scale by using a certain threshold, gaps get visible. From a binary color scale areal statistics can yield the coverage in %.

To further verify, SEM images of every sample were taken from edges of the middle checkerboard field. By optimizing brightness and contrast for either GaN or SiO_2 both were separated very well as discussed earlier (compare fig. 4.1 a_2) and c_2)).
Figure 4.2 depicts a SEM image with brightness and contrast optimized for GaN. Gaps in the very grainy layer appear pitch black. The complete grey scale of the image contains 255 steps. By moving the color threshold this scale is reduced to 2 values, white and black. After inversion of the color scale, gaps appear as white spots. Such an image allows for statistic areal evaluation of the covered area by just calculating the ratio of black and white pixels. This was done for SiO_2 and Si regions, separately. The coverage is then given by:

$$Coverage = \frac{BlackPixels}{BlackPixels + WhitePixels} \tag{4.1}$$

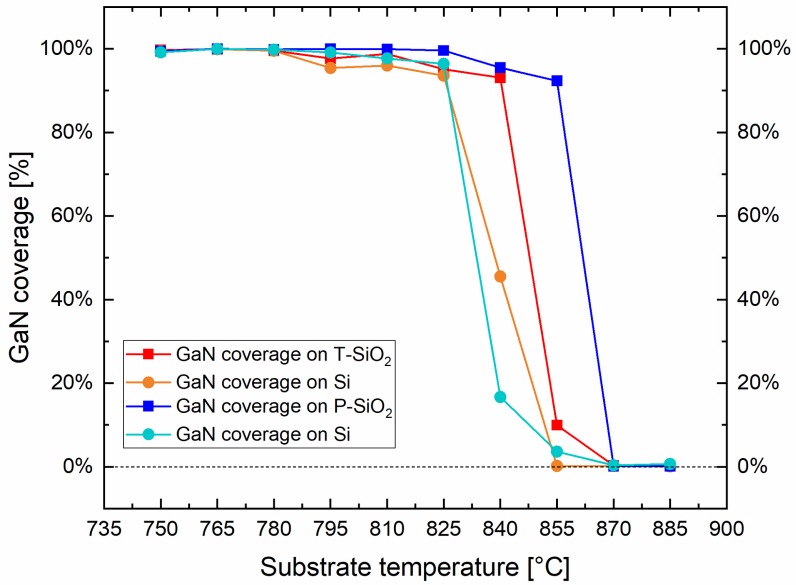

Figure 4.3: GaN coverage on different exposed surfaces overgrown at different substrate temperatures. Critical substrate temperature of T_c=870°C results in neglectable coverage.

Applying formula to the image shown in figure 4.2 yields a coverage of 99.83%. This analysis was done for all overgrown samples.
Figure 4.3 shows the results for evaluation of GaN coverage vs. substrate temperature. The red and blue lines show coverage on T-SiO_2 and P-SiO_2, respectively. The other curves graph coverage on the Si surfaces after deposition and RIE of thermal oxides (orange) or of plasma deposited oxides (teal).
The first important result is the critical substrate temperature of 870°C where GaN coverage is well below 1% for all surfaces. This result was also published [Mei21]. For adoption to 3C-SiC, a substrate temperature of above 870°C will serve as a starting point.
Another important thing to notice is, that coverage on T-SiO_2 is always below P-SiO_2 which is attributed to the different surface roughnesses of both oxides. This could make thermal oxides preferable, compared to plasma deposited oxides. Finally, all samples show that coverage vanishes first on Si, while transition on coverage looks to be more abrupt on the teal curve. This implies, that Si could be an interesting alternative mask material as well.

4.1.2 SAG on nanoscopic SiO_2 Masks

The investigation of the critical substrate temperature T_c of SiO_2 for a Ga cell operated at 923°C (BEP $2{\cdot}10^{-7}$mbar) revealed, that T_c=870°C is sufficient to prevent nucleation during 41 minutes of continuous growth. Nitrogen plasma was fed with 0.5 SCCM of N_2 and operated at 260 W. Selective Area Growth (SAG) of GaN was done by overgrowth of the same checkerboard patterns, but this time 3C-SiC (001) was employed. For a given set of parameters, the sticking coefficient for Ga is different on 3C-SiC, Si and SiO_2.

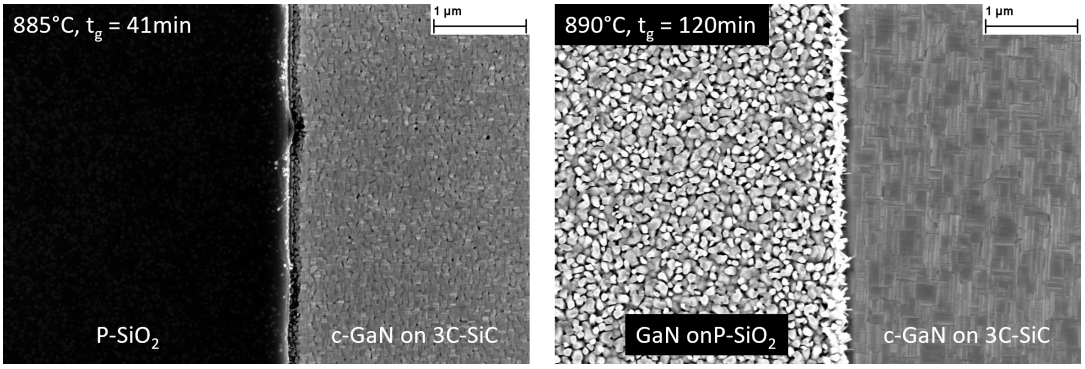

Figure 4.4: SEM images of patterned 3C-SiC (001) overgrown by GaN for 41 min at 885°C growth temperature (left) and for 2 h at 890°C growth temperature (right). Prior to growth, the left side was bare P-SiO2, and the right side was bare 3C-SiC. Polycrystalline and mostly hexagonal GaN nucleated on the SiO2 side at both samples. Faceted cubic GaN is observable on the 3C-SiC side. 90° angles between facets indicate cubic structure.

The challenge is to balance III/V flux ratio, substrate temperature and growth time precisely to make nucleation on the mask unlikely but not totally suppress nucleation on the substrate. The first experiments were done with variation in substrate temperature and growth time. Figure 4.4 shows SEM images of two samples with P-SiO_2 masks overgrown at comparable substrate temperatures and different growth times. It underlines the impact of growth time on selectivity. To achieve an epilayer thickness exceeding the 200 nm a growth time of 2 h was chosen. Assuming a growth rate of 150 nm/h, typical at nominal growth conditions, this would result in 300 nm of GaN. At 41 min only partial coalescence of small grains is visible. After 120 min a coalesced film with cubic facetation can be observed. Extending the growth times leads to properly coalesced epilayers but also increases parasitic nucleation and growth. Nevertheless, critical substrate temperature is about 15°C higher on 3C-SiC substrates for 41 min of growth compared to earlier experiments on Si. This is probably because the 3C-SiC/Si substrates are about 100 μm thicker then the bare Si substrates. As the whole process is modeled by nucleation rates, increasing growth time also increases the probability of nucleation

on the mask. If nucleation happens on the mask, the growth speed is comparable for growth on 3C-SiC and SiO_2 as GaN grows on GaN once nucleated.

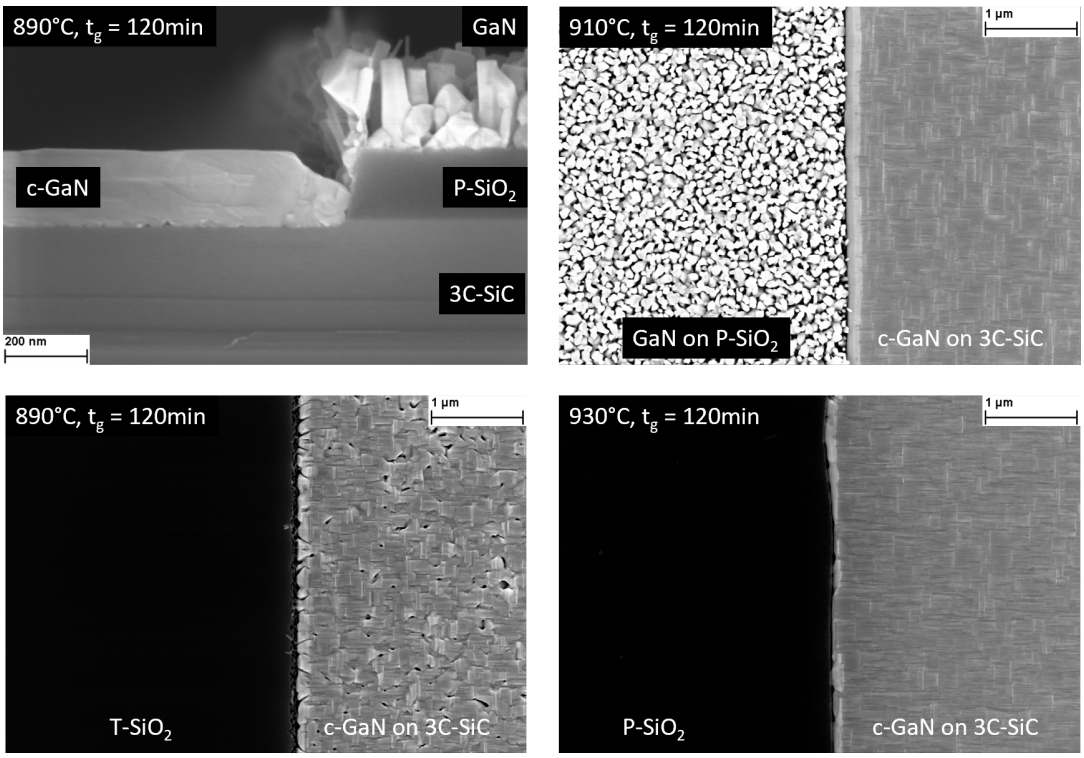

Figure 4.5: (top-left) SEM side-view image of the sample depicted in figure 4.4 right. Sample was overgrown for 120 minutes at 890°C. (top-right,bottom) Top-view of samples grown at different temperatures at a fixed Ga flux for 120 minutes.

After testing the longer growth time, substrate temperature was increased further to restore selectivity. Figure 4.5 shows SEM images of 4 samples with different substrate temperatures and oxide masks overgrown for 2 h. Top left image depicts the same sample shown in figure 4.4 right. After 2 h only 200 nm were deposited. From the side-view one can see that coverage consists of randomly orientated and mostly hexagonal grains on SiO_2. On 3C-SiC a plain film was grown. The top images indicate a strong temperature difference between T- and P-SiO_2 masks. Where 890°C were sufficient to supress growth on T-SiO_2, P-SiO_2 showed poly crystalline h-GaN coverage op to 910°C.
Increasing the substrate temperature restored selectivity for both masks employed. Figure 4.5 also depicts top-down SEM images of 3 overgrown samples. Selectivity was achieved for growth on T-SiO_2 patterns at 890°C (bottom left). For P-SiO_2 even 910°C was insufficient and good selectivity was only achieved for temperatures of 930°C and above (top and bottom right). This examples show that it was possible

to adopt the parameters from the series on Si and grow GaN selectively at high temperatures using different oxides as masks. From SEM images the selectively grown GaN films look cubic due to surface facets with 90° angles. Most samples show coalesced layers but their surface morphology varies as well as their growth rates. While GaN grows flat and mostly coalesced on top of 3C-SiC, a polycrystalline hexagonal arrangement of grains deposited on SiO_2.

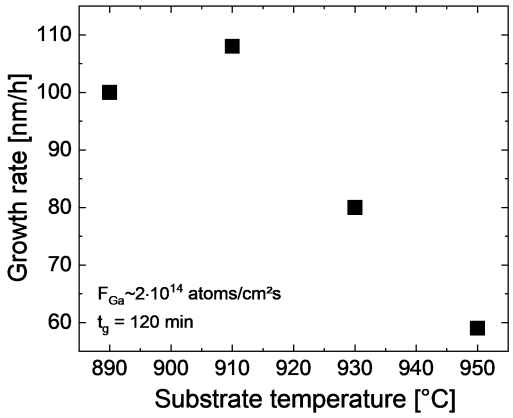

Figure 4.6: GaN coverage on different exposed surfaces overgrown at different substrate temperatures. Critical substrate temperature of T_c=890°C results in neglectable coverage on SiO_2.

Figure 4.6 shows the growth rates from the GaN grown on 3C-SiC. Overgrowth at such high temperature significantly reduces the growth rate. Starting from around 100 nm/h at 890°C it decreases to only 60 nm/h at 950°C as GaN dissociation increases with rising temperatures. At regular growth conditions a growth rate of about 150 nm/h is typical. For further analysis, the sample overgrown selectively at 930°C is measured by means of HRXRD, AFM and PL.

AFM from the center field of the checkerboard pattern showed a roughness of 3.7 nm and is comparable to growth at lower temperatures. AFM images are not depicted here as surface morphology can already be seen in figure 4.4 and 4.5.

Figure 4.7 shows the results for PL and HRXRD measurements. The PL spectra were obtained using a 266 nm Nd:YAG Laser operating at 5 mW. The samples were cooled with a closed helium cycle to 13 K. The blue spectrum was taken from c-GaN selectively grown on 3C-SiC at 930°C (fig. 4.5 bottom right). The blue spectrum originates from GaN grown on SiO_2 at 910°C (fig. 4.5 top right). The laser spot was below 1 mm in diameter, allowing selective measurements.

Observed transitions were marked with dashed lines. Transitions from cubic (blue) or hexagonal (yellow) phase are highlighted.

The black spectrum shows dominant hexagonal transitions with cubic impurities. This confirms poly-crystalline and mostly hexagonal phase of GaN grown on SiO_2, as already observed by SEM, again. The transitions at 3.35 eV (I_2-BSF) and 3.42 eV (I_1-BSF) can be attributed to Basal Stacking Faults (BSF) [Mei06]. The transition at 3.47 eV (D^0,X) corresponds to the excitonic transition of hexagonal Gallium Nitride [Tak09].

The blue spectrum shows intense transitions typical for c-GaN. The transition at 3.07 eV is described as a convolution of two transitions, a donot-acceptor recombination $(D^0,A^0)_C$ and a C-related band-acceptor recombination $(e,A^0)_C$, separated

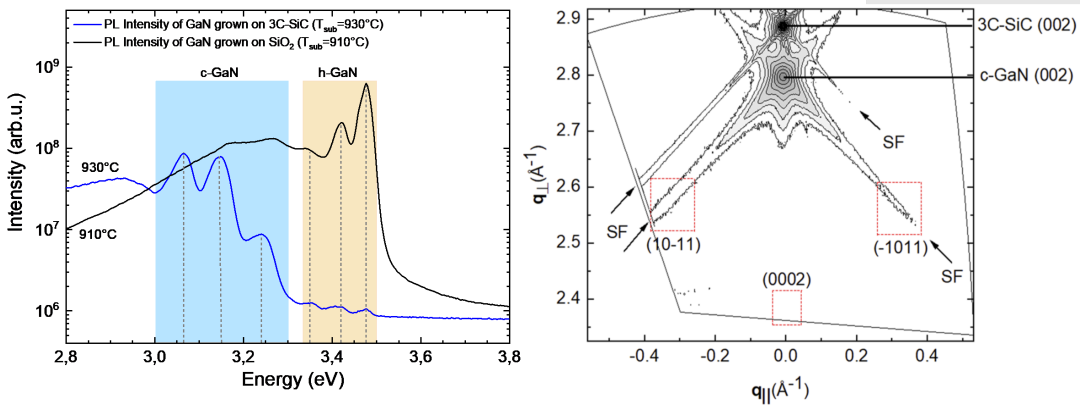

Figure 4.7: (left) PL spectra of two samples overgrown with GaN. Both were excited by a 266 nm Nd:YAG laser operating at 5 mW at a sample temperature of 13K. The blue spectrum was measured on the GaN surface grown on bare 3C-SiC selectively at 930°C (fig 4.5 bottom right). The black spectrum originates from GaN grown on the SiO_2 mask of a sample that was not selectively overgrown at 910°C (figure 4.5 top right). (right) RSM of the sample overgrown selectively at 930°C showing symmetrical (002) reflections of 3C-SiC and c-GaN. Red boxes indicate where one would expect reflections from hexagonal inclusions [Fre17]. Comparing intensities along both [110] and [-110] azimuths yields a hexagonal content of below 1%. Published in [Mei21].

by 25 meV [Sch02]. It was addressed to be caused by carbon doping. However, the sample was not doped intentionally. The other transitions at 3.15 eV (D^0,A^0) and 3.24 eV (D^0,X) belong to a donator-acceptor pair and an excitonic transition [As03; Fen12; Sch02], respectively. Hexagonal luminescence is also observable but just above noise level.

Figure 4.7 also shows a Reciprocal Space Map (RSM) along the (002) reflections of 3C-SiC and c-GaN of the sample selectively overgrown at 930°C. Red boxes indicate where one would expect reflections of hexagonal inclusions from <111> facets and h-GaN/3C-SiC grown in [0002/001] direction [Fre17]. Taking those low intensities from stacking faults into account along both azimuths yields a hexagonal content of well below 1%. Calculation is described in section 2.3.2.

With PL and HRXRD measurements there is clear proof that it is not only possible to grow Gallium Nitride selectively but also with dominant cubic phase on 3C-SiC (001) masked with SiO_2. From here a large number of well known techniques for hexagonal Gallium Nitride may become viable for the cubic counterpart. Proper SAG enables Epitaxial Lateral Overgrowth (ELO) [Ju04], Pendeoepitaxie (PE) [Lin99], Nano Hetero Epitaxy (NHE) [Che08], Aspect Ratio Trapping (ART) [Man20], Phase Transitions [Liu16] and many more. This results were also published after a peer review process in AIP Advances [Mei21]. Furthermore, it proves the model just proposed by Gridchin et al. qualitatively [Gri22]. Selective growth was established for a fixed III/V flux ratio by increasing the substrate temperature.

4.1.3 GaN growth on NSL patterned SiO_2 on 3C-SiC

Reactive Ion Etching (RIE) was done by CHF_3/Ar chemistry as explained in chapter 2.5. In order to achieve rectangular holes in a SiO_2 matrix, RIE parameters for pattern transfer were optimized.

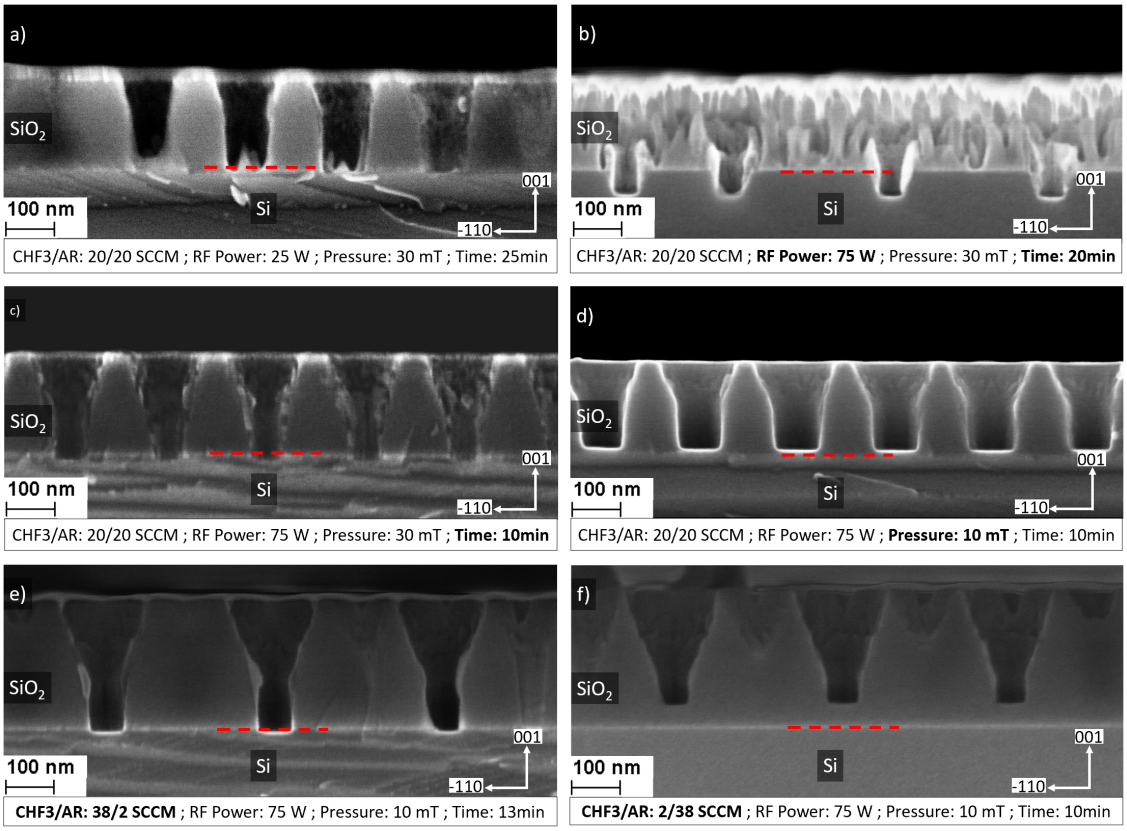

Figure 4.8: SEM side-view of cleaved samples etched under varied RIE conditions. Parameter changed is printed bold. Dashed orange line indicates SiO_2/Si interface.

Figure 4.8 depicts six SEM side-view images of cleaved samples, etched under various parameter changes. The changed parameter from sample to sample is printed bold in the corresponding image. To begin a recipe, used earlier within our working group, was tested. The process was operated at a RF power of 25 W, a pressure of 30 mTorr and fluxes of 20 SCCM of CHF_3 and Ar, each. After 25 minutes of etching the holes were etched to the bottom of the hole, reaching the SiO_2/Si interface, with slightly sloped sidewalls. However, residual SiO_2 grass was observed (figure 4.8 a)). Dashed orange line indicates SiO_2/Si interface.
To counteract SiO_2 residuals the RF power was increased to 75 W and the time was reduced to 20 minutes (figure 4.8 b)) in anticipation of a much higher etching rate. Nevertheless, the Nickel mask was not able to withstand the etch and the SiO_2 mask

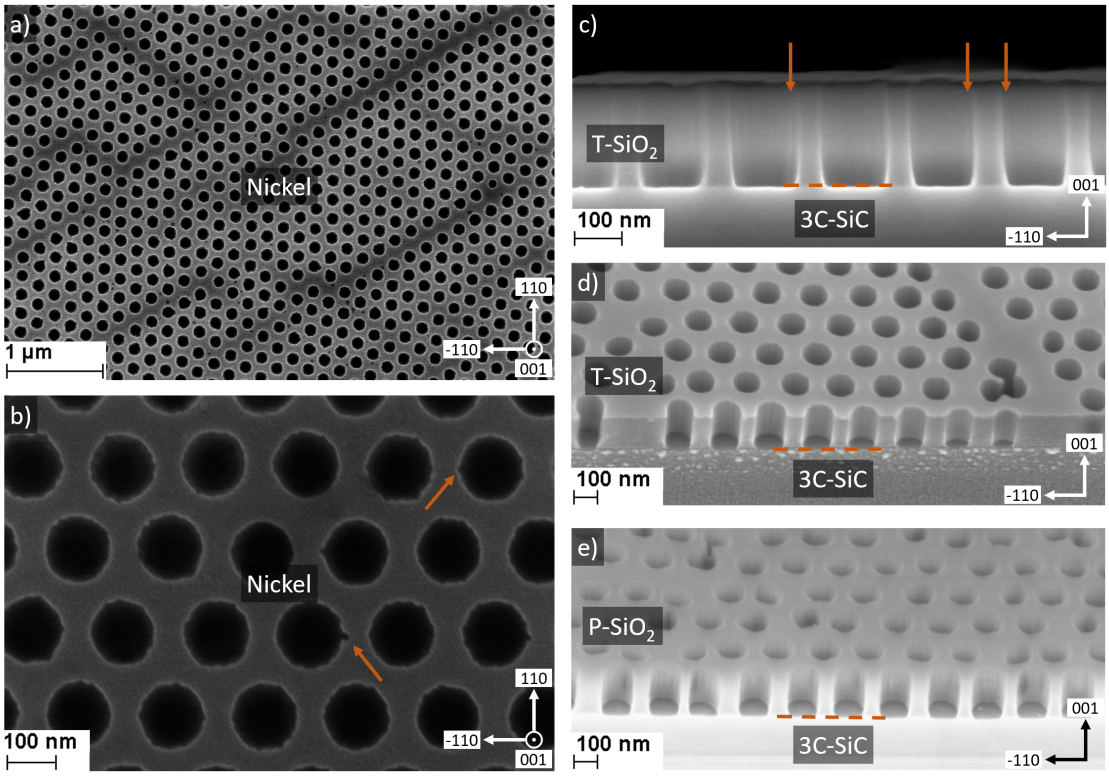

Figure 4.9: SEM images of the final SiO_2 masks patterned with NSL. a), b) top-down views of the Nickel mask. c) side-view of the mask. d) and e) depict 45° angled views of the cleaved mask. orange arrows indicate mask imperfections transferred to the holes appearing as grooves in the sidewalls. Dashed orange line indicates SiO_2/3C-SiC interface.

was damaged beyond recognition. Moreover this was accompanied by over etching into the Si substrate by about 50 nm.
Etching time was reduced to 10 minutes to successfully preserve the Nickel mask (figure 4.8 c)). However, the holes were not rectangular but in bottle neck shape. Also a little over etch into the Si substrate is left.
At this point the etch was to aggressive and the pressure was reduced to the lowest possible amount of 10 mTorr necessary to achieve a stable plasma (figure 4.8 d)). The resulting holes had much larger bases but the bottle neck shape persisted. No over etching was observed.
Variation of flux ratios did not solve the problem as depicted in figure 4.8 e) and f). After all, the problem of bottle neck shape was solved by switching to a slightly different apparatus with the same name (Oxford Plasmalab 100) operated by another working group. The chamber is probably a little bigger resulting in a more perpendicular ion bombardment of the surface. It also has way less users and is probably cleaner. The other device was tested because chamber geometry and contamination

level strongly impacts etching anisotropy.
In the other apparatus, the plasma was operated as described in section 3.6. Figure 4.9 depicts different SEM images of the final SiO_2 masks patterned with NSL. a) and b) show top-down views of the Nickel mask and c) a side-view of the holes. d) and e) depict 45° angled views of the cleaved mask.
Orange arrows indicate imperfections from polystyrene spheres transferred into the Nickel mask. As the etch is very anisotropic they appear as grooves in the sidewalls of the holes. Besides that, the sidewalls are very steep and only a slight bow can be observed.
The achieved structures, are then employed for nano selective growth of GaN on 3C-SiC.

4.1.4 GaN growth on NSL patterned SiO_2 on 3C-SiC (001)

Nano Selective Area Growth (NSAG) was tested on NSL mask patterned SiO_2/3C-SiC with the parameters from the previous section. Samples were overgrown for 3h with adjusted Ga fluxes.

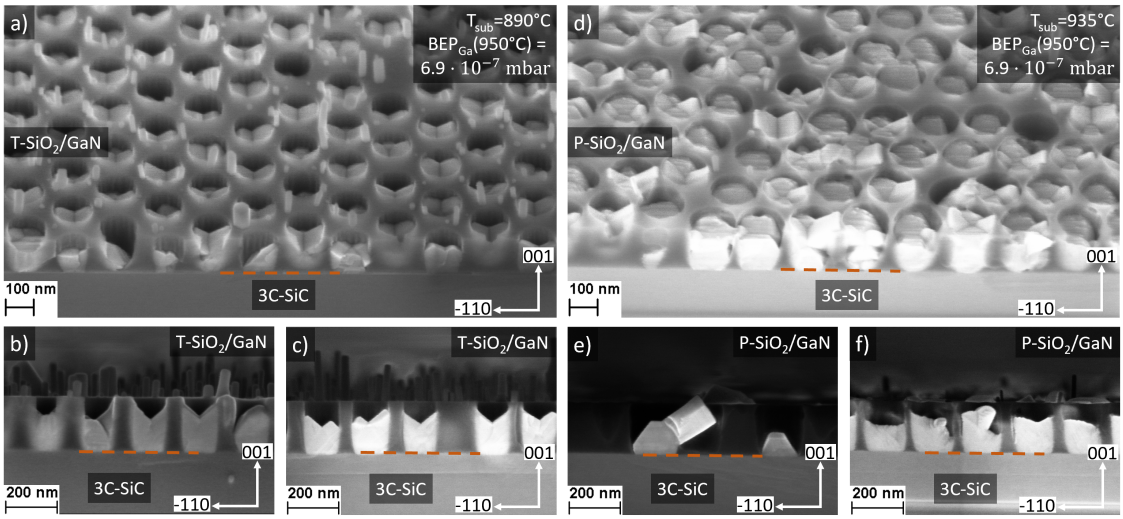

Figure 4.10: SEM images of two overgrown and cleaved samples with NSL patterned oxide masks grown at different substrate temperatures of 890°C (a) and 935°C (d), respectively. Both were overgrown selectively for 3h. a), d) 45° angled-view and b), c), e), f) side-view

Figure 4.10 shows SEM images of two samples overgrown at 890°C (a,b,c) and 935°C (d,e,f) with a constant Ga-flux (BEP $6.9{\cdot}10^{-7}$mbar). The images a), b), and c) depict results on a thermal oxide (T-SiO_2) mask while images d), e), and f) show results on a plasma deposited oxide (P-SiO_2) mask. As shown previously, for the P-SiO_2 a higher temperature is necessary for selective growth.
For both oxides selective overgrowth was achieved on 130 nm openings, but an increased Ga flux was necessary to get proper nucleation in the holes. On the thermal mask a characteristic V-shape of the GaN filling can be observed (see fig. 4.10 a), b) and c)). This is a consequence of sample rotation and its occurrence is much less probable without rotation, as visible in figure 4.10 d). The P-SiO_2 covered sample was not rotated during growth and shows less V-shaped grains within the holes. However, if a V-shape occurs it is probably caused by cubic to hexagonal phase transitions on <111> facets (see fig 4.10 e)) as described in section 2.1.1. If this happens on opposing <111> facets a hexagonal twin grows out of the hole. Formation of v-shaped grains is further discussed in section 4.1.6.
Besides V-shapes, the grains from hole to hole look very different and growth is somewhat inhomogeneous. Probably nucleation of more then one grain happens per

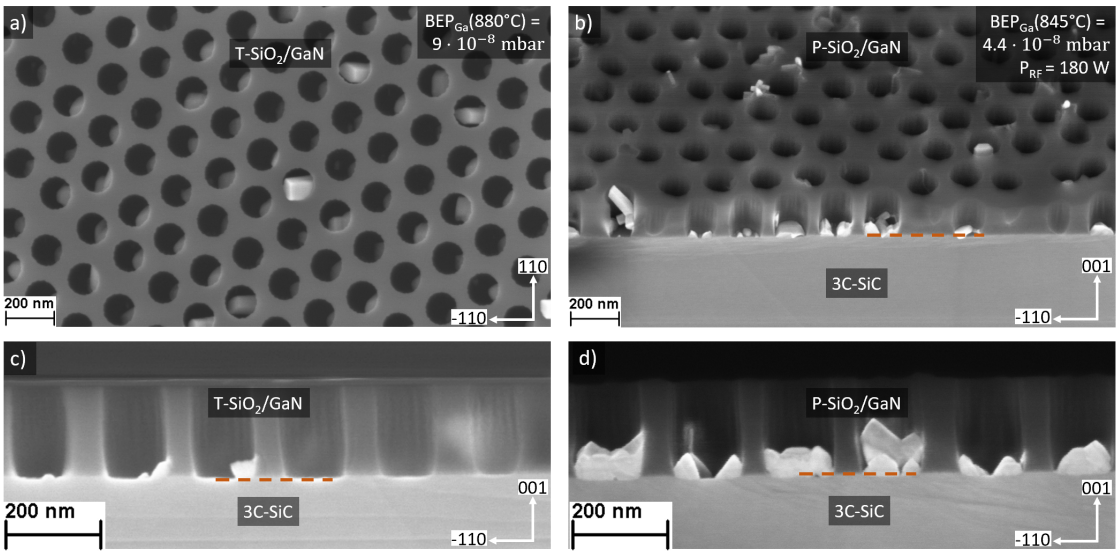

Figure 4.11: SEM images of overgrown and cleaved samples with NSL patterned oxide masks. All were overgrown for 3h and at 870°C. a), d) 45° angled-views and b), c), e), f), g) side-views. a), b) Selectively overgrown T-SiO_2 mask. c), d) selectively overgrown P-SiO_2 mask. e), f), g) Overgrown samples with P-SiO_2 masks and varied Ga fluxes.

hole and once they coalesce different defects can occur leading to different results in every hole. However, for both masks a higher Ga flux was necessary compared to larger mask openings. Nevertheless, NSAG was achieved. While not perfectly selective they represent a good compromise between selectivity and deposited amount. The better the selectivity, the less GaN is deposited. However, this relation seems to hold for all employed substrate temperatures.

Figure 4.11 and 4.12 depict SEM images of thermal and plasma deposited oxide masks patterned by NSL after overgrowth at 870°C. In order to achieve selectivity the III/V flux ratio was varied. The images a), b), c) and d) of Figure 4.11 show the best results in terms of selectivity for T-SiO_2 and P-SiO_2, respectively. The Pictures a), b) and c) of Figure 4.12 depict three samples overgrown with different Ga fluxes at 870°C for 3 h. Experiments on checkerboard patterns (section 4.1.2) pointed out the difference in substrate temperatures necessary to achieve SAG on T-SiO_2 and P-SiO_2 already. For the fixed substrate temperature of 870°C the Ga BEP was reduced to $9{\cdot}10^{-8}$mbar to achieve selectivity on T-SiO_2 masks (see figure 4.11 a)). In contrast, a much lower Ga BEP was uncovered to lead to SAG on P-SiO_2. As visible in figure 4.12 coverage of GaN on P-SiO_2 started to disappear for a BEP as low as $4.4{\cdot}10^{-8}$mbar. However, nucleation on 3C-SiC was accompanied by alot of parasitic nucleation on the shidewalls of the P-SiO_2 holes. To counteract parasitic nucleation, III/V flux ratio was increased again by reducing the RF power of the plasma cell from 260 W to 180 W. According to Gridchin et al. it is the III/V ratio

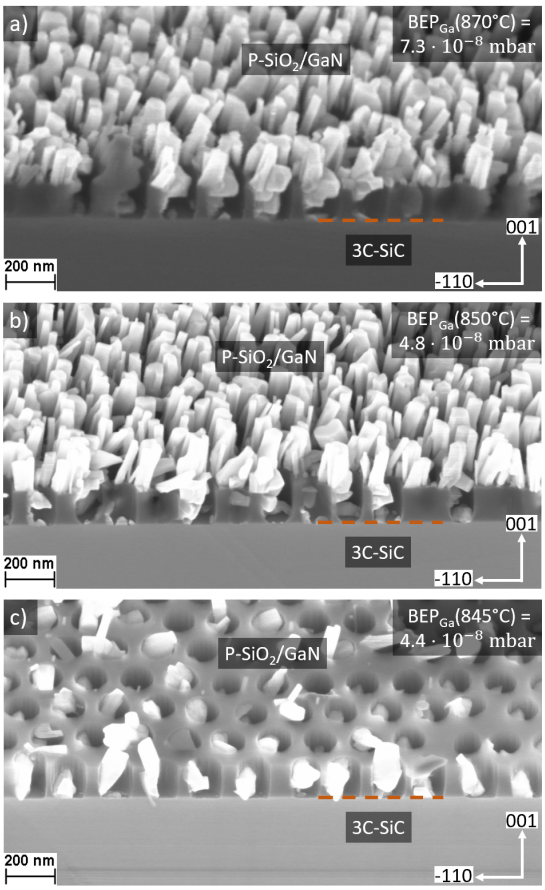

Figure 4.12: SEM images of overgrown and cleaved samples with NSL patterned oxide masks. All were overgrown for 3h and at 870°C. a), d) 45° angled-views and b), c), e), f), g) side-views. a), b) Selectively overgrown T-SiO_2 mask. c), d) selectively overgrown P-SiO_2 mask. e), f), g) Overgrown samples with P-SiO_2 masks and varied Ga fluxes.

that matters and this can also be varied by different amounts of Nitrogen offered. Therefore, SAG on P-SiO_2 requires a reduced Ga flux compared to SAG on T-SiO_2 for a given substrate temperature, but also a reduced N flux. While this observations are in line with the model of Gridchin et al. [Gri22], the effects of Nitrogen adatom behaviour can not be neglected completely.
In summary this shows that SAG can be achieved by variation of the III/V flux ratio.
To confirm cubic phase a sample masked with NSL patterned T-SiO_2 was cleaved and conventionally prepared with x-section mechanical dimple grinding followed by an ion milling step in a GATAN PIPS. The sample was overgrown at 880°C, a Ga BEP of $3.25{\cdot}10^{-7}$ mbar and masked with NSL patterned T-SiO_2.
Figure 4.13 shows two TEM bright field images of the aforementioned sample. It depicts two comparable grains selectively grown in c-GaN not exposing V-shapes. By chance, no such grains were observed after TEM preparation. The left picture is rotated to align [001] upwards.
Some Stacking Faults (SF) can be seen at the c-GaN/3C-SiC (001) interface of the left picture. They are either introduced as a consequence of strain relaxation or by defects from the substrate. Moving upwards some of the SF annihilate, but also new SF's are introduced, intercepting the c-GaN/SiO_2 interface. Those SF's are marked with arrows. Somehow, they don not penetrate the whole c-GaN grain and terminate. The influence of SiO_2 on the GaN grain is not fully understood. On the top part Fast Fourier Transform (FFT) along the red rectangle reveals phase pure c-GaN.

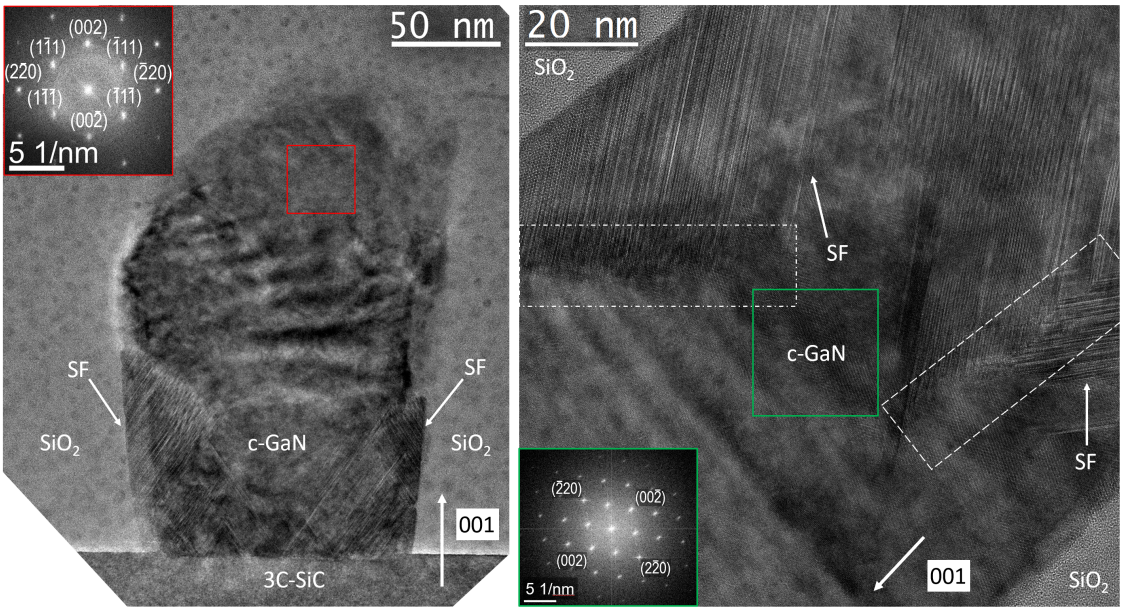

Figure 4.13: TEM bright field images of a sample NSL patterned with a T-SiO_2 mask and overgrown at 880°C with a Ga BEP of $3.25{\cdot}10^{-7}$ for 3 h. (left) a c-GaN grain grown selectively inside a hole in the SiO_2 mask. (right) magnified middle part of a comparable grain. Stacking Faults (SF) are marked with arrows. Dashed and dot-dashed rectangles mark areas of either SF annihilation or SF's just disappearing, respectively. Fast Fourier Transforms (FFT) along the red and green rectangle expose phase pure c-GaN.

The right image depicts another grains middle part with a higher magnification without rotation. Therefore, the [001] direction points to the bottom left. SF's intercept and annihilate in the area marked with a dashed line. On the left part the SF's intercepting the c-GaN/SiO_2 interface again just disappear without any sign of annihilation. Maybe they are a result of strain growing with layer thickness originating from the GaN grain and terminating at the SiO_2 interface. Again, FFT beyond defective region (green rectangle) exposed phase pure c-GaN. However, Aspect Ratio Trapping could not be observed as described in literature.
Overall, these experiments show that NSAG of c-GaN on 3C-SiC (001) is possible and qualitatively follows the model proposed by Gridchin et al. [Gri22]. However, the effects of Nitrogen ad atoms surface behavior can not be totally neglected when SAG is conducted at temperatures of 870°C. On nano scales NSAG works, but there is a lot of potential left for optimization. One aspect of further analysis should be to see grain morphologies with respect to substrate temperature and a Ga BEP optimized for selective growth. If there is a substrate temperature promoting lateral growth this could help. Also employment of miscut substrates can help to increase homogeneity of selectively grown GaN, as stacking faults exhibit a preferred orientation [Lee19b].

4.1.5 GaN growth on EBL patterned SiO_2 on 3C-SiC

Within this section, growth on Electron Beam Lithography patterned SiO_2 masks is discussed. First, growth on V-shaped grooves in analyzed to see if cubic nucleation on <111> facets of 3C-SiC (001) is possible. Besides that growth in EBL patterned holes is discussed to narrow down limitations of the geometry of the PAMBE chamber (maximum aspect ratio).

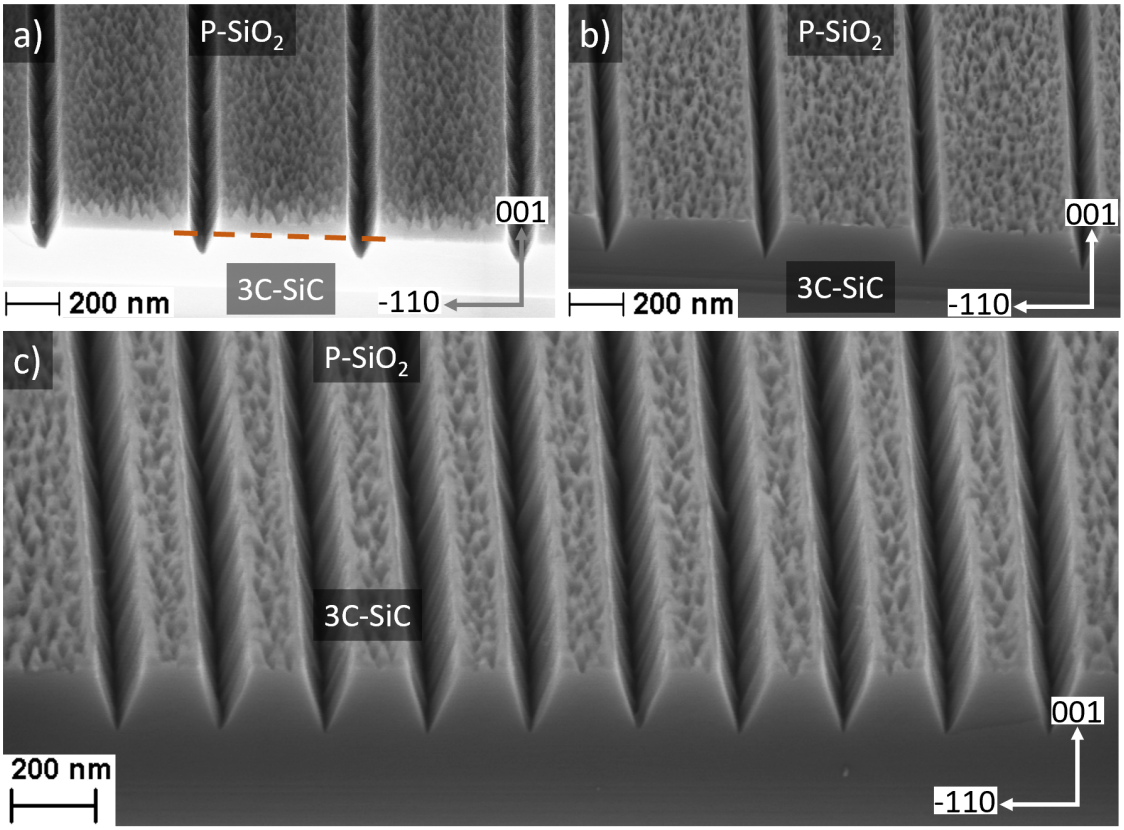

Figure 4.14: SEM images of cleaved EBL patterned samples after RIE with SF_6 with slightly different etching times (90 s a) and 105 s b) and c)). Grooves are orientated along [110] approximately dissecting <111> facets and expose and include an angle of about 55°.

4.1.5.1 V-shaped grooves

Kemper [Kem14] observed defect free c-GaN nucleation on <111> facets of 3C-SiC. In order to reproduce this observation, V-shaped grooves were patterned following the work of Littmann [Lit]. When Littmann conducted growth on <111> facets of 3C-SiC the GaN nucleated on all surfaces. Therefore, the experiment is conducted again with parameters leading to NSAG. While Littmann removed the SiO_2 mask,

acting as a hard mask for SF_6 RIE of 3C-SiC, it is left in this thesis to suppress unwanted nucleation on the 3C-SiC (001) surface between the grooves.
Figure 3.5 and section 3.5 depict and explains the process of Electron Beam Lithography (EBL) and the achieved structures as transferred into SiO_2. Figure 4.14 shows SEM 45° tilted images of two samples after SF_6 RIE. The image a) depicts a sample etched for 90 s, b) and c) depict a sample etched for 105 s.
As visible in figure 4.14, 90 s of SF_6 RIE yields V-shaped grooves but with a very round tip. Increasing the etching time to 105 s results in sharp V-shapes. The included angles reach from 55° to 60°. This causes a deviation from <111> facets of 5° to 7.5°. However, parameters did not allow for more shallow grooves. Probably, this could be fixed by changing the grooves dimensions within the SiO_2. Nevertheless, such V-shaped grooves approximately dissect <111> facets of 3C-SiC.
Ín both cases the EBL resist was not removed before SF_6 RIE but was not able to withstand the RIE process. Furthermore, the SiO_2 is damaged badly. For 105 s of etching there is no interface visible indicating that the SiO_2 mask was nearly, completely etched away. Process development revealed, that the SiO_2 mask remains intact but is rough. Roughness was not measured by means of AFM but SEM images show peak to valley distances of up to 100 nm in the SiO_2 mask.

4.1.5.2 GaN growth on V-shaped grooves

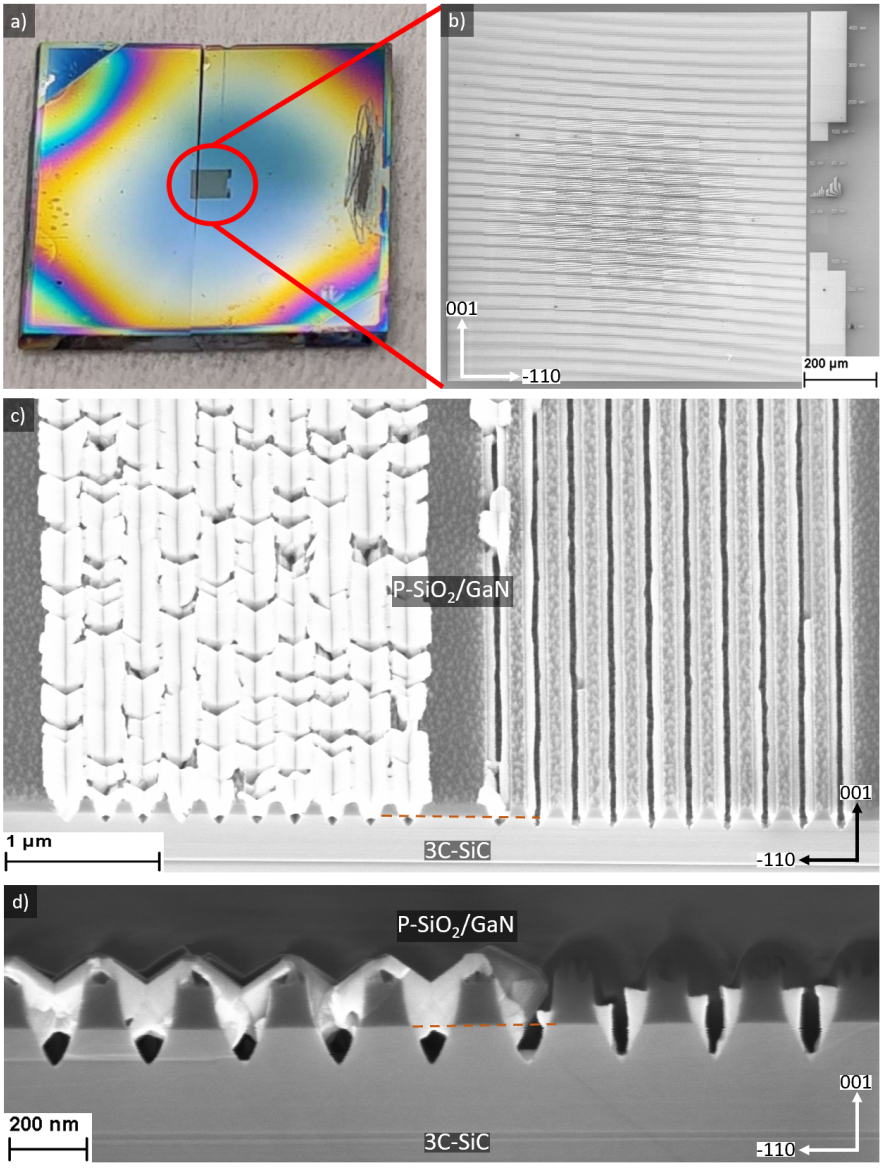

Figure 4.15: Optical photograph and SEM images of EBL patterned and overgrown samples. a) Photograph of a sample overgrown selectively. The e-beam structured part is shown in the cetner of the image. The colours of the film outside the structured area is due to thickness variation of the epilayers as a result of a thermal gradient. It also shows that grooves are always aligned towards the scratch (right side of the sample). b) SEM image of the utilized EBL pattern as already depicted in figure 3.5. c) and d) 45° angled-view and side-view SEM images of the first result using parameters slightly deviating from overgrowth of NSL patterned SiO_2/3C-SiC (T_{sub}=935°C, BEP_{Ga}(1000°C)=10^{-6} mbar).

The first overgrowth of V-shaped grooves was conducted at slightly adjusted parameters compared to overgrowth of NSL patterned SiO_2/3C-SiC (001). Substrate temperature was set to 935°C and Ga cell was operated at 1000°C, resulting in a BEP of $1{\cdot}10^{-6}$ mbar, in anticipation of a different III/V flux ratio necessary for NSAG on such patterns. This will be discussed in further detail later on. The sample was rotated during the 3 h growth.
Figure 4.15 a) shows an optical photograph of another selectively overgrown sample that will be discussed in detail later. Here it serves as an orientation of how samples look like after overgrowth and how the nanoscopic patterns are aligned on a macroscopic scale. The grooves are patterned in a way, that always makes them point towards the scratch (seen in figure 4.15 a) on the right side of the sample). This will be important for precise alignment of the Ga impingement later on. Picture b) shows the general EBL pattern utilized as described in section 3.5.
Image c) and d) show 45° angled-view and side-view of the cleaved overgrown sample. The SiO_2 mask is still intact but rough. However, the growth remains selective. On the small scales depicted, no parasitic growth happened, despite the extreme roughness. Furthermore, different behaviour comparing the 10 grooves on the left and on the right was observed. This is caused by APD's from the 3C-SiC substrate. The APD boundary is directly underneath the barrier between the groove batches. The GaN grains grown in the left batch of grooves expose a characteristic V-shape already observed when overgrowing NSL patterned SiO_2. Within the other APD's grooves the GaN grains tend to form narrow trenches. In both cases the grooves were not filled bottom up and show large gaps in the base of the grooves.
While the selectivity was sustained in this first try, the morphology and filling of the grooves is not satisfying. Also APD's seem to have a big influence when overgrowing V-shaped grooves. In order to properly fill the grooves, Ga BEP was increased to a BEP of $2.9{\cdot}10^{-6}$ mbar. Substrate temperature was kept at 935°C. The sample was rotated during the 3 h growth.
Figure 4.16 a) and b) depict side-view SEM images after overgrowth and cleaving. Again very different behaviors of the GaN grains were observed with respect to the APD's. The APD depicted in a) shows some filled grooves and some gaps at the grooves bases.

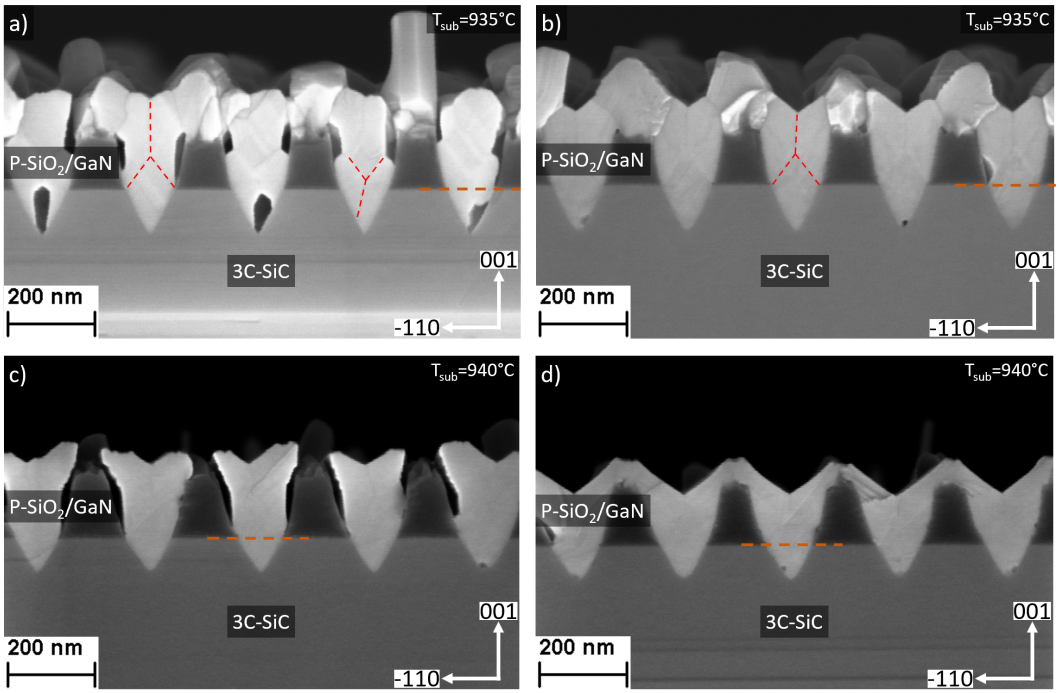

Figure 4.16: SEM side-view images of two cleaved samples patterned with V-shaped grooves overgrown with a Ga BEP of $2.9{\cdot}10^{-6}$ mbar at different substrate temperatures. Images were taken across the differend APD's. SiO_2/3C-SiC interface is indicated by a dashed line. Grain boundaries within GaN grains are indicated by red dashed lines.

In the first case, the grain boundaries form the typical V-shape on top of the grain. In the second case, a grain boundary coming up from the grooves base is visible. In the middle of the grain, it forms a rectangle. Above the rectangle, the V-shape forms again. The side-view along the other APD, depicted in image b), shows clean filling of the groove and only one pattern of grain boundaries. It looks like the GaN grown within the grooves consists of 3 grains at least. Growth was not selective in this case. To restore selectivity, the next sample was grown with a 5°C increase in substrate temperature. The results are imaged in form of side-view SEM images in figure 4.16 c) and d). The small increase in substate temperature not only restored perfect selectivity, but also lead to clean bottom up filling of the grooves. Both domains show V-shaped grains without any obvious boundaries. This does not necessarily mean, that there are no grain boundaries as they not appear visible in SEM every time. On the APD depicted in image c) the GaN grains somehow do not get in contact with the SiO_2 and don't show such distinct V-shapes compared to the grains depicted in image d).
The sample depicted in figure 4.16 a) and b) was also prepared for TEM with x-section mechanical dimple grinding followed by an ion milling step in a GATAN PIPS.

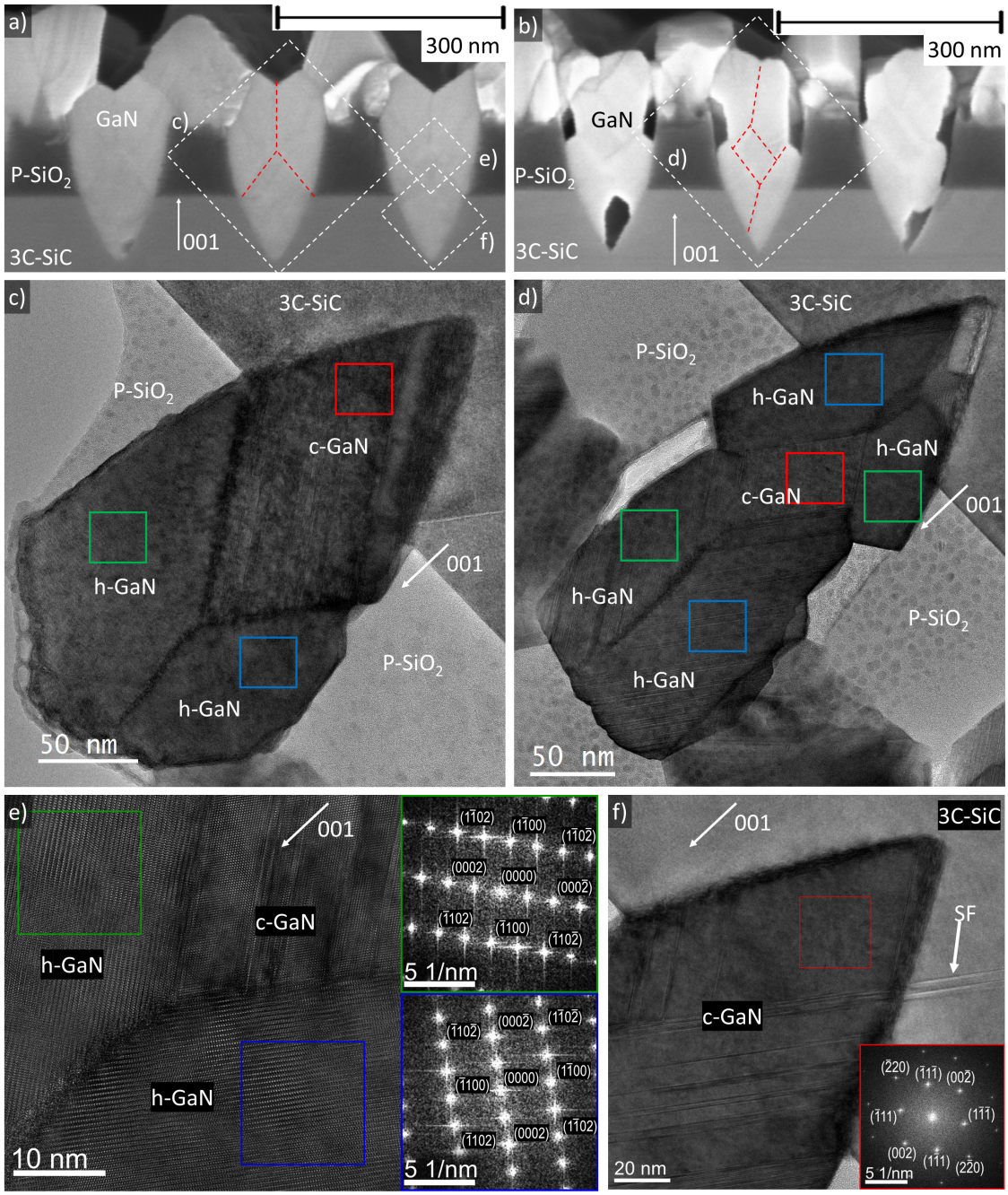

Figure 4.17: a) and b) enlarged SEM images from the sample depicted in figure 4.15 a) and b), showing side views of different APD's of overgrown V-shaped grooves on 3C-SiC. Overgrowth was conducted at 935°C and was not selective. Red dashed lines indicate grain boundaries. White dashed rectangles serve as an eye guide to show on what part of comparable grains TEM bright field measurements were conducted. Fast Fourier Transform inlets expose areas of hexagonal (blue, green) and cubic (red) Gallium Nitride. The shown FFT's originate from the images e) and f). Images c), d), e) and f) show TEM bright field images of the different types of observed grains. c), e) Triple grain boundary as a consequence of cubic to hexagonal transition. d) Six grain boundaries as a consequence of a double phase transition. f) Enlarged tip area exposing phase pure c-GaN. Growth always turned towards hexagonal twin formation due to sample rotation.

Figure 4.17 a) and b) show enlarged images of the aforementioned sample with additional marks, acting as eye guides for the TEM bright field images. They depict side-views of of different GaN APD's after overgrowth at 935°C and a Ga BEP of $2.9{\cdot}10^{-6}$ mbar for 3 h while being rotated.
Red dashed lines indicate grain boundaries. White dashed rectangles mark where TEM images, shown in c), d), e) and f) were taken. The colored rectangles mark positions where Fast Fourier Transform (FFT) resulted in patterns comparable to the FFT's given in the images e) and f), revealing the GaN phase.
Blue and green rectangles mark hexagonal GaN originating from opposing <111> facets of 3C-SiC or c-GaN. Red rectangles mark c-GaN grown on <111> or <0001> facets of 3C-SiC or h-GaN. The depicted FFT's originate from the images e) and f). Indexation was done by simulation of the hexagonal and cubic crystals by CaRine [C B22]. The software allows to project the lattice into [110] zoneaxis orientation and simulate FFT patterns.
TEM measurements were taken from comparable grains of the prepared sample and not from the exact same grain that is depicted in the SEM images. The pictures c) and d) show examples of whole grains with representative boundary structure compared to GaN grains observed by SEM. In the case of cubic GaN nucleation (c), hexagonal GaN emerges from the <111> facets after contact with SiO_2. Three grain boundaries can be seen as a result, with one reaching the top of the grain. In case of hexagonal nucleation (d), the hexagonal growth fronts merge with a tetrahedron bonding angle of 109.47°. This causes a hexagonal to cubic phase transition, as visible in figure 4.17 and confirmed by FFT [Liu16].
However, after a certain size of the cubic grain hexagonal GaN emerges from <111> facets. Two phase transitions also explain the occurrence of six grain boundaries as indicated by SEM images. Once the second transition happens, GaN forms hexagonal twins on the opposing <111> facets in both cases (c) and d)). This triple boundary is enlarged in picture f). FFT inlets expose the cubic to hexagonal phase transition and formation of hexagonal twins. The same process is probably happening when overgrowing NSL patterned SiO_2 masks as the characteristic V-shape was also observed there. At this point sample rotation is suspected to cause the V-shape. Due to rotation, opposing <111> facets are exposed to the Ga beam in turn. Therefore the III/V ratio is oscillating all the time. As a nitrogen rich environment promotes hexagonal phase, sample rotation is probably unfavorable.
Nevertheless, Figure 4.17 f) shows that it is possible to grow phase pure cubic GaN in V-shaped grooves along [110] approximately intersecting <111> facets of 3C-SiC.
In order to test the influence of sample rotation during overgrowth, two samples were patterned by EBL with the same structure described in section 3.5. Patterns were not transfered into the 3C-SiC by SF_6 RIE, but into the SiO_2. Therefore it consists of U-shaped grooves and holes, comparable to NSL patterned SiO_2. The sample was overgrown at 955°C and with a slightly higher Ga BEP of $3.6{\cdot}10^{-6}$ mbar.

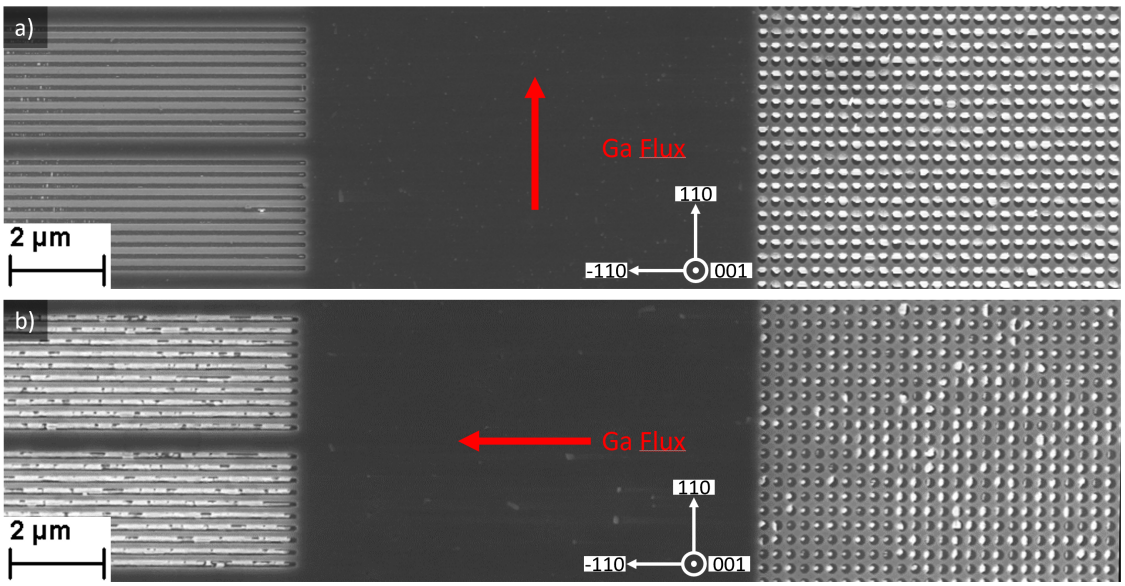

Figure 4.18: Top-view SEM images of two samples covered with EBL patterned P-SiO_2, overgrown at 955°C and with a Ga BEP of $3.6{\cdot}10^{-6}$ mbar. Overgrowth was done for 3 h and without rotation. Samples were either orientated perpendicular a) or parallel b) to the surface projection of the impinging Ga flux.

III/V ratio and substrate temperature were both increased to see if the growth rate is influenced by just offering more material. Both samples were overgrown for 3 h without rotation. With the help of the big scratch, the grooves were aligned parallel and perpendicular to the impinging Ga flux. The substrate holder is fixed in the manipulator by a certain number of small teeth like metal beams. The sample was placed in a way, that the scratch on the surface points towards such a metal beam. Once transfered into the manipulator, the substrate holder was rotated to make the scratch and metal beam point towards the glowing Ga cell. The normal of the sample holder is already very parallel to the normal of the Ga cell. However, no cell is perfectly perpendicular to the substrate as cell dimensions do not allow this. The idea of the explained alignment is, that the projection of the Ga cell normal vector on the 3C-SiC surface was paralleled to the grooves.
Figure 4.18 depicts top-view SEM images of both samples after overgrowth. Red arrows show the Ga flux impingement vector projected onto the surface. The sample depicted in image a) was purposefully aligned to have the grooves perpendicular to Ga flux, while the sample shown in picture b) was aligned to have the grooves parallel to the Ga flux. Both alignments are confirmed by the position of GaN grains in the neighboring holes. Both cases show GaN grains on the sidewalls of the mask with respect to the impinging flux. If Ga flux is perpendicular to the grooves nearly nothing is deposited at all. If Ga flux is parallel to the grooves regular selective growth can be observed. The alignment itself was surprisingly easy and was

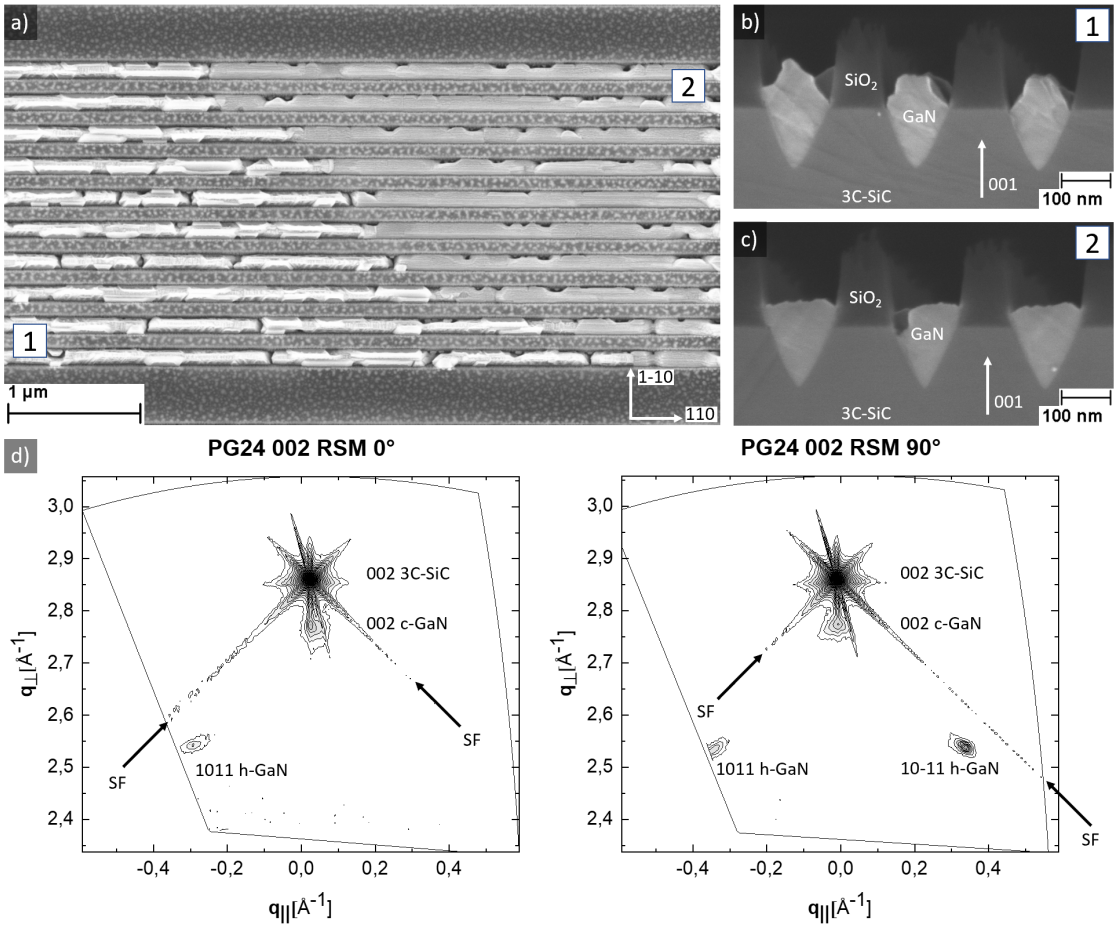

Figure 4.19: SEM images and RSMs along both main azimuths of an overgrown sample without rotation at 955°C and with a Ga BEP of $3.2{\cdot}10^{-6}$ mbar for 3 h. Images a), b) and c) depict top- and side-view images taken by SEM. Side-views of each domain denoted with numbers 1 and 2. Graphs in d) show RSMs of the 002 reflections along [110] (0°) and [1-10] (90°). Hexagonal phase content was estimated to be 44%.

successful in the first try.

This observation confirms the assumption made earlier. Sample rotation results in oscillating III/V ratios, as Ga can only reach the bottom of grooves if grooves and Ga cell normal are properly aligned. As a consequence, samples with EBL patterned grooves will not be rotated during overgrowth anymore, but properly aligned with respect to the Ga cell.

To visualize the effect on V-shaped grooves the experiment was repeated, but this time the pattern was transferred to 3C-SiC. The sample was overgrown at 955°C and a slightly decreased Ga BEP of $3.2{\cdot}10^{-6}$ mbar to get a better selectivity. With proper alignment and without rotation the sample was overgrown for 3 h.

Figure 4.19 shows SEM images and RSMs along both main azimuths of the overgrown

sample without rotation. The images a),b) and c) show top- and side-view graphics taken by SEM. Graphs d) show RSMs of the 002 reflections along [110] (0°) and [1-10] (90°).
Turning off the rotation and alignment of the grooves eliminated dominant V-shape of GaN grains grown selectively. However, top-view SEM image (a) shows a significant difference in morphology for each APD, again. While GaN grains in one domain look rough and sometimes show V-shapes (1), GaN grains grown in Domain 2 look smooth compared to the other domain. This is also visible in the side-view (b),c)). GaN grains from domain 1 look very rough with no dominating facet. In comparison, grains from domain 2 look somewhat smooth and the surface could be (001) of c-GaN. In both domains grooves are filled from the bottom up without gaps. Furthermore, no grain boundaries were observed. However, the growth rate could not be increased by increasing substrate temperature and BEP.
Figure 4.19 d) depicts 2 RSM's along the [110] and [1-10] azimuths. For this measurement the center structure was cleaved out of the sample to avoid signal from parasitically nucleated GaN on colder parts of the substrate. Each map was integrated for 24 h without any slits behind the hybrid monochromator to have maximum intensity. This is necessary to get any considerable signal out of these tiny deposited volumes. The strong faceted 002 reflection originates from the 3C-SiC substrate. Facets indicate SF from 3C-SiC. Surprisingly, signal to noise ratio is big enough to see multiple reflections of GaN. Just below the 002 reflection of 3C-SiC, a 002 reflex of c-GaN can be measured. However, both directions are accompanied by hexagonal GaN grown on <111> facets [Fre17]. Taking integral intensities of all reflections into account, hexagonal phase content was estimated to be 44%. Usually hexagonal reflections are well within the map. Here, the 1011 reflection is barely inside the mapped area, indicating strained GaN.
At this point multiple strategies are thinkable to further improve surface morphology, homogeneity and phase purity. One option would be to optimize III/V ratio with respect to substrate temperature and selectivity from about 870°C to 970°C, to get optimal parameters for NSAG on V-shaped grooves. NSAG could be achieved by variation of Ga and N fluxes for a fixed substrate temperature. However, such optimizations are very time consuming and may only lead to good results within one of two APD's. Growing thin films on unpatterned 3C-SiC is also known to result in APD's but they don't appear as different as observed in case of NSAG on <111> facets. Another option would be to switch from 3C-SiC to c-GaN buffer as a substrate. Homoepitaxial overgrowth could be favorable. Again, this would be very time consuming as no recipes exist for V-shaped grooves in c-GaN, yet. The most feasible option, within the given time, was to try to avoid APD's all together.
As reported by Lee et al. APD's are suppressed by employing 3C-SiC (001) with 4° miscut towards [110] [Lee19b]. To get rid of inhomogeneities introduced by APD's such miscut substrates were employed. Two samples were carefully prepared to have

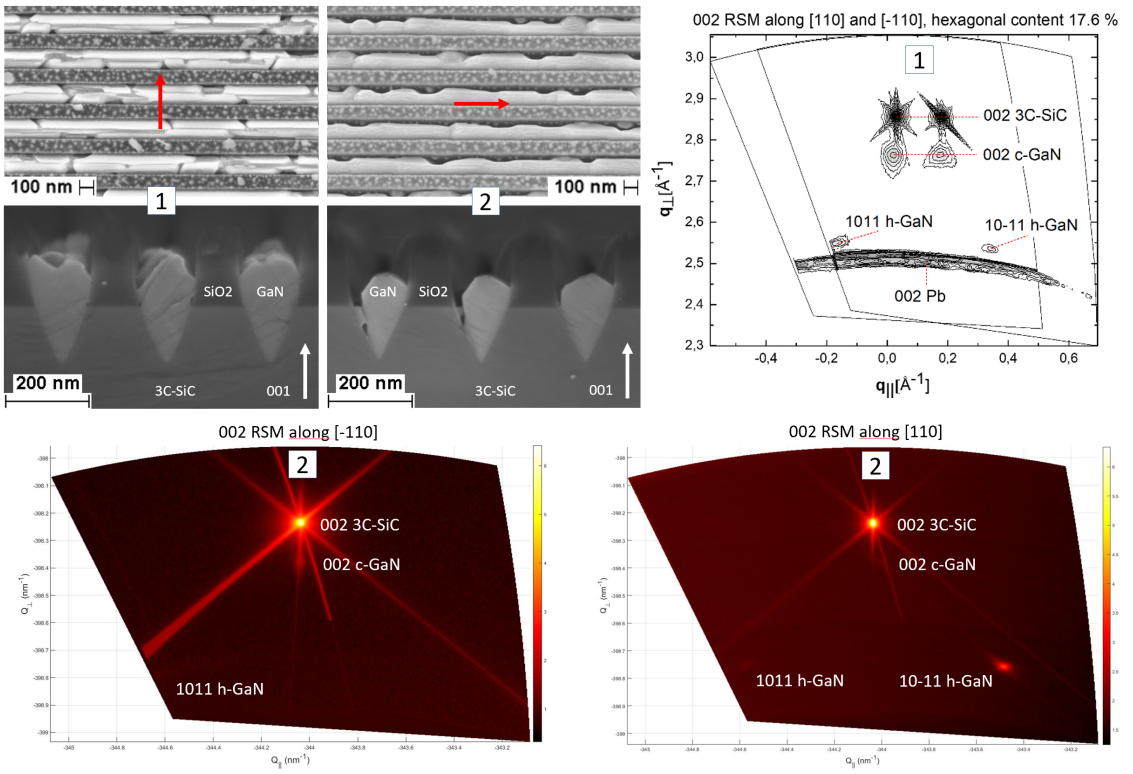

Figure 4.20: SEM images and RSMs of two overgrown samples employing 3C-SiC with 4° miscut towards [110]. Miscut orientation is indicated with a red arrow. V-shaped grooves were patterned perpendicular (1) and parallel (2) to miscut and were overgrown without rotation at 950°C and with a Ga BEP of $3.6{\cdot}10^{-6}$ mbar for 3 h. RSM's of 002 reflections along [110] and [-110] are depicted. Hexagonal phase content was estimated to be 17.6% and 95% for grooves orientated perpendicular and parallel to miscut, respectively.

grooves parallel and perpendicular to miscut (see figure 4.20). This was controlled by means of HRXRD multiple times to ensure correct alignment. after precisely estimating miscut orientation, with respect to the 1x1 cm^2 sample, direction of miscut was indicated by an arrow, scratched into the backside.
After patterning with EBL and transfer with RIE, both samples were overgrown at 950°C with a Ga BEP of $3.6{\cdot}10^{-6}$ mbar for 3 h. Both times the grooves were aligned parallel to the projected Ga cell normal vector as described earlier (see figure 4.18). Figure 4.20 depicts SEM top- and side-view images and RSM's of the 002 reflections along both azimuths. Different plotting of RSM's is a result of different machines utilized. Measurements on grooves perpendicular (1) and parallel (2) to miscut were taken in a malvern X'Pert pro and Rigaku smartlab, respectively.The measurement on sample (1) was masked with led tape, resulting in a Debye-ring. Both maps were plotted in one graph as the miscut displaces the reflections in reciprocal space along

both azimuths. The measurement on sample (2) was done with lateral selectivity by the fine beam of the machine. As the employed copper tube of the Rigaku machine is operated with about 3 times more power, the intensity is still sufficient with a narrow beam. However, resulting data files were way to large to handle with Origin. Therefore, data is plotted with Rigaku software and looks a little different.
SEM images show that each sample is uniform without any APD's, but the respective morphologies are very different. Sample (1) shows a very grainy structure with indications of emerging V-shapes. Nevertheless, no grain boundaries were visible in side-view. Sample (2) shows smoother surfaces but a wide gap on the upper part of the grooves if observed from top-view. Side-view shows this gap on the left. While not as smooth, grains on both samples look very comparable to results on substrates without nominal miscut. It looks like morphology of both APD's was mimicked by choosing different groove orientations with respect to miscut.
RSM's of both samples, depicted in figure 4.20, expose very different phase contents. RSM's for grooves parallel to miscut (2) show nearly invisible c-GaN reflections but a very bright 10-11 h-GaN reflection along [110]. Probably hexagonal growth on the left facet of the grooves (SEM side-view) is dominant, resulting in nearly phase pure hexagonal GaN. RSM's of sample (1) with grooves perpendicular to miscut show dominant cubic phase with a hexagonal content of about 17.6%. Within this work, this was the least hexagonal content achieved when overgrowing V-shaped grooves approximately dissecting <111> facets of 3C-SiC. Hexagonal content was reduced to about 44% by just employing miscut substrates.

4.1.5.3 Aspect Ratio Limit

Besides structuring V-shaped grooves, EBL was also employed to pattern round and square hole arrays with opening diameters ranging from 100 nm to 400 nm. Furthermore, a test pattern was developed (figure 3.6) to narrow down the Aspect Ratio Limit (ARL) of our PAMBE chamber. In the end, these different hole arrays served three purposes.

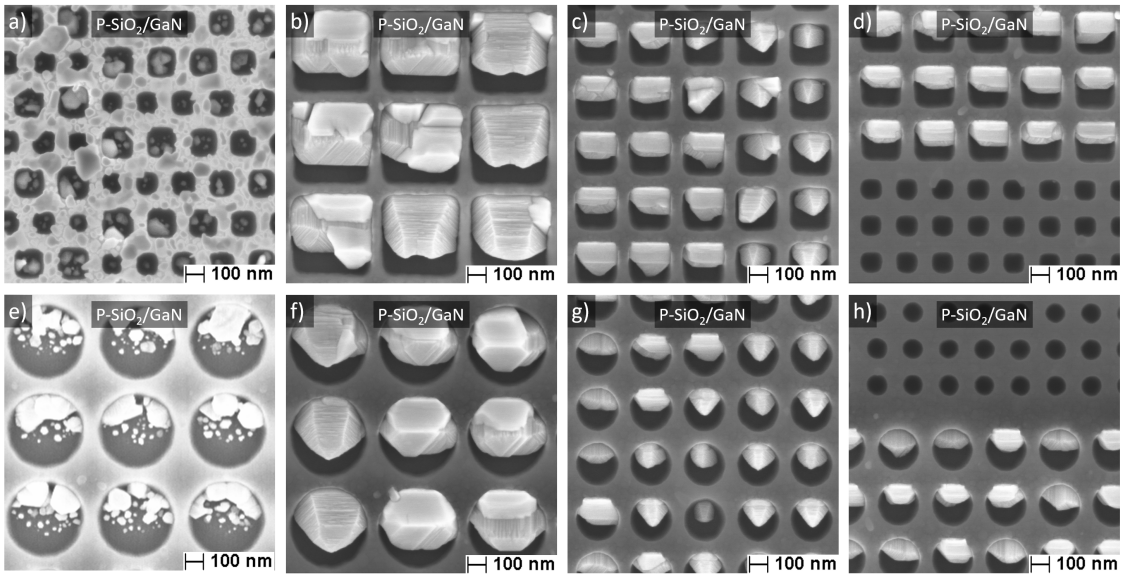

Figure 4.21: Top-view SEM images of different overgrown round and square hole arrays with opening diameters of 400 nm (b,f), 200 nm (c,g) and 100 nm (d,h). a),e) oxidized substrate led to polycystalline GaN.

Figure 4.21 depicts several top-view SEM images of overgrown hole arrays in EBL patterned and 200 nm thick SiO_2. 3C-SiC substrate was not etched. Depicted samples were overgrown at 955°C with a Ga BEP of $3.6{\cdot}10^{-6}$ mbar without rotation for 3 h. The image a) and e) show overgrown patterns with very poly crystalline GaN. As no SF_6 RIE was conducted, the EBL resist had to be removed somehow. Usually this is done by burning the resist with an O_2 RIE process. However, this process deterioates the surface of the 3C-SiC surface. The bare 3C-SiC is probably oxidized by the oxygen plasma. Unfortunately, this also happened to the developed test structure and the results from this are not very meaningful. Nevertheless, the smallest holes only showed tiny grains inside, indicating an ARL of (1.8±0.1). At least, these samples demonstrates the fatality of treating bare 3C-SiC with an oxygen plasma. The pictures b), c), f) and g) image selectively overgrown round and rectangular holes with 400 nm and 200 nm in diameter. They impressively demonstrate the possibilities of NSAG on hole arrays at even further elevated temperatures. The highest temperature resulted in successful NSAG on NSL patterned SiO_2 masks was

955°C. Images were taken in a way that both APD's are within the picture. This can be seen by different SF distributions in the grains with respect to the [110] and [-110] directions.

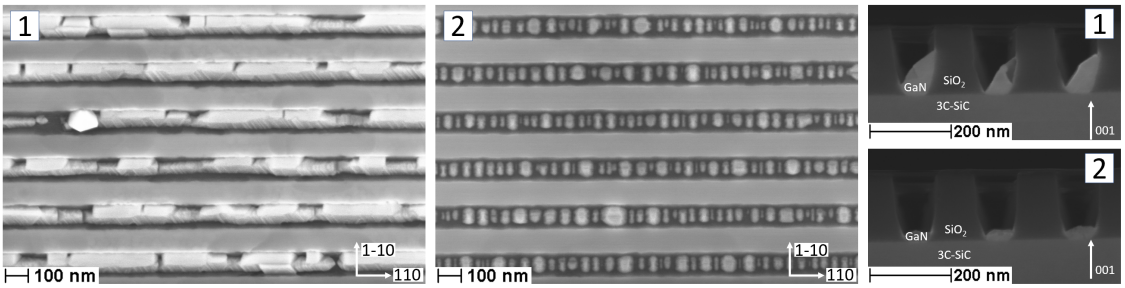

Figure 4.22: SEM images of a sample EBL patterned with U-shape grooves in P-SiO_2. Overgrowth was done at 955°C with a Ga BEP of $3.6{\cdot}10^{-6}$ mbar without rotation for 3 h.

Figure 4.21 d) and h) depict corner sections of round (h) and rectangular (d) hole arrays with different opening diameters. The partially filled holes have opening diameters of 200 nm, while the empty holes are 100 nm in diameter. As the mask is 200 nm thick, The ARL has to be somewhere just below 2. This is also underlined by he shadow edge within the partially filled holes, nearly dissecting the holes in half. Furthermore, this solidifies the assumption of neglectable Ga diffusion along 3C-SiC surfaces.
Figure 4.22 depicts the overgrown U-shaped grooves that were also patterned on the aforementioned sample. SEM top-and side-views were taken along both APD's, marked with 1 and 2. APD 1 looks like a one sided hexagonal grain emerged from a <111> facet. APD 2 looks smooth and could consist of small cubic GaN grains. However, phase was not estimated. Growth on U-shaped grooves could offer an elegant way to circumvent limitations introduced by the chamber geometry. In principle, there is no limit when employing U-shaped grooves in terms of aspect ratio, as sample and Ga cell can be aligned in a way, that the projected Ga flux vector on the samples surface is parallel to the grooves. However, the deposited amount after 3 h was very small. Additionally, if ART can be realized this way, defects could only be terminated in one direction. Maybe a combination with miscut substrates would yield promising results. NSAG on U- and V-shaped grooves was successfully demonstrated. Increasing the III/V flux ratio, aligning the impinging Ga flux and switching to 4° miscut 3C-SiC substrates resulted in a hexagonal phase content of as low as 17.6 % when selectively growing GaN on <111> facets of 3C-SiC. Furthermore, growth on holes and U-shaped grooves demonstrate NSAG down to scales as small as 100 nm, indicate an ARL of just below 2 and in addition shows possible options to achieve proper ART.

4.1.6 BCP Masks

In this section, growth on Block Co-polymer Lithography (BCP) patterned P-SiO_2/3C-SiC (001) and P-SiO_2/c-GaN (001) is studied to see if coalescence with dominant cubic phase is possible after NSAG. The BCP process is described in section 3.4.
The c-GaN buffer was deposited at a substrate temperature of 805°C with a Ga BEP of $2{\cdot}10^{-7}$ mbar for 30 minutes on a 2x2 cm^2 sample holder. Plasma cell was operated at 260 W and fed with 0,5 SCCM of N_2. A higher substrate temperature was chosen as this seems to yield smoother surfaces (see section 4.2). GaN growth at elevated temperature will be further discussed in section 4.2. After 30 minutes the RHEED showed a 2D pattern and the growth was interrupted. Post-growth characterization revealed a film thickness of about 40 nm, a roughness of 1 nm and a hexagonal phase content well below 1 %. With this properties the c-GaN buffer was feasible for further processing. The BCP process was carried out by Mr. Daniel Kool, a PhD student of the working group of Prof. Jörg K. N. Lindner.

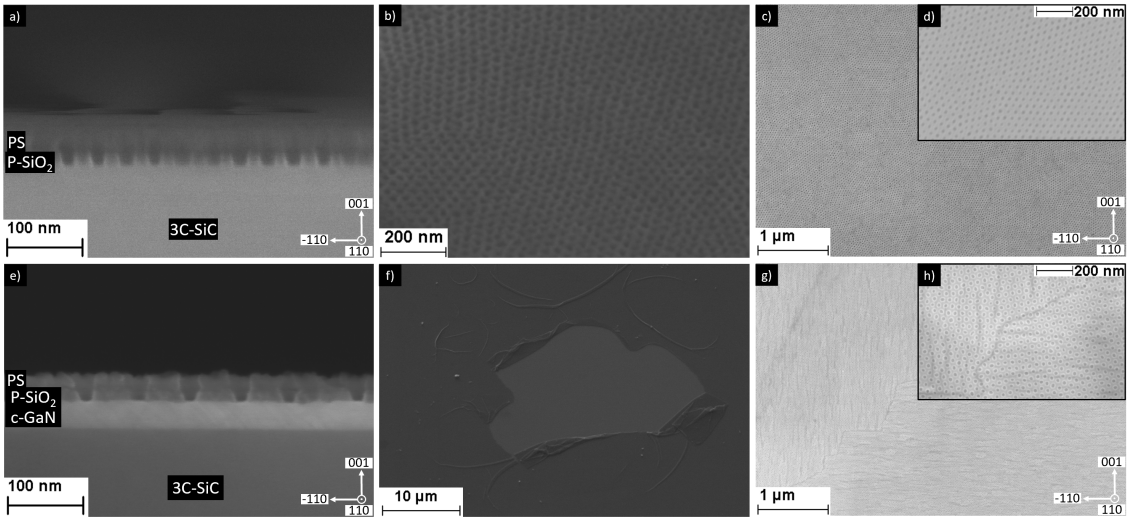

Figure 4.23: SEM images of the BCP patterned P-SiO_2 at different stages of the process on top of 3C-SiC (a), c), d)) and c-GaN (e), g), h)). a) and e) show a side-view after RIE processing of the P-SiO_2 with the mask still on top. b) and f) depict 45° angled-views of the mask after RIE (b) and after 30 min of H_2SO_5 etch (f). c), d), g) and h) top-view pictures imaging the surfaces after complete removal of the PS mask. c) and d) depict the final structure before overgrowth with a c-GaN buffer below.

Figure 4.23 shows different SEM images of the BCP patterned SiO_2 during different stages of the process. a) and e) depict side-views of the samples after RIE processing of the SiO_2. Different trys with different etching times were performed. A total RIE time of 9 minutes was necessary to etch through the SiO_2 and to reveal the

substrates. Compared to etching of NSL patterned SiO_2 the etching rate of BCP patterned SiO_2 is significantly lower. This is probably caused by diffusion limitation

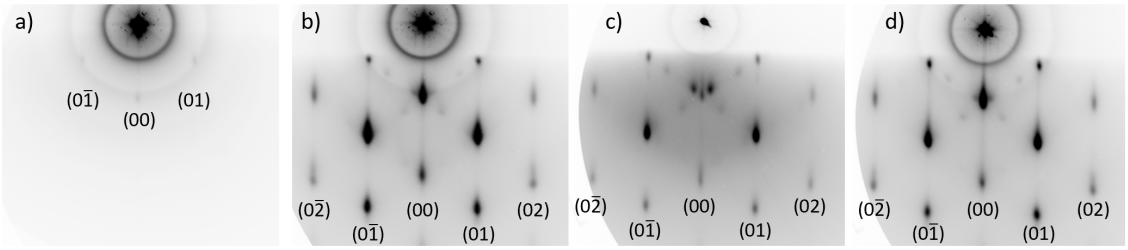

Figure 4.24: RHEED patterns along [110] after different stages of growth. a), b) Rheed patterns of GaN on P-SiO_2/3C-SiC after 10 and 120 minutes of growth, respectively. c) and d) RHEED patterns of GaN on P-SiO_2/c-GaN after 10 and 120 minutes of growth, respectively. Substrate temperature was 950°C. Growth was conducted with a Ga BEP of $3.2{\cdot}10^{-6}$ mbar for 2 h.

due to the small opening diameters of the holes. In both cases the holes have diameters of about 17 nm.
After RIE processing of the SiO_2 the PS mask has to be removed. Usually, this is done by a O_2 RIE process. As discussed in the previous section, this severely degrades the 3C-SiC surfaces and renders the substrates useless for NSAG. Therefore, piranha etch (H_2SO_5) was tested as described in section 3.4.
Figure 4.23 b) and f) depict 45° angled-views of the PS mask. After being exposed to H_2SO_5 for 30 minutes in a supersonic bath, the mask is only partially detached from the SiO_2 surface. This can be seen by small patches removed and wrinkles in the sticking PS layer (see fig. 4.23 f)). As the etch is violent, bubbles form and lift the sample. Once the sample floats, no H_2SiO_5 can reach the surface anymore. Therefore the samples were places upside down to ensure permanent contact of the masked surface to the etchant.
Figure 4.23 c), d), g) and h) show the samples after 120 minutes of treatment with H_2SO_5. c) and d) show the results on 3C-SiC. It is visible, that the SiO_2 mask is still intact and no residual PS is left. The same observations can be made on the c-GaN buffer (g) and h)). Furthermore, the c-GaN morphology is visible through the 20 nm thick SiO_2. It appears semi transparent for electrons.
Overgrowth was only tested once for each substrate. The parameters from overgrowing V-shaped grooves were adopted and the experiments were conducted at a substrate temperature of 950°C and with a Ga BEP of $3.2{\cdot}10^{-6}$ mbar for 2 h. Overgrowth was monitored via RHEED.
Figure 4.24 depicts RHEED images along [110] of both samples after 10 and 120 minutes of overgrowth. After 120 minutes growth was interrupted and both samples show a cubic but 3 dimensional pattern of GaN accompanied by slightly visible hexagonal reflections. From comparison of the pictures a) and c) a big difference in

nucleation time is possible. Homoepitaxial overgrowth seems to promote nucleation speed. After 120 minutes the GaN grown homoepitaxial also looks somewhat streakier. This could be a result of faster nucleation and therefore more time for coalescence. From RHEED the films looks 3D but highly cubic.

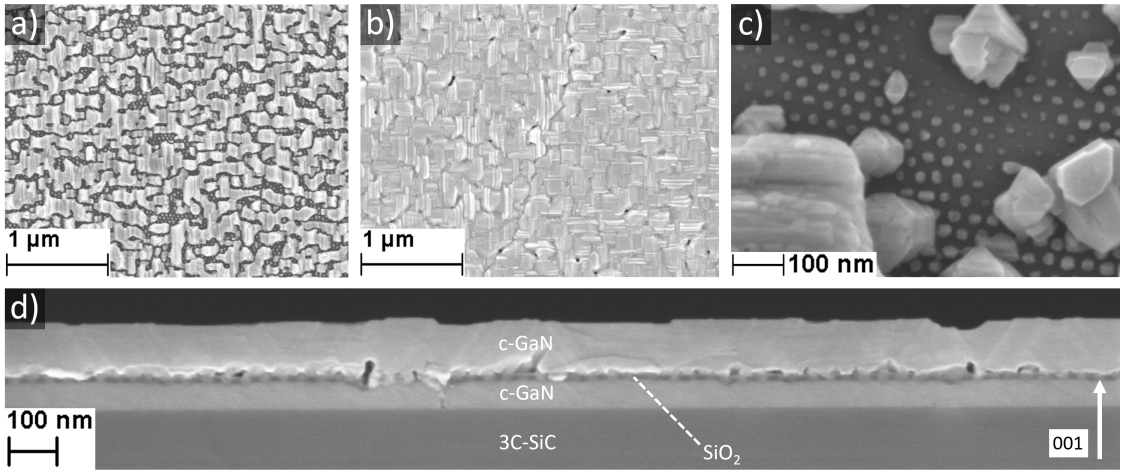

Figure 4.25: Top-view SEM images of the BCP patterned overgrown sample. Overgrowth was done at 950°C and a Ga BEP of $3.2{\cdot}10^{-6}$ mbar for 2 h. a), b), c)are taken at different positions from the center, a) center, b) 3-4 mm away from the center, c) from the samples edge, respectively. d) side-view along b).

After growth, the samples showed a color gradient comparable to the sample depicted in figure 4.15 indicating a negative temperature gradient from the center towards the samples edges. As a result, selectivity is different across the sample, as well as the deposited amount. This effect can be approximately interpreted as different stages of growth.
Figure 4.25 shows SEM images of the homoepitaxially overgrown sample. From observations with SEM both samples look comparable. Image a) depicts a top-view taken from the center of the sample. Growth was selective and single selectively grown GaN grains have coalesced to form a layer. However, the deposited amount in the center of the sample is not enough for full coalescence. Picture b) shows a top-view taken 3 to 4 mm from the samples center. A film with gaps and cubic facets was observed, indicating successful but partial coalescence at slightly lower temperatures. Image d) shows a side-view of that region. A closed layer with stacking faults resulting in steps at the surface is visible. From the side-view the layer looks coalesced and smooth. Image c) shows a corner section of the sample, suspected to be much colder. Here, selectivity is not good resulting in huge grains parasitically grown on the SiO_2 mask. However, one can see that every single hole in the SiO_2 mask is filled selectively. Due to the bad selectivity the Ga beam is cut from reaching

the surface by the big grains grown on the mask. In summary, these images confirm coalescence and NSAG down to scales of 17 nm.
Finally, the phase was examined by means of HRXRD. Figure 4.26 depicts 2 RSM's taken along [110] of both samples. RSM's along [-110] looked similar and are therefore not depicted here. Both maps show intense 002 reflections of 3C-SiC and c-GaN

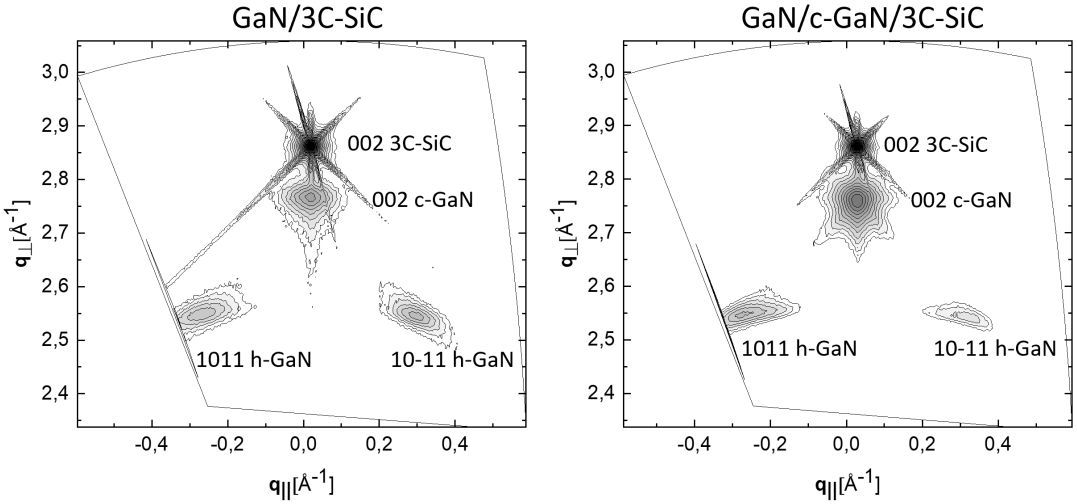

Figure 4.26: RSMs taken along [110] of overgrown P-SiO_2 masked samples structured with BCP. Employing a c-GaN buffer decreased hexagonal phase content from 44% to 29%.

but also show 1011 and 10-11 hexagonal reflections indicating hexagonal inclusions on <111> facets of the c-GaN grains. The heteroepitaxially overgrown sample with GaN/3C-SiC exhibited a hexagonal phase content of 44 %. The other sample, employing a c-GaN buffer, exposted a hexagonal phase content of 19 %. The buffer was taken into account by scaling the intensity of the 002 reflections of c-GaN to the layer thicknesses achieved. This is a rough approximation as the deposited amount varied laterally as shown in figure 4.25. With the buffer substracted, hexagonal phase content was calculated to be 29 %. Therefore the homoepitaxial process not only favors nucleation it also promoted cubic phase. Even without phase purity this experiments impressively demonstrate that coalescence after NSAG is possible. Further research of NSAG with GaN on BCP patterned growth masks is highly recommendable.

4.2 PAMBE of c-GaN at elevated temperatures

Throughout the whole section Gallium Nitride was grown on different structures and facets on 3C-SiC at elevated temperatures. In this final chapter, some basic results are presented, showing c-GaN films grown at 870°C. This substrate temperature is at least 100°C hotter compared to regular growth conditions as described in section 3.7. High temperature growth was conducted on bare 3C-SiC, 4° miscut 3C-SiC and on a c-AlN buffer. First growth runs on unpatterned substrates showed remarkable RHEED patterns during and after growth. Furthermore, at such high temperatures it was not possible anymore to estimate Ga coverage with the help of RHEED flashes. Post-growth characterization revealed very smooth surfaces but also a higher FWHM of 002 reflections, indicating more defects within the layer. Also the growth rate is slightly reduced from 150 nm/h to about 100 nm/h. All of this will be roughly sketched within this section.

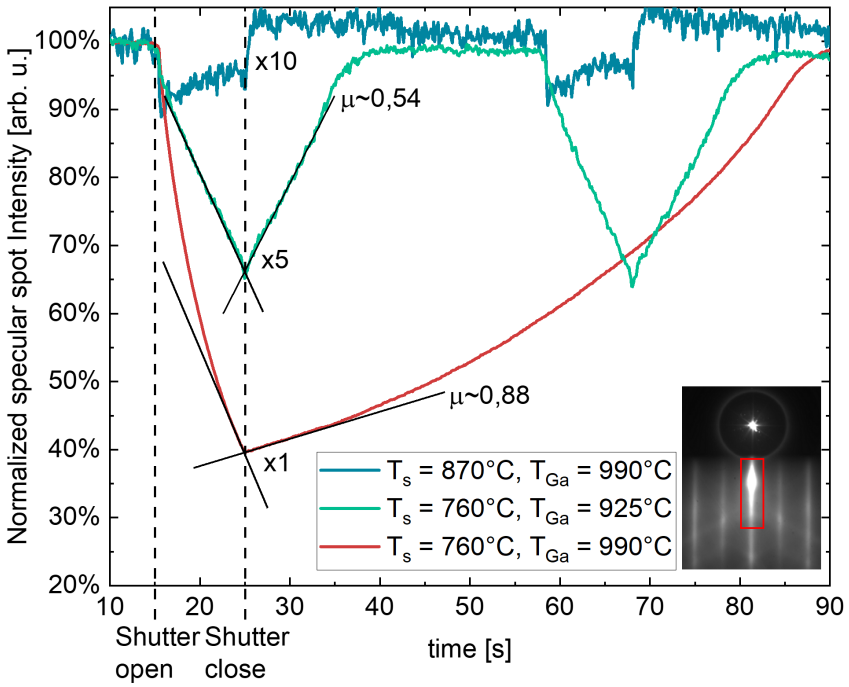

Figure 4.27: RHEED specular spot intensity along [110] during Ga flashes with different substrate and cell temperatures. By comparison of ad- and desorption time one can approximately estimate the sticking coefficient μ. For high temperatures this technique does not work anymore.

Figure 4.27 depicts the normalized specular spot intensity for three different parameter sets of substrate and Ga cell temperatures during a 10 s Ga flash on 3C-SiC. The Plasma cell is off. The green and blue curves are multiplied by 5 and 10, respectively.

At regular growth conditions, as described in section 3.7, with a substrate temperature of 760°C and a Ga BEP of $2{\cdot}10^{-7}$ mbar (T_{Ga}=925°C) the resulting sticking coefficient μ is approximately 0,54. With such settings the amount of adsorbing and desorbing Ga is roughly equal. If the Ga BEP is increased to $8.4{\cdot}10^{-7}$ mbar, the resulting sticking coefficient is about 0.88, indicating that the adsorption rate is alot higher then the desorption rate. Usually the adsorption and desorption are comparable and nearly equal. The same Ga flux results in nearly no intensity drop for a substrate temperature of 870°C.

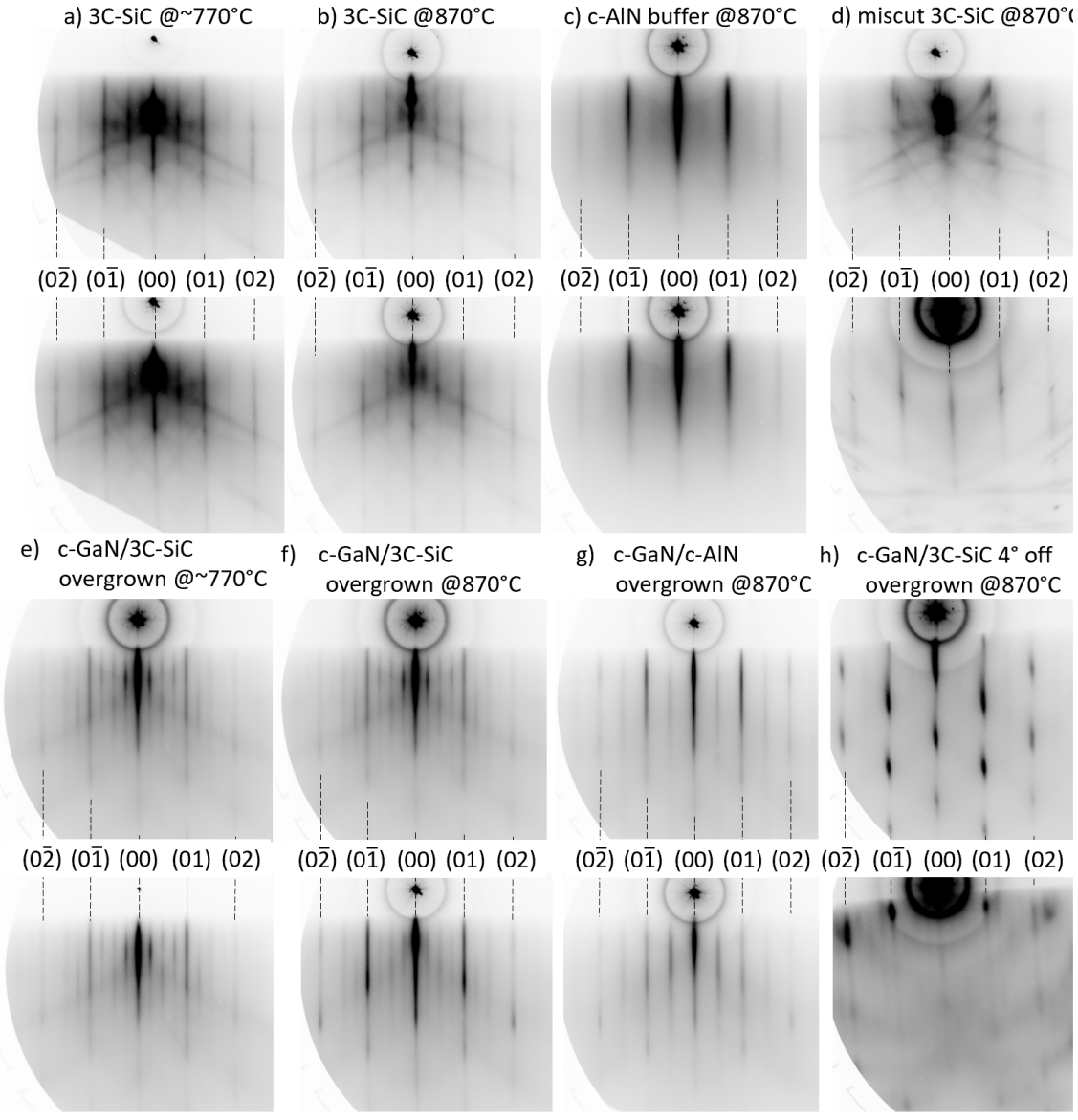

Figure 4.28: RHEED patterns along [-110] (top) and [110] (bottom) of exemplary samples before and after c-GaN deposition at different temperatures.

This implies, that most of the Ga adatoms reaching the surface desorb right away with very little residence time.
Alltogether, this could mean, that only a few Ga adatoms are present on the surface and nucleation together with N is very unlikely.
Figure 4.29 depicts several RHEED images of the mentioned surfaces before and after overgrowth with GaN at different substrate temperatures. In all experiments Ga BEP was set to $2{\cdot}10^{-7}$ mbar. Top and bottom row images show patterns taken along [-110] and [110] azimuth, respectively. Image a) and b) show the 3C-SiC surface prior to growth. Sharp and streaky reflexes together with Kikuchi lines indicate a smooth surface with APD's. The difference between both patterns is the diffuse scattering intensity that is just different from sample to sample. Besides that, a) and b) look comparable and both show 2x2 reconstruction. The c-AlN buffer, shown in images c), was deposited as thin as possible and is about 10 nm thick. In both directions, a perfectly 2D surface, with slight 2x2 reconstruction, is observable. Images d) shows the RHEED patterns along the main azimuths of the 4° miscut 3C-SiC substrate. The streaky pattern is made up of even smaller streaks, indicating a stepped surface after Hasegawa et al. [Has12]. The perpendicular direction only shows very weak streaks as most of the electrons are diffusely scattered on the steps edges.
The growth time was varied to achieve approximately 600 nm thick films for characterization. Overgrowth was done for 240 minutes at 770°C resulting in a growth rate of 150 nm/h. The other samples were overgrown for over 330 minutes and showed much lower growth rates of around 100 nm/h. Image e) shows a reference sample overgown for 240 minutes at about 770°C, optimized to keep a Ga monolayer on the surface all the time. After deposition a fully 2D RHEED pattern was observed in both directions. Streaks are slightly modulated due to overlap with Kikuchi lines still visible. Image f) depicts post growth RHEED images of a sample overgrown for 330 minutes at 870°C. Again sharp streaks with overlapping Kikuchi lines is visible. Both samples c-GaN shows 4x4 reconstructions after deposition. In conclusion, RHEED shows nearly the same surfaces after deposition at different temperatures. This was achieved without any optimization of the Ga coverage.
Figure 4.28 g) shows the RHEED patterns of an overgrown c-AlN buffer. Resulting c-GaN film was 700 nm after 360 minutes, resulting in a growth rate of about 116 nm/h. Again very sharp and intense streaks can be observed but this time with a 2x2 reconstruction. Also Kikuchi lines are not visible in this case. Nevertheless, the surface looks perfectly 2D along both azimuths.
Image h) depicts RHEED patterns of the overgrown 4° miscut 3C-SiC substrate. Along [-110] a very spotty pattern was observed. Streaks are still visible but the surface looks very 3D. This is probably due to steps roughening the surface by bunching. In the opposite direction along the steps a very weak but perfectly streaky pattern can be seen. The sample shows a 4x2 reconstruction.
The samples overgrown at 870°C also showed reconstructions in the RHEED patterns

throughout the whole growth. This is another hint that Ga coverage during growth is neglectable. It was already reported, that reconstructions are invisible as long as

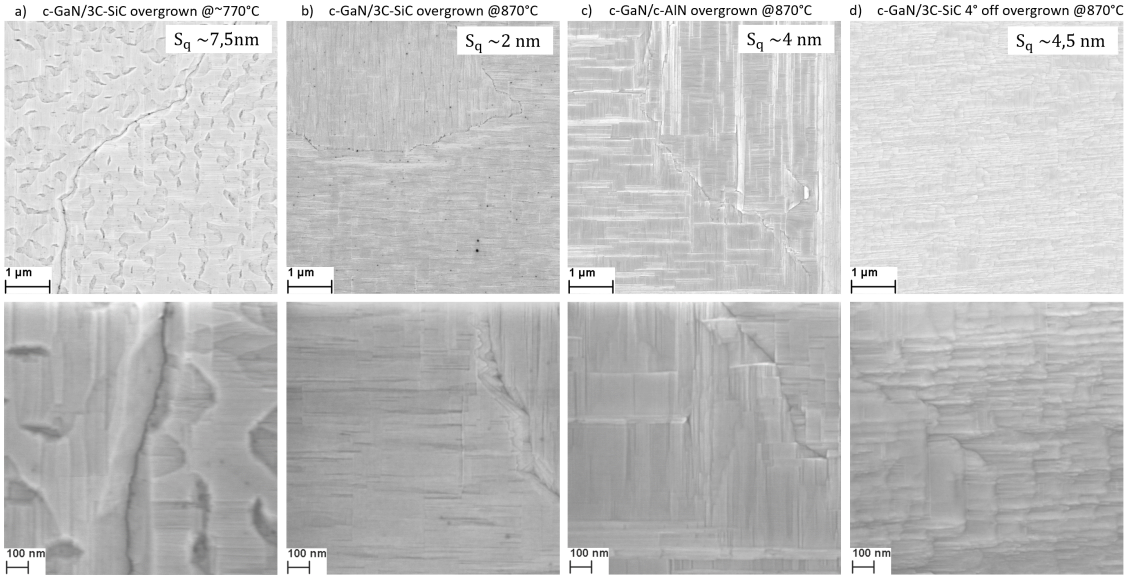

Figure 4.29: Top-view SEM images of exemplary samples after c-GaN deposition at different temperatures. Bottom row shows enlarged images taken from the surfaces depicted above with larger magnification. Inlets gives the roughness, estimated by 10x10 μm^2 AFM measurements.

the surface is covered with Ga. [As03].
Together, RHEED images imply that c-GaN can grown at elevated temperatures without noteworthy surface roughening or hexagonal inclusions. Furthermore, RHEED images show remarkably sharp lines combined with Kikuchi lines from the c-GaN surface, even without monitoring Ga surface coverage during growth. Figure 4.29 depicts top-view SEM images of c-GaN grown deposited on different surfaces at 770°C and 870°C. Depicted films have comparable thicknesses of about 600 nm at least. Top and bottom row pictures show the same surface with different magnifications. Inlets show surface roughnesses estimated by 10x10 μm^2 AFM measurements.
Images a) in fig. 4.29 show the surface of a reference sample grown under regular growth conditions as describes in section 3.7. While the roughness is a bit high, the surface morphology is representative. Surface roughness was estimated to be 7.5 nm. On the top image one can see a grain boundary as a result of APD formation. APD's show comparable morphologies with a 90° rotation. The enlarged picture shows fine steps in the surface accompanied by wrinkles. Fine steps probably stem from SF's, while wrinkles are a result of imperfections in Ga coverage during growth.
Pictures b) depict the surface of c-GaN grown on 3C-SiC at an elevated substrate of 870°C. Again, grain boundaries indicate APD formation. The black dots are some residue introduced by sample cleaning prior to SEM imaging. Unfortunately, it was

not possible to remove them. However, the surface was very smooth with a surface roughness of about 2 nm. Also the morphology changed. It looks like the surface is only roughened by fine lines and trenches with 90° angle in between. Again stacking faults are suspected to cause such facetation of the surface, indicating a cubic film.

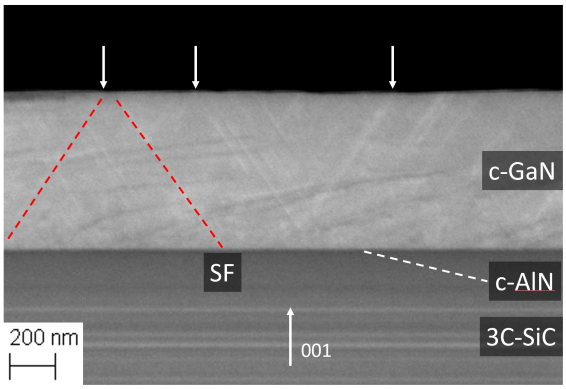

Figure 4.30: SEM side-view image of a c-GaN layer deposited on c-AlN/3C-SiC (001) at 870°C. Arrows indicate SF intersections with the surface. Red dashed lines highlight two SF as a guide for the eye. Horizontal features in the image are a result of surface imperfections after cleaving.

Wrinkles can not be seen anymore. On the enlarged image one can additionally see formation of <111> facets in proximity of the APD boundary. Figure 4.29 c) images the c-GaN surface after deposition on a 10 nm c-AlN buffer on 3C-SiC at 870°C. The surface shows dominant facetation accompanied by APD's. in this case the lines are broader, indicating SF bunching. Nevertheless, the films roughness is 4 nm and inbetween the bunched SF's, the surface looks very smooth. Figure 4.30 shows a SEM side-view of this sample. As the SF bunch, they appear visible in SEM imaging. Red dashed lines exemplary indicate two SF's reaching the samples surface. Arrows also indicate more SF's reaching the top of the film. These SF's probably become observable in top-view as lines as described earlier, roughening the surface.

Images d) in fig. 4.29 show a 4° miscut 3C-SiC (001) substrate, with the miscut being orientated towards [110]. In this case the growth mode changed and step flow growth with step bunching is observed. AFM revealed a mean step height of about 20 monolayers and a surface roughness of 4.5 nm. The enlarged image shows terraces with an average size of 241 nm.

Despite no big difference in the shapes of post-growth RHEED patterns (figure 4.28) the surfaces show very different morphologies. In general a hotter substrate resulted in a smoother surface, just roughened by SF as exemplarily shown in figure 4.30. This is promising as application of mechanisms for SF reduction are within reach.

Figure 4.31 shows RSM's, for the samples previously discussed, along [110] and [-110]. For the reference sample grown at 770°C, depicted in images a), only very thin lines, corresponding to SF, are visible. FWHM of 002 c-GaN reflection is about 26.25 arcmin. Hexagonal phase content was estimated to be 0.2%. Structurally, this reference is absolutely nominal.

Images b) shows the RSM's for c-GaN grown on 3C-SiC at 870°C. SF's appear to be braodened and not evenly distributed. The FWHM of 002 c-GaN

reflections are very different along both directions. The hexagonal phase content was calculated to be 0.7%. SF anisotropy, as also reported by Lee [Lee19a], is probably the cause of the APD depended morphologies, as observed in section 4.1.5.

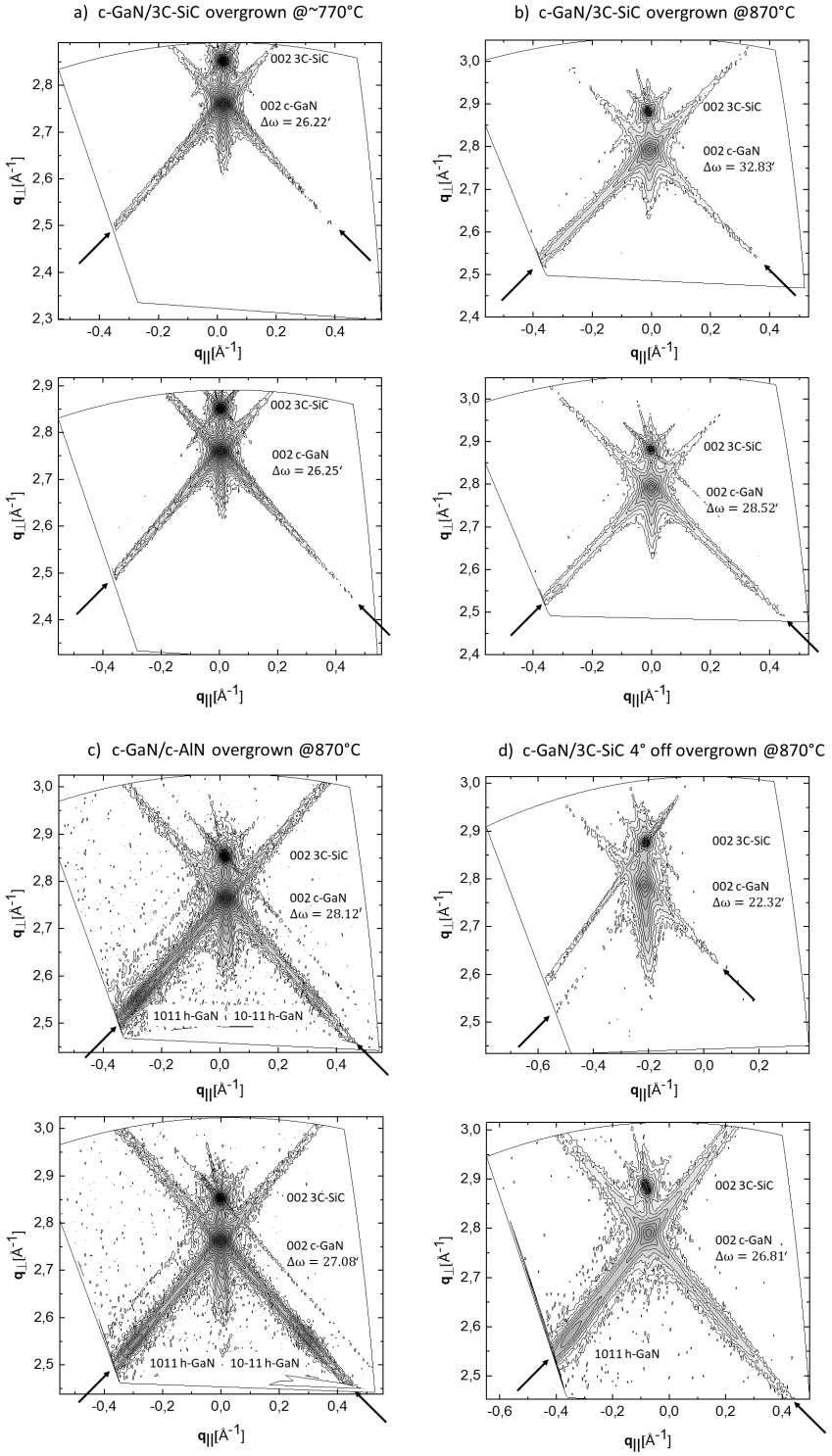

Figure 4.31: Reciprocal Space Maps (RSM) along [110] and [-110] of 002 reflections of four samples. a) c-GaN reference grown on 3C-SiC at 770°C. Hexagonal phase content 0,2 %. b) c-GaN grown on 3C-SiC at 870°C. Hexagonal phase content 0,7%. c) c-GaN grown on c-AlN/3C-SiC at 870°C. Hexagonal phase content 7 %. d) c-GaN grown on 4° miscut 3C-SiC. Hexagonal phase content 5 %. Black arrows indicate SF of the c-GaN layer.

For c-GaN grown on c-AlN buffer at 870°C Stacking faults, depicted in the graphs c), also appear do be not only broadened but also extended, indicating a higher SF density. While the FWHM of the 002 reflections of c-GaN are only slightly increased the hexagonal phase content rose to 7%. This may be surpressed by parameter optimization for growth on c-AlN. However, when grown on a c-AlN buffer, c-GaN grown at higher temperature does not show a significant SF anisotropy.
When employing miscut substrates (figure 4.31 d)), the FWHM is reduced down to 22.32 arcmin. This can be a consequence of suppressed APD formation. Stacking faults only occur in one direction along [-110]. Along [110] a comparable RSM's was measured with only a slight anistropy in SF distribution. Nevertheless, the hexagonal content was measured to be 10 % in [-110] and 0 % in [110] direction. Averaged a hexagonal content of 5 % was achieved with the step-flow growth mode. Also in this case, parameters were not optimized and a lower hexagonal phase content should be possible.
Together HRXRD measurements reveal, that it is possible to grow c-GaN at elevated temperature with comparable structural quality (hexagonal phase content, defect densities). Also when employing other Nitrides (c-AlN) and miscut surfaces (4° miscut 3C-SiC) comparable results can be achieved. In conclusion, elevated temperatures cause c-GaN epilayers to get smoother but also reduce the effects of SF annihilation and can increase hexagonal phase contents. Growth optimization for elevated temperatures could overcome the structural drawbacks while achieving smoother epilayers.

CHAPTER 5

Summary and Outlook

Selective Area Growth (SAG) of cubic Gallium Nitride (c-GaN) was demonstrated down to nano scales. The employed substrate was 3C-SiC (001) grown in Si. Different silicon oxides were used as growth masks. Deposition was optimized, especially for thermal oxides. Thermal oxidation of 3C-SiC is known for decades but rates can differ from oven to oven. Therefore, long oxidation series were carried out and the growth rate of thermal oxide on 3C-SiC was estimated by assumption of a Deal-Grove behaviour of the oxidation process.
Following deposition, the SiO_2 masks had to be patterned. For first experiments this was done by optical Lithography on Si. Silicon offers an elegant and cheap way to test parameters. Compared to 3C-SiC, bare Silicon substrates are about 100 times cheaper but offer very good quality and are structurally comparable.
The series conducted on Silicon yielded a critical substrate temperature indicating no nucleation of GaN on SiO_2 for a fixed Ga flux. A temperature of 870°C was found to be sufficient to prevent unwanted nucleation on the SiO_2 masks. The critical substrate temperature was adopted to patterned 3C-SiC substrates. However without an increase in substrate temperature, 870°C did not result in SAG. For proper SAG on 3C-SiC patterned with plasma deposited or thermal oxides, substrate temperatures of 930°C and 890°C are necessary, respectively.
In order to tailor smaller structures, different lithography methods were applied. Nanosphere Lithography (NSL) was used to pattern large Areas (A > 2x2 cm^2) with 130 nm holes in diameter. Block-Copolymer Lithography (BCP) was used to achieve 17 nm openings. Electron Beam Lithography was employed to pattern grooves. After patterning, the structures were transferred into 3C-SiC and SiO_2 by Reactive Ion etching with SF_6 and CHF_3/Ar chemistry, respectively. All of these methods required careful optimization.
Holes exposed aspect ratios ranging from 1 to 2. Grooves were patterned to either expose <001> or <111> facets of 3C-SiC along [110]. The achieved patterns therefore, were sophisticating to demonstrate nano SAG down to scales of 17 nm on <001> and 100 nm on <111> facets of 3C-SiC (001).
Hexagonal phase content was determined by means of Transmission Electron Microscopy (TEM) and High Resolution X-Ray Diffraction (HRXRD). HRXRD measurements revealed hexagonal phase contents of below 1% when overgrowing checkerboard patterns. Lowest hexagonal phase contents, measured on V-shaped grooves by HRXRD, was 17.6 % and was achieved by employing miscut substrates. After coalescence on BCP patterned holes, the hexagonal phase content was estimated to be 29 %. TEM revealed phase pure nucleation on NSL and EBL patterned <001> and <111> facets of 3C-SiC.

In addition, planar c-GaN growth on 3C-SiC without any patterns was tested to see how c-GaN behaves at such high temperatures. For elevated temperatures of 870°C it was shown to be possible to deposit c-GaN on 3C-SiC. Also buffers like c-AlN and miscut substrates were employed and it was demonstrated, that dominant cubic GaN can be also grown on them at elevated temperatures. All of this was achieved with out any optimization of the Ga flux.
In conclusion, these findings emphasize that it is possible to grown cubic Gallium Nitride selectively on 3C-SiC by Plasma Assisted Molecular Beam Epitaxy. This opens thinkable applications for techniques like Epitaxial Lateral Overgrowth [Ju04], Pendeoepitaxy [Lin99], Nano Hetero Epitaxy [Che08], Aspect Ratio Trapping [Man20], Phase transitions of merging growth fronts [Liu16] and many more. A lot of these techniques have also been shown to be possible for hexagonal Nitrides. However, defect densities were not reduced, yet.
Further research on the basis of the presented findings could improve structural quality of c-GaN. Up to now SF's are the dominant factor of structural degrading of c-GaN epilayers.

Bibliography

[Amb96] Ambacher, O., Brandt, M. S., Dimitrov, R., Metzger, T., Stutzmann, M., Fischer, R. A., Miehr, A., Bergmaier, A., and Dollinger, G.: 'Thermal stability and desorption of Group III nitrides prepared by metal organic chemical vapor deposition'. *Journal of Vacuum Science & Technology B: Microelectronics and Nanometer Structures Processing, Measurement, and Phenomena* (1996), vol. 14(6): pp. 3532–3542. doi: 10.1116/1.588793 (cit. on pp. 1, 8).

[Ard38] Ardenne, M. von: 'Das Elektronen-Rastermikroskop'. *Zeitschrift für Physik* (Sept. 1938), vol. 109(9): pp. 553–572. doi: 10.1007/BF01341584 (cit. on p. 31).

[As03] As, D. J.: 'Growth and characterization of MBE-grown cubic GaN, $In_xGa_{1-x}N$ And $Al_yGa_{1-y}N$'. *III-Nitride Semiconductor materials: Growth.* Ed. by M.O. Manasreh, I.T. Ferguson. Vol. 19. Taylor & Francis, New York, 2003. Chap. 9: pp. 323–450 (cit. on pp. 15, 33, 43, 54, 64, 96).

[As10] As, D. J.: 'Recent developments on non-polar cubic group III nitrides for optoelectronic applications'. *Proc.SPIE* (2010), vol. 7608. doi: 10.1117/12.846846 (cit. on pp. 43, 54, 55).

[Aye95] Ayers, J. E.: 'New model for the thickness and mismatch dependencies of threading dislocation densities in mismatched heteroepitaxial layers'. *Journal of Applied Physics* (1995), vol. 78(6): pp. 3724–3726. doi: 10.1063/1.359952 (cit. on p. 26).

[Ber06] Berrah, S., Abid, H., Boukortt, A., and Sehil, M.: 'Band Gap of Cubic AlN, GaN and InN compounds under pressure'. *Turk Journal of Physics* (2006), vol. 30: pp. 513–518 (cit. on p. 6).

[Ber10] Bertness, K. A., Sanders, A. W., Rourke, D. M., Harvey, T. E., Roshko, Al., Schlager, J. B., and Sanford, N. A.: 'Controlled Nucleation of GaN Nanowires Grown with Molecular Beam Epitaxy'. *Advanced Functional Materials* (2010), vol. 20(17): pp. 2911–2915. doi: https://doi.org/10.1002/adfm.201000381 (cit. on pp. 17, 57).

[Bin86] Binnig, G., Quate, C. F., and Gerber, Ch.: 'Atomic Force Microscope'. *Phys. Rev. Lett.* (9 Mar. 1986), vol. 56: pp. 930–933. doi: 10.1103/PhysRevLett.56.930 (cit. on p. 29).

[Blu74] Bludau, W., Onton, A., and Heinke, W.: 'Temperature dependence of the band gap of silicon'. *Journal of Applied Physics* (1974), vol. 45(4): pp. 1846–1848. doi: 10.1063/1.1663501 (cit. on p. 6).

[Bra18] Brassat, K., Kool, D., Bürger, J., and Lindner, K. N. J.: 'Hierarchical nanopores formed by block copolymer lithography on the surfaces of different materials pre-patterned by nanosphere lithography'. *Nanoscale* (21 2018), vol. 10: pp. 10005–10017. doi: 10.1039/C8NR01397G (cit. on pp. 47, 49).

[BRY] BRYAN, I. S.: 'Al-rich AlGaN and AlN Growth on Bulk AlN Single Crystal Substrates'. PhD thesis. North Carolina State University (cit. on p. 13).

[Bry16] Bryan, I., Bryan, Z., Mita, S., Rice, A., Tweedie, J., Collazo, R., and Sitar, Z.: 'Surface kinetics in AlN growth: A universal model for the control of surface morphology in III-nitrides'. *Journal of Crystal Growth* (2016), vol. 438: pp. 81–89. doi: https://doi.org/10.1016/j.jcrysgro.2015.12.022 (cit. on p. 13).

[Bur51] Burton, W. K., Cabrera, N., Frank, F. C., and Mott, N. F.: 'The growth of crystals and the equilibrium structure of their surfaces'. *Philosophical Transactions of the Royal Society of London. Series A, Mathematical and Physical Sciences* (1951), vol. 243(866): pp. 299–358. doi: 10.1098/rsta.1951.0006 (cit. on pp. 13, 14, 19).

[C B22] C. Boudias, D. Monceau, Product: *CaRine*. Oct. 2022 (cit. on p. 80).

[Cha18] Chang, B., Jensen, F., Hübner, F., and Jansen, H.: 'DREM2: a facile fabrication strategy for freestanding three dimensional silicon micro- and nanostructures by a modified Bosch etch process'. *Journal of Micromechanics and Microengineering* (July 2018), vol. 28(10): p. 105012. doi: 10.1088/1361-6439/aad0c4 (cit. on pp. 39, 40).

[Che08] Chen, G.-T., Chan, C.-H., Hou, C.-H., Liu, H.-H., Shiu, N.-W., Chang, M.-N., Chen, C.L., and Chyi, J.-I.: 'Epitaxial lateral overgrowth of GaN on AlGaN/(111)Si micropillar array fabricated by polystyrene microsphere lithography'. *Proc SPIE* (Mar. 2008), vol. 6894. doi: 10.1117/12.764475 (cit. on pp. 2, 57, 64, 102).

[Cru15] Crum, L. A.: 'Resource Paper: Sonoluminescence'. *The Journal of the Acoustical Society of America* (2015), vol. 138(4): pp. 2181–2205. doi: 10.1121/1.4929687 (cit. on p. 33).

[CRY] CRYSTAL: *Yttria-stabilized Zirconium Oxide (YSZ)*. Datenblatt YSZ Substrat. CRYSTAL GmbH. Ostendstrasse 25, 12459 Berlin, Germany (cit. on p. 6).

[Dav] Davydov, V.Yu., Klochikhin, A.A., Seisyan, R.P., Emtsev, V.V., Ivanov, S.V., Bechstedt, F., Furthmüller, J., Harima, H., Mudryi, A.V., Aderhold, J., Semchinova, O., and Graul, J.: 'Absorption and Emission of Hexagonal InN. Evidence of Narrow Fundamental Band Gap'. *physica status solidi (b)* (), vol. 229(3): r1–r3. doi: 10.1002/1521-3951(200202)229:3<R1::AID-PSSB99991>3.0.CO;2-O (cit. on p. 6).

[Dea65] Deal, B. E. and Grove, A. S.: 'General Relationship for the Thermal Oxidation of Silicon'. *Journal of Applied Physics* (1965), vol. 36(12): pp. 3770–3778. doi: 10.1063/1.1713945 (cit. on pp. 43, 44).

[Dep20] Deppe, M.: 'Germanium Doping of Aluminum-Containing Cubic Group III-Nitride Heterostructures'. PhD thesis. University of Paderborn, July 2020 (cit. on p. 56).

[Dub21] Dubrovskii, V. G.: 'Gallium Diffusion Flow Direction during Deposition on the Surface with Regular Hole Arrays'. *Technical Physics Letters* (Aug. 2021), vol. 47(8): pp. 601–604. doi: 10.1134/S1063785021060213 (cit. on p. 17).

[Fan08] Fang, H., Yang, Z. J., Wang, Y., Dai, T., Sang, L. W., Zhao, L. B., Yu, T. J., and Zhang, G. Y.: 'Analysis of mass transport mechanism in InGaN epitaxy on ridge shaped selective area growth GaN by metal organic chemical vapor deposition'. *Journal of Applied Physics* (2008), vol. 103(1): p. 014908. doi: 10.1063/1.2829784 (cit. on pp. 2, 17, 57).

[Fau16] Faucher, J., Masuda, T., and Lee, M. L.: 'Initiation strategies for simultaneous control of antiphase domains and stacking faults in GaAs solar cells on Ge'. *Journal of Vacuum Science & Technology B* (2016), vol. 34(4): p. 041203. doi: 10.1116/1.4945659 (cit. on p. 9).

[Fen12] Feneberg, M., Röppischer, M., Cobet, C., Esser, N., Schörmann, J., Schupp, T., As, D. J., Hörich, F., Bläsing, J., Krost, A., and Goldhahn, R.: 'Optical properties of cubic GaN from 1 to 20 eV'. *Phys. Rev. B* (15 Apr. 2012), vol. 85: p. 155207. doi: 10.1103/PhysRevB.85.155207 (cit. on p. 64).

[For05] Forte Poisson, M.-A. di, Magis, M., Tordjman, M., Sarazin, N., and Persio, J. di: 'MOCVD growth of group III nitrides for high power, high frequency applications'. *physica status solidi (c)* (2005), vol. 2(3): pp. 947–955. doi: https://doi.org/10.1002/pssc.200460600 (cit. on p. 1).

[Fre17] Frentrup, M., Lee, L. Y., Sahonta, S.-L., Kappers, M. J., Massabuau, F., Gupta, P., Rachel, A. Oliver, Humphreys, Colin J, and Wallis, David J: 'X-ray diffraction analysis of cubic zincblende III-nitrides'. *Journal of Physics D: Applied Physics* (2017), vol. 50(43): p. 433002. doi: 10.1088/1361-6463/aa865e (cit. on pp. 28, 64, 83).

[Fre00] Frey, T.: 'Cubic III-Nitride Quantum Structures Grown by Molecular Beam Epitaxy'. PhD thesis. University of Paderborn, June 2000.

[Fun84] Fung, C. D. and Kopanski, J. J.: 'Thermal oxidation of 3C silicon carbide single-crystal layers on silicon'. *Applied Physics Letters* (1984), vol. 45(7): pp. 757–759. doi: 10.1063/1.95394 (cit. on pp. 43, 44).

[Gat06] Gatzert, C., Blakers, A. W., Deenapanray, Prakash N. K., Macdonald, D., and Auret, F. D.: 'Investigation of reactive ion etching of dielectrics and Si in CHF3:O2 or CHF3:Ar for photovoltaic applications'. *Journal of Vacuum Science & Technology A* (2006), vol. 24(5): pp. 1857–1865. doi: 10.1116/1.2333571 (cit. on pp. 40, 41).

[Gle20] Gleichmann, N.: 'SEM vs TEM'. *Technology Networks* (2020), vol. 2020 (cit. on p. 32).

[Gol01] Goldberg, Levinshtein, Y., Rumyantsev, M., and Sergey: *Properties of advanced semiconductor materials: GaN, AIN, InN, BN, SiC, SiGek*. Vol. 25. SciTech Book News, 2001 (cit. on p. 6).

[Got11] Gotschke, T., Schumann, T., Limbach, F., Stoica, T., and Calarco, R.: 'Influence of the adatom diffusion on selective growth of GaN nanowire regular arrays'. *Applied Physics Letters* (2011), vol. 98(10): p. 103102. doi: 10.1063/1.3559618 (cit. on pp. 15, 17, 57).

[Gri22] Gridchin, V. O., Dvoretckaia, L. N., Kotlyar, K. P., Reznik, R. R., Parfeneva, A. V., Dragunova, A. S., Kryzhanovskaya, N. V., Dubrovskii, V. G., and Cirlin, G. E.: 'Selective Area Epitaxy of GaN Nanowires on Si Substrates Using Microsphere Lithography: Experiment and Theory'. *Nanomaterials* (2022), vol. 12(14). doi: 10.3390/nano12142341 (cit. on pp. 18, 20, 64, 71, 72).

[Had10] Haddock, S. H. D., Moline, M. A., and Case, J. F.: 'Bioluminescence in the Sea'. *Annual Review of Marine Science* (2010), vol. 2(1). PMID: 21141672: pp. 443–493. doi: 10.1146/annurev-marine-120308-081028 (cit. on p. 33).

[Har95] Harris G. L., 1953-, Electrical Engineers, Institution of, and service), INSPEC (Information: *Properties of silicon carbide*. English. At foot of t.p.: IEE. London : INSPEC, 1995 (cit. on p. 6).

[Has12] Hasegawa, S.: 'Reflection High-Energy Electron Diffraction'. *Characterization of Materials* (2012), vol.: pp. 1925–1938. DOI: https://doi.org/10.1002/0471266965.com139 (cit. on pp. 21, 22, 95).

[Hau18] Haung, J. J., Kuo, H.-C., and Shen, S.-C.: *Nitride Semiconductor Light-Emitting Diodes (LEDs) - Materials, Technologies and Applications*. Woodhead Publishing, 2018. DOI: 10.1016/C2016-0-01551-6 (cit. on pp. 1, 8).

[Hea96] Headrick, R. L., Kycia, S., Park, Y. K., Woll, A. R., and Brock, J. D.: 'Real-time x-ray-scattering measurement of the nucleation kinetics of cubic gallium nitride on β-SiC(001)'. *Phys. Rev. B* (20 Nov. 1996), vol. 54: pp. 14686–14691. DOI: 10.1103/PhysRevB.54.14686 (cit. on p. 15).

[Heb14] Heber, J.: 'Nobel Prize 2014: Akasaki, Amano & Nakamura'. *Nature Physics* (Nov. 2014), vol. 10(11): pp. 791–791. DOI: 10.1038/nphys3147 (cit. on p. 1).

[Hil13] Hiller, L., Stauden, T., Kemper, R., Lindner, J. K. N., As, D., and Pezoldt, J.: 'ECR-Ectching of Submicron and Nanometer Sized 3C-SiC(100) Mesa Structures'. *Materials Science Forum* (Jan. 2013), vol. 717-720: pp. 901–904. DOI: 10.4028/www.scientific.net/MSF.717-720.901 (cit. on p. 41).

[Hir08] Hiroto, S., Katsumi, K., and Akihiko, K.: 'Ti-mask Selective-Area Growth of GaN by RF-Plasma-Assisted Molecular-Beam Epitaxy for Fabricating Regularly Arranged InGaN/GaN Nanocolumns'. *Applied Physics Express* (Dec. 2008), vol. 1: p. 124002. DOI: 10.1143/apex.1.124002 (cit. on pp. 17, 57).

[Hsu12] Hsu, C.-W., Chen, Y. F., and Su, Y. K.: 'Nanoepitaxy of GaAs on a Si(001) substrate using a round-hole nanopatterned SiO2 mask'. *Nanotechnology* (Nov. 2012), vol. 23(49): p. 495306. DOI: 10.1088/0957-4484/23/49/495306 (cit. on p. 2).

[Jac22] Jackson, H., Smith, L., Yarrison-Rice, J., Ma, M., and Argyres, P.: 'Probing Electronic and Vibronic States in CdTe Self-Assembled Quantum Dots and CdS Nanowires using Room Temperature Resonant Raman Scattering'. (Aug. 2022), vol. (cit. on p. 33).

[Jan12] Jansen, H.V., Gardeniers, H., and Fluitman, J.H.J.: 'A survey on the reactive ion etching of silicon in microtechnology'. *J. Micromech. Microeng.* (Dec. 2012), vol. 6(14). DOI: 10.1088/0960-1317/6/1/002 (cit. on pp. 39, 41).

[Ju04] Ju, W., Gulino, D.A., and Higgins, R.: 'Epitaxial lateral overgrowth of gallium nitride on silicon substrate'. *Journal of Crystal Growth* (2004), vol. 263(1): pp. 30–34. doi: https://doi.org/10.1016/j.jcrysgro.2003.11.107 (cit. on pp. 2, 57, 64, 102).

[Kap97] Kapolnek, D., Keller, S., Vetury, R., Underwood, R. D., Kozodoy, P., Den Baars, S. P., and Mishra, U. K.: 'Anisotropic epitaxial lateral growth in GaN selective area epitaxy'. *Applied Physics Letters* (1997), vol. 71(9): pp. 1204–1206. doi: 10.1063/1.119626 (cit. on pp. 2, 17, 57).

[Kar14] Karouta, F.: 'A practical approach to reactive ion etching'. *Journal of Physics D: Applied Physics* (May 2014), vol. 47(23): p. 233501. doi: 10.1088/0022-3727/47/23/233501 (cit. on p. 39).

[Kem14] Kemper, R.: 'Cubic GaN on Pre-Patterned 3C-SiC-Si (001) Substrates'. PhD thesis. University of Paderborn, Apr. 2014 (cit. on pp. 2, 26, 54, 73).

[Kun08] Kuntharin, S., Sanorpim, S., Nakamura, T., Katayama, R., and Onabe, Kentaro: 'Structural Investigation of Cubic-Phase InN on GaAs (001) Grown by MBE under In- and N-Rich Growth Conditions'. *Semiconductor Photonics: Nano-Structured Materials and Devices*. Vol. 31. Advanced Materials Research. Trans Tech Publications, Jan. 2008: pp. 215–217. doi: 10.4028/www.scientific.net/AMR.31.215.

[Lae20] Laermer, F., Franssila, S., Sainiemi, L., and Kolari, K.: 'Deep reactive ion etching'. *Handbook of Silicon Based MEMS Materials and Technologies* (2020), vol. doi: 10.1016/B978-0-12-817786-0.00016-5 (cit. on p. 39).

[Lee19a] Lee, Y. L.: 'Structural Characterisation of Heteroepitaxial Zincblende Gallium Nitride'. PhD thesis. University of Cambridge, Jan. 2019 (cit. on pp. 9, 26, 98).

[Lee19b] Lee, Y. L., Frentrup, M., Vacek, P., Kappers, M. J., Wallis, D. J., and Oliver, R. A.: 'Investigation of stacking faults in MOVPE-grown zincblende GaN by XRD and TEM'. *Journal of Applied Physics* (2019), vol. 125(10): p. 105303. doi: 10.1063/1.5082846 (cit. on pp. 9, 72, 83).

[Lev11] Levinson, H. J.: *Principles of Lithography*. SPIE PRESS, 2011. doi: 10.1117/3.865363 (cit. on pp. 35–38).

[Lin99] Linthicum, K., Gehrke, T., Thomson, D., Carlson, E., Rajagopal, P., Smith, T., Batchelor, D., and Davis, R.: 'Pendeoepitaxy of gallium nitride thin films'. *Applied Physics Letters* (1999), vol. 75(2): pp. 196–198. doi: 10.1063/1.124317 (cit. on pp. 2, 57, 64, 102).

[Lit] Littmann, M.: *Epitaxie von c-GaN auf vorstrukturierten 3C-SiC Substraten* (cit. on pp. 41, 73).

[Liu16] Liu, R. and Bayram, C.: 'Maximizing cubic phase gallium nitride surface coverage on nano-patterned silicon (100)'. *Applied Physics Letters* (2016), vol. 109(4): p. 042103. doi: 10.1063/1.4960005 (cit. on pp. 2, 57, 64, 80, 102).

[Lot13] Lotze, C.: 'Fundamental Processes in Single Molecule Junctions: Interplay of Forces and Electronic Effects'. PhD thesis. Freie Universität Berlin, July 2013 (cit. on p. 29).

[Man20] Mantach, R., Vennéguès, P., Zuniga-Perez, J., De Mierry, P., Portail, M., and Feuillet, G.: 'Freestanding-quality dislocation density in semipolar GaN epilayers grown on SOI: aspect ratio trapping'. *Applied Physics Express* (Oct. 2020), vol. 13(11): p. 115504. doi: 10.35848/1882-0786/abc1cd (cit. on pp. 2, 57, 64, 102).

[Mei06] Mei, J., Srinivasan, S., Liu, R., Ponce, F. A., Narukawa, Y., and Mukai, T.: 'Prismatic stacking faults in epitaxially laterally overgrown GaN'. *Applied Physics Letters* (2006), vol. 88(14): p. 141912. doi: 10.1063/1.2193352 (cit. on p. 63).

[Mei21] Meier, F., Protte, M., Baron, E., Feneberg, M., Goldhahn, R., Reuter, D., and As, D. J.: 'Selective area growth of cubic gallium nitride on silicon (001) and 3C-silicon carbide (001)'. *AIP Advances* (2021), vol. 11(7): p. 075013. doi: 10.1063/5.0053865 (cit. on pp. 17, 60, 64).

[Muj03] Mujica, A., Rubio, Angel, Munoz, A., and Needs, R. J.: 'High-pressure phases of group-IV, III–V, and II–VI compounds'. *Rev. Mod. Phys.* (3 July 2003), vol. 75: pp. 863–912. doi: 10.1103/RevModPhys.75.863.

[Nic92] Nicoloso, N., Loebert, A., and Leibold, B.: 'Optical absorption studies of tetragonal and cubic thin-film yttria-stabilized zirconia'. *Sensors and Actuators B: Chemical* (1992), vol. 8(3): pp. 253–256. doi: https://doi.org/10.1016/0925-4005(92)85027-T (cit. on p. 6).

[Nip16] Nippert, F., Karpov, S. Yu., Callsen, G., Galler, B., Kure, T., Nenstiel, C., Wagner, M. R., Strassburg, M., Lugauer, H.-J., and Hoffmann, A.: 'Temperature-dependent recombination coefficients in InGaN light-emitting diodes: Hole localization, Auger processes, and the green gap'. *Applied Physics Letters* (2016), vol. 109(16): p. 161103. doi: 10.1063/1.4965298 (cit. on p. 8).

[Nis] Nishida, K., Kitamura, Y., Hijikata, Y., Yaguchi, H., and Yoshida, S.: 'Epitaxial growth of hexagonal and cubic InN films'. *physica status solidi (b)* (), vol. 241(12): pp. 2839–2842. doi: 10.1002/pssb.200405049.

[Oku98] Okumura, H., Hamaguchi, H., Koizumu, T., Balakrishnan, K., Ishida, Y., Arita, M., Chichibu, S., Nakanishi, H., Nagatomo, T., and Yoshida, S.: 'Growth of cubic III-nitrides by gas source MBE using atomic nitrogen plasma: GaN, AlGaN and AlN'. *Journal of Crystal Growth* (1998), vol. 189/190: pp. 390–394. doi: 10.1016/S0022-0248(98)00321-2 (cit. on p. 6).

[Pas04] Paszkowicz, W., Podsiadło, W., and Minikayev, R.: 'Rietveld-refinement study of aluminium and gallium nitrides'. *Journal of Alloys and Compounds* (2004), vol. 382(1). Proceedings of the European Materials Research Society Fall Meeting, Symposium B: pp. 100–106. doi: https://doi.org/10.1016/j.jallcom.2004.05.036 (cit. on p. 6).

[Poh20] Pohl, U. W.: *Epitaxy of semiconductors*. Springer Cham, 2020. doi: 10.1007/978-3-030-43869-2 (cit. on pp. 14, 21).

[Poh18] Pohl, U. W. and Böer, K. W.: *Semiconductor Physics*. Springer Cham, 2018. doi: 10.1007/978-3-319-69150-3 (cit. on pp. 33, 34).

[Pow93] Powell, R. C., Lee, N.-E., Kim, Y.-W., and Greene, J. E.: 'Heteroepitaxial wurtzite and zinc-blende structure GaN grown by reactive-ion molecular-beam epitaxy: Growth kinetics, microstructure, and properties'. *Journal of Applied Physics* (1993), vol. 73(1): pp. 189–204. doi: 10.1063/1.353882 (cit. on p. 6).

[Sch02] Schikora, D., As, D. J., and Lischka, K.: *The molecular beam epitaxy of cubic III-Nitrides*. Ed. by Tanya Paskova, Bo Monemar. Research Signpost, Kerala, India, 2002. Chap. 15: pp. 314–368 (cit. on pp. 5, 15, 16, 33, 43, 54, 64).

[Sch06] Schörmann, J., As, D. J., Lischka, K., Schley, P., Goldhahn, R., Li, S. F., Löffler, W., Hetterich, M., and Kalt, H.: 'Molecular beam epitaxy of phase pure cubic InN'. *Applied Physics Letters* (2006), vol. 89(26): p. 261903. doi: 10.1063/1.2422913 (cit. on p. 6).

[Sch11] Schumann, T., Gotschke, T., Limbach, F., Stoica, T., and Calarco, R.: 'Selective-area catalyst-free MBE growth of GaN nanowires using a patterned oxide layer'. *Nanotechnology* (Jan. 2011), vol. 22(9): p. 095603. doi: 10.1088/0957-4484/22/9/095603 (cit. on pp. 2, 17, 57).

[Sci] Scientific, HORIBA: *What are the main differences between an SEM, an ESEM, an SEM-FIB and an (S)TEM?* url: https://www.horiba.com/gbr/cathodoluminescence-spectroscopy-sem-esem-sem-fib-stem/ (visited on 08/14/2022) (cit. on p. 31).

[She02] Shen, X.M., Fu, Y., Feng, G., Zhang, B.S., Feng, Z.H., Wang, Y.T., and Yang, H.: 'Structural characterization of epitaxial lateral overgrown GaN on patterned GaN/GaAs(001) substrates'. *Journal of Crystal Growth* (2002), vol. 246(1): pp. 69–72. doi: https://doi.org/10.1016/S0022-0248(02)01827-4 (cit. on p. 2).

[She91] Sherwin, M. E. and Drummond, T. J.: 'Predicted elastic constants and critical layer thicknesses for cubic phase AlN, GaN, and InN on Beta-SiC'. *Journal of Applied Physics* (1991), vol. 69(12): pp. 8423–8425. doi: 10.1063/1.347412 (cit. on p. 6).

[Shi89] Shitara, T. and Nishinaga, T.: 'Surface Diffusion Length of Gallium during MBE Growth on the Various Misoriented GaAs(001) Substrates'. *Japanese Journal of Applied Physics* (July 1989), vol. 28(Part 1, No. 7): pp. 1212–1216. doi: 10.1143/jjap.28.1212 (cit. on p. 13).

[Son04] Song, Y., Dhar, S., Feldman, L. C., Chung, G., and Williams, J. R.: 'Modified Deal Grove model for the thermal oxidation of silicon carbide'. *Journal of Applied Physics* (2004), vol. 95(9): pp. 4953–4957. doi: 10.1063/1.1690097 (cit. on pp. 43–45).

[Sta13] Stark, C. J. M., Detchprohm, T., Lee, S. C., Jiang, Y.-B., Brueck, S. R. J., and Wetzel, C.: 'Green cubic GaInN/GaN light-emitting diode on microstructured silicon (100)'. *Applied Physics Letters* (2013), vol. 103(23): p. 232107. doi: 10.1063/1.4841555 (cit. on p. 17).

[Str52] Straumanis, M. E. and Aka, E. Z.: 'Lattice Parameters, Coefficients of Thermal Expansion, and Atomic Weights of Purest Silicon and Germanium'. *Journal of Applied Physics* (1952), vol. 23(3): pp. 330–334. doi: 10.1063/1.1702202 (cit. on p. 6).

[Str92] Strite, S. and Morkoç, H.: 'GaN, AlN, and InN: A review'. *Journal of Vacuum Science & Technology B: Microelectronics and Nanometer Structures Processing, Measurement, and Phenomena* (1992), vol. 10(4): pp. 1237–1266. doi: 10.1116/1.585897 (cit. on pp. 1, 8).

[Sud00] Suda, J., Kurobe, T., Nakamura, S., and Matsunami, H.: 'Selective Area Growth of Cubic GaN on 3C-SiC (001) by Metalorganic Molecular Beam Epitaxy'. *Japanese Journal of Applied Physics* (Nov. 2000), vol. 39(Part 2, No. 11A): pp. L1081–L1083. doi: 10.1143/jjap.39.l1081 (cit. on p. 17).

[Tab99] Tabata, A., Lima, A. P., Teles, L. K., Scolfaro, L. M. R., Leite, J. R., Lemos, V., Schöttker, B., Frey, T., Schikora, D., and Lischka, K.: 'Structural properties and Raman modes of zinc blende InN

epitaxial layers'. *Applied Physics Letters* (1999), vol. 74(3): pp. 362–364. DOI: 10.1063/1.123072 (cit. on p. 6).

[Tac91] TACHI, S., TSUJIMOTO, K., ARAI, S., and KURE, T.: 'Low-temperature dry etching'. *Journal of Vacuum Science & Technology A* (1991), vol. 9(3): pp. 796–803. DOI: 10.1116/1.577364 (cit. on p. 41).

[Tak09] TAKAFUMI, Y. and SOON-KU, H.: *Oxide and Nitride Semiconductors - Processing, Properties and Applications*. Springer Berlin, Heidelberg, 2009. DOI: 10.1007/978-3-540-88847-5 (cit. on p. 63).

[Tan00] TANAKA, S., KAWAGUCHI, Y., SAWAKI, N., HIBINO, M., and HIRAMATSU, K.: 'Defect structure in selective area growth GaN pyramid on (111)Si substrate'. *Applied Physics Letters* (2000), vol. 76(19): pp. 2701–2703. DOI: 10.1063/1.126448 (cit. on pp. 2, 17, 57).

[Tas19] TASSEV, V. L. and VANGALA, S. R.: 'Thick Hydride Vapor Phase Heteroepitaxy: A Novel Approach to Growth of Nonlinear Optical Materials'. *Crystals* (2019), vol. 9(8). DOI: 10.3390/cryst9080393 (cit. on p. 11).

[Tel02] TELES, L.K, FURTHMÜLLER, J., SCOLFARO, L.M.R., TABATA, A., LEITE, J.R., BECHSTEDT, F., T, FREY., AS, D.J., and LISCHKA, K.: 'Phase separation and gap bowing in zinc-blende InGaN, InAlN, BGaN, and BAlN alloy layers'. *Physica E: Low-dimensional Systems and Nanostructures* (2002), vol. 13(2): pp. 1086–1089. DOI: https://doi.org/10.1016/S1386-9477(02)00309-0.

[Tsa22] TSAI, Y.-C., LEBURTON, J.-P., and BAYRAM, C.: 'Quenching of the Efficiency Droop in Cubic Phase InGaAlN Light-Emitting Diodes'. *IEEE Transactions on Electron Devices* (2022), vol. 69(6): pp. 3240–3245. DOI: 10.1109/TED.2022.3167645 (cit. on pp. 1, 8).

[Wec13] WECKER, T.: *Herstellung und Charakterisierung von symmetrischen und asymmetrischen Doppel Quantum Wells*. Aug. 2013 (cit. on pp. 25, 27).

[Wri97] WRIGHT, A. F.: 'Elastic properties of zinc-blende and wurtzite AlN, GaN, and InN'. *Journal of Applied Physics* (1997), vol. 82(6): pp. 2833–2839. DOI: 10.1063/1.366114.

[Yao] YAO, G.: 'Growth mechanisms of InN on zirconia surfaces'. PhD thesis. University of Tokyo.

[Zeo] ZEON: *Zeon ZEP520A EBL resist Datasheet*. https://www.zeon.co.jp/en/business/enterprise/electronic/imagelec/. [Online; accessed 25.10.2022] (cit. on p. 51).

List of Figures

List of Tables

A First chapter of appendix

A.1 Sample list

Number	Substrate	Date	Comment
GNF3014	17CO-012	23.05.2019	c-GaN Reference before chamber opening
GNF3019	17CO-012	27.06.2019	c-GaN Reference after chamber opening
ANF3023	17CO-012	16.07.2019	c-AlN parameter optimization
GNF3025	16CO-140	18.07.2019	c-AlN parameter optimization
GNF3026	16CO-140	19.07.2019	c-AlN parameter optimization
GNF3027	16CO-140	23.07.2019	c-GaN 600 nm Reference
GNF3028	16CO-140	24.07.2019	c-GaN 600 nm Reference - Missing
ANF3033	16CO-140	15.08.2019	c-AlN parameter optimization
ANF3034	16CO-140	16.08.2019	c-AlN parameter optimization
ANF3035	16CO-140	21.08.2019	c-AlN parameter optimization
ANF3036	16CO-140	22.08.2019	c-AlN parameter optimization
ANF3037	16CO-140	23.08.2019	c-AlN parameter optimization
ANF3038	16CO-140	26.08.2019	c-AlN parameter optimization
ANF3039	16CO-140	27.08.2019	c-AlN parameter optimization
ANF3040	16CO-140	27.08.2019	c-AlN parameter optimization
ANF3041	16CO-140	28.08.2019	c-AlN parameter optimization
GNF3044	16CO-140	10.09.2019	c-GaN on c-AlN test
INF3045	16CO-140	11.09.2019	c-InN on c-AlN test
GNF3046	16CO-140	12.09.2019	c-GaN on c-AlN test
ANF3047	16CO-140	17.09.2019	c-AlN parameter optimization
GNF3048	TYN-B-11	09.10.2019	MQW 4° off, test for Henning - Missing
GNF3049	X-6536-05	10.10.2019	MQW, test for Henning
ANF3050	TYN-B-11	16.10.2019	AlN 4° off test
ANF3051	TYN-B-11	17.10.2019	AlN 4° off test
ANF3052	X-6536-05	21.10.2019	AlN parameter optimization
ANF3053	16CO-140	22.10.2019	AlN parameter optimization
GNF3055	16CO-140	07.01.2020	c-GaN Reference for SAG experiments
1SWTF3057	Si	13.01.2020	SAG test T-SiO2/Si
2SWTF3058	Si	13.01.2020	SAG test T-SiO2/Si
3SWTF3059	Si	14.01.2020	SAG test T-SiO2/Si
4SWTF3060	Si	14.01.2020	SAG test T-SiO2/Si
5SWTF3061	Si	15.01.2020	SAG test T-SiO2/Si
6SWTF3062	Si	15.01.2020	SAG test T-SiO2/Si
7SWTF3063	Si	16.01.2020	SAG test T-SiO2/Si
8SWTF3064	Si	16.01.2020	SAG test T-SiO2/Si
9SWTF3065	Si	17.01.2020	SAG test T-SiO2/Si

10SWTF3066	Si	17.01.2020	SAG test T-SiO2/Si
			Success - Published AIP Advances 2021.
AGNF3071	16CO-140	07.02.2020	c-GaN on c-AlN @870°C
AGNF3072	16CO-140	12.02.2020	c-GaN on c-AlN @870°C
			Pieces used for XRD Demo
GNF3073	16CO-140	17.02.2020	c-GaN on 3C-SiC @870°C
1SWPF3078	Si	03.03.2020	SAG test P-SiO2/Si
2SWPF3079	Si	03.03.2020	SAG test P-SiO2/Si
3SWPF3080	Si	04.03.2020	SAG test P-SiO2/Si
4SWPF3081	Si	04.03.2020	SAG test P-SiO2/Si
5SWPF3082	Si	05.03.2020	SAG test P-SiO2/Si
6SWPF3083	Si	05.03.2020	SAG test P-SiO2/Si
7SWPF3084	Si	06.03.2020	SAG test P-SiO2/Si
8SWPF3085	Si	09.03.2020	SAG test P-SiO2/Si
9SWPF3086	Si	09.03.2020	SAG test P-SiO2/Si
10SWPF3087	Si	10.03.2020	SAG test P-SiO2/Si
			Success - Published AIP Advances 2021.
AGNF3091	16CO-140	12.03.2020	c-AlN on 3C-SiC @870°C
GNF3092	16CO-140	13.03.2020	Ga flash tests
GNF3093	16CO-020	17.03.2020	c-GaN on 3C-SiC @870°C
GNF3105	16CO-020	18.03.2020	c-GaN on 3C-SiC @900°C
INF3108	16CO-020	15.06.2020	InGaN test
INF3109	16CO-020	16.06.2020	InGaN test
INF3111	16CO-020	18.06.2020	InGaN test
INF3112	16CO-020	19.06.2020	InGaN test
INF3114	16CO-020	22.06.2020	InGaN test
GNF3122	16CO-020	13.07.2020	SAG 3C-SiC checkerboard test
GNF3123	16CO-020	14.07.2020	SAG 3C-SiC checkerboard test
GNF3124	16CO-020	15.07.2020	SAG 3C-SiC checkerboard test
GNF3135	16CO-140	27.08.2020	SAG 3C-SiC checkerboard test
GNF3136	16CO-140	28.08.2020	SAG 3C-SiC checkerboard test
GNF3138	16CO-140	02.09.2020	SAG 3C-SiC checkerboard test
GNF3139	16CO-140	02.09.2020	SAG 3C-SiC checkerboard test
GNF3140	16CO-140	07.09.2020	SAG 3C-SiC checkerboard test
GNF3141	16CO-140	09.09.2020	SAG 3C-SiC checkerboard test
			Success - Published AIP Advances 2021.
GNF3142	16CO-140	11.09.2020	SAG 3C-SiC checkerboard test
GNF3143	16CO-140	15.09.2020	SAG 3C-SiC checkerboard test

GNF3163	16CO-140	10.12.2020	SAG 3C-SiC checkerboard test
GNF3167	16CO-140	11.12.2020	SAG 3C-SiC checkerboard test
GNF3177	16CO-020	03.05.2021	c-GaN Reference
GNF3181	16CO-020	04.05.2021	c-GaN on 3C-SiC @930°C
SWGNF3185	16CO-020	17.05.2021	SAG T-SiO2/3C-SiC NSL test
SWGNF3186	16CO-020	18.05.2021	SAG T-SiO2/3C-SiC NSL test
INF3201	YSZ	19.05.2021	InN on Graphene on YSZ test
SWGNF3202	16CO-020	05.07.2021	SAG T-SiO2/3C-SiC NSL test
SWGNF3203	16CO-020	06.07.2021	SAG P-SiO2/3C-SiC NSL test
SWGNF3304	16CO-020	07.07.2021	SAG P-SiO2/3C-SiC NSL test
INF3207	16CO-020	10.08.2021	InN parameter optimization
INF3208	16CO-020	12.08.2021	InN parameter optimization
INF3209	16CO-020	13.08.2021	InN parameter optimization
INF3210	16CO-020	16.08.2021	InN parameter optimization
GNLF3213	14CO-142	01.09.2021	c-GaN on 2x2 cm^2 3C-SiC test
INZ3214	Ge/GaAs NW	02.09.2021	c-InN on Ge capped GaAs NW (Zhang)
INZ3215	Ge/GaAs NW	02.09.2021	c-InN on Ge capped GaAs NW (Zhang)
INZ3216	Ge/GaAs NW	02.09.2021	c-InN on Ge capped GaAs NW (Zhang)
GNF3277	16CO-020	05.10.2021	c-GaN thin film
INF3228	YSZ	13.10.2021	InN on YSZ test
INF3230	YSZ	18.10.2021	InN on YSZ test
SWGNF3232	16CO-020	21.10.2021	SAG T-SiO2/3C-SiC NSL test
SWGNF3233	16CO-020	22.10.2021	SAG T-SiO2/3C-SiC NSL test
GNF3224	16CO-020	25.10.2021	c-GaN on 2x2 cm^2 3C-SiC test
INMF3236	YSZ	27.10.2021	InN on Graphene on YSZ test
SWGNF3240	16CO-020	03.11.2021	SAG P-SiO2/3C-SiC NSL test
SWGNF3242	16CO-020	05.11.2021	SAG P-SiO2/3C-SiC NSL test
PG1_SWGNF3243	20CO-017	09.11.2021	SAG P-SiO2/3C-SiC V-shaped grooves test
			Structure PG1 overgrown
AGNF3246	20CO-017	12.11.2021	c-GaN on c-AlN @870°C
			Pieces sent to AG Meier
AGNF3247	20CO-017	15.11.2021	c-GaN on c-AlN @870°C
GNF3250	20CO-017	12.11.2021	c-GaN on 3C-SiC @870°C
GNF3251	20CO-017	24.11.2021	c-GaN on 3C-SiC @870°C
PG4_SWGNF3252	20CO-017	29.11.2021	SAG P-SiO2/3C-SiC V-shaped grooves test
			Structure PG4 overgrown
PG5_SWGNF3253	20CO-017	30.11.2021	SAG P-SiO2/3C-SiC V-shaped grooves test
			Structure PG5 overgrown

SWGNF3254	20CO-017	01.12.2021	SAG P-SiO2/3C-SiC BCP patterned
GNF3255	20CO-017	02.12.2021	c-GaN reference
GNF3256	20CO-017	21.12.2021	600 nm c-GaN
INF3257	YSZ	23.12.2021	InN on YSZ test
INF3258	YSZ	29.12.2021	InN on YSZ test
INF3259	YSZ	29.12.2021	InN on YSZ test
GNF3260	20CO-017	05.01.2022	c-GaN
INZ3261	Ge/GaAs NW	06.01.2022	c-InN on Ge capped GaAs NW (Zhang)
INZ3262	Ge/GaAs NW	07.01.2022	c-InN on Ge capped GaAs NW (Zhang)
INF3263	YSZ	10.01.2022	InN on Graphene on YSZ test
GNF3264	20CO-017	11.01.2022	600 nm c-GaN
PG8_SWGNF3265	20CO-017	12.01.2022	SAG P-SiO2/3C-SiC V-shaped grooves test
			Structure PG8 overgrown
SWGNF3266	20CO-017	13.01.2022	SAG P-SiO2/3C-SiC BCP patterned - Missing
PG6_SWGNF3268	20CO-017	15.01.2022	SAG P-SiO2/3C-SiC V-shaped grooves test
			Structure PG6 overgrown
PG7_SWGNF3269	20CO-017	20.01.2022	SAG P-SiO2/3C-SiC V-shaped grooves test
			Structure PG7 overgrown
PG9_SWGNF3273	20CO-017	25.01.2022	SAG P-SiO2/3C-SiC V-shaped grooves test
			Structure PG9 overgrown
GNF3277	TYN-B-11	09.02.2022	c-GaN on 4° off 3C-SiC @870°C
PG13_SWGNF3279	20CO-017	15.02.2022	SAG P-SiO2/3C-SiC V-shaped grooves test
			Structure PG13 overgrown
AGNF3282	TYN-B-11	16.03.2022	AlGaN test on 4° off 3C-SiC
GNF3284	20CO-017	22.02.2022	c-GaN on 4° off 3C-SiC @870°C
AGNF3286	20CO-017	07.03.2022	AlGaN on 4° off 3C-SiC @870°C
AGNF3287	20CO-017	08.03.2022	AlGaN on 4° off 3C-SiC @870°C
			sent away for CL, ECCI
PG18	20CO-017	21.03.2022	Aspect Ratio test EBL patterned - Missing
AGNF3295	20CO-017	29.03.2022	AlGaN test on 3C-SiC @870°C
INF3299	YSZ	06.04.2022	InN on InO on YSZ
INZ3300	YSZ	07.04.2022	InO on YSZ
GNF3302	20CO-017	12.04.2022	SAG GaN on 3C-SiC BCP patterned
PG21_SWGNF3303	20CO-017	13.04.2022	SAG P-SiO2/3C-SiC V-shaped grooves test
			Structure PG21 overgrown, to be published
PG22_SWGNF3304	20CO-017	14.04.2022	SAG P-SiO2/3C-SiC V-shaped grooves test
			Structure PG22 overgrown, to be published
GNF3305	20CO-017	19.04.2022	2x2 cm^2 c-GaN buffer for BCP patterning

INF3306	YSZ	21.04.2022	InN on YSZ
INF3307	YSZ	22.04.2022	InN on YSZ
SWGNF3307	20CO-017	29.04.2022	SAG T-SiO2/3C-SiC NSL test
SWGNF3308	20CO-017	03.05.2022	SAG T-SiO2/3C-SiC NSL test
SWGNF3312	20CO-017	13.05.2022	SAG P-SiO2/3C-SiC NSL test
SWGNF3313	20CO-017	16.05.2022	SAG P-SiO2/3C-SiC NSL test
SWGNF3314	20CO-017	18.05.2022	SAG P-SiO2/3C-SiC NSL test
SWGNF3315	20CO-017	19.05.2022	SAG P-SiO2/3C-SiC NSL test
SWGNF3316	20CO-017	01.06.2022	SAG P-SiO2/3C-SiC NSL test
SWGNF3317	20CO-017	03.06.2022	SAG P-SiO2/3C-SiC NSL test
SWGNF3320	20CO-017	10.06.2022	SAG P-SiO2/3C-SiC BCP patterned
PG24	20CO-017	13.06.2022	SAG P-SiO2/3C-SiC V-shaped grooves test
			Structure PG24 overgrown, to be published

Publications

Scientific publications

1. **Falco Meier**, Maximillian Protte, Elias Baron, Martin Feneberg, Rüdiger Goldhahn, Dirk Reuter, and Donat Josef As , "Selective area growth of cubic gallium nitride on silicon (001) and 3C-silicon carbide (001)", AIP Advances 11, 075013 (2021) https://doi.org/10.1063/5.0053865
2. **Falco Meier**, Mario Littmann, Julius Bürger, Thomas Riedl, Daniel Kool, Jörg Lindner, Dirk Reuter, Donat Josef As, "Selective area growth of cubic Gallium Nitride in nanoscopic Silicon Dioxide masks", IWN2022 conference contribution, Phys. Status Solidi B, 2200508 (2023), https://doi.org/10.1002/pssb.202200508

Submissions to conferences

1. Thomas Riedl[1], Julius Bürger, **Falco Meier**, D. J. As, J. K. Lindner: "Microscopic investigation of selective-area MBE of cubic GaN in defect-trapping mask nanoholes on 3C-SiC/Si (001)", *Poster presentation*, MS2.P011, MC 2021, August, Wien, Austria
2. **Falco Meier**, Dirk Reuter, Donat Josef As: "Selective area growth of cubic gallium nitride on 3C-silicon carbide (001)", *Poster presentation*, P11, DEMBE 2021, October, Göttingen, Germany
3. **Falco Meier**, Julius Bürger, Thomas Riedl, Daniel Kool, Jörg K.N. Lindner, Dirk Reuter, Donat Josef As: "Selective Area Growth of cubic Gallium Nitride in nanoscopic Silicon Dioxide masks", *Poster presentation*, PP 079, IWN 2022, October, Berlin, Germany

1 Presenting author is underlined

Acknowledgments

I would like to extend my gratitude to the working groups of Professors Donat J. As and Dirk Reuter for providing me with the opportunity to pursue my PhD thesis at the University of Paderborn. Their professional advice, patience, and support were invaluable in my academic journey.

I would like to specifically acknowledge Mario Littmann and Dr. Michael Deppe for their constant provision of information and cooperation in maintaining our outdated equipment.

Lastly, I would like to express my appreciation to my family for their unwavering support and patience throughout my academic career. Their encouragement and understanding have been a source of strength and motivation.